

NACA RM A53D10

6411

0143335

TECH LIBRARY KAFB, NM

NACA

RESEARCH MEMORANDUM

WIND-TUNNEL INVESTIGATION OF THE VORTEX WAKE AND DOWNWASH
FIELD BEHIND TRIANGULAR WINGS AND WING-BODY

COMBINATIONS AT SUPERSONIC SPEEDS

By J. Richard Spahr and Robert R. Dickey

Ames Aeronautical Laboratory
Moffett Field, Calif.

NATIONAL ADVISORY COMMITTEE
FOR AERONAUTICS

WASHINGTON

June 25, 1953

19.98/13

Classification cancelled (or changed to UNCLASSIFIED)

By Authority of ASA TECH PAR AMENDMENT #126
(OFFICER AUTHORIZED TO CHANGE)

By.....2 May 68.....
NAME AND

.....(NMP).....
GRADE OF OFFICER MAKING CHANGE)

27 Mar 61
DATE



NATIONAL ADVISORY COMMITTEE FOR AERONAUTICS

RESEARCH MEMORANDUM

WIND-TUNNEL INVESTIGATION OF THE VORTEX WAKE AND DOWNWASH

FIELD BEHIND TRIANGULAR WINGS AND WING-BODY

COMBINATIONS AT SUPERSONIC SPEEDS

By J. Richard Spahr and Robert R. Dickey

SUMMARY

The flow field behind triangular wings (aspect ratios of 0.67 to 4) alone and in combination with a pointed cylindrical body has been investigated at Mach numbers of 1.5 and 2.0 through an angle-of-attack range of 0° to 24° . The character of the vortex wake was observed by means of the vapor-screen flow-visualization technique, and certain regions of the downwash field associated with the observed vortex systems were surveyed. Estimates of the downwash distributions were also made using a method based on existing theories, and the results have been compared with experiment.

The initial character and subsequent behavior of the wing trailing vortex wake with or without the body present were observed to vary significantly with the wing aspect ratio and with the angle of attack. For low-aspect-ratio wings at small angles of attack and for large-aspect-ratio wings throughout the test angle-of-attack range, the nature and behavior of the wake is in accord with theoretical predictions; that is, the vortex wake leaves the wing trailing edge as a sheet and proceeds to roll up into one or two (depending on the type of spanwise load distribution) regions of vorticity behind each wing panel as it progresses downstream. One region of vorticity exists behind each wing panel at small angles of attack when the span load distribution is elliptic, and two regions exist at large angles of attack and for large aspect ratios when the load distribution is partially linear. The rate at which the rolling up takes place increases with angle of attack and decreases with increasing aspect ratio as predicted by theory. The vortex wake from the low-aspect-ratio wings at large angles of attack fails to leave the trailing edge as a sheet since the vorticity discharged from each wing panel becomes separated from the upper surface and rolls up into a single vortex ahead of the trailing edge.

At moderate and large angles of attack, the presence of the body in combination with the wings was observed to introduce two additional pairs of vortices into the flow field as a result of body cross-flow separation, one pair from the forebody and one pair from the afterbody.

Downwash-survey results generally confirmed the flow-visualization observations as to the identity and locations of the discrete vortices in the flow field. The experimental downwash field of the isolated body at small angles of attack was in agreement with that predicted by potential-flow theory, but at large angles the influence of viscous cross-flow separation was found to produce significant differences, especially in the immediate vicinity of the vortices associated with this separation. At small angles of attack the experimentally determined downwash field behind wing-body combinations having low-aspect-ratio subsonic-leading-edge wings was closely predicted by theoretical calculations in which a single vortex was used to replace the wake from each wing panel. For a wing-body combination having an aspect ratio 4 supersonic-leading-edge wing, three vortices were required in the theoretical calculations to predict the measured downwash distributions. At large angles of attack the agreement between the experimental and theoretical downwash was at best only qualitative, primarily because of flow-separation effects on the wing and body.

INTRODUCTION

The rational design of airplanes and missiles requires knowledge of the mutual aerodynamic interactions of the wing, body, and tail since these interactions can exert a significant influence on both the longitudinal and lateral stability and control characteristics. These effects are of greatest importance for airframes for which the body is large relative to the wing and the tail span is a large fraction of the wing span. In such cases the effects on the rearward lifting surfaces of the vortex wake from the forward surfaces can result in highly non-linear stability characteristics and in large rolling moments in combined pitch and sideslip which may be intolerable.

A number of theoretical and experimental studies have been made to investigate the nature of the flow field behind wings at supersonic speeds. In references 1 to 8, various applications of linearized supersonic wing theory have been employed to compute the downwash field behind such wings in which the wing vorticity is implicitly assumed to be contained in a flat vortex sheet which remains undistorted to infinity in the free-stream direction. However, the analysis of references 9 and 10 and the experimental results of references 11 to 14 show that for low-aspect-ratio wings these linearized theory results cannot be used for a realistic prediction of the downwash field in the

vicinity of the probable tail-plane location, except near zero angle of attack, because of the deflection and rolling up of the vortex sheet. The effects of this rolling-up process are illustrated by the theoretical computations of reference 15 in which large differences were found in the lift and moment characteristics of a wing-tail combination between those calculated on the basis of a flat deflected vortex sheet and those based on two vortex lines (simulating a fully rolled-up vortex sheet). The influence of a body on these wing-tail interference effects has been investigated only to a very limited extent. The general problem is discussed theoretically in reference 16, and closed expressions have been derived in reference 17 on the basis of slender-body theory for the force and moment characteristics of a particular family of wing-body-tail combinations for the two limiting cases of a flat vortex sheet and two vortex lines.

An experimental investigation of a wing-body combination has been reported in reference 18 in which the downwash and sidewash fields at the tail location of a low-aspect-ratio, cruciform, triangular-wing missile were surveyed. It was found that the flow field at the tail-plane location corresponded to that for a single vortex from each wing panel, indicating that the vortex sheets from this wing were essentially rolled up for the moderate angles of attack investigated. The aerodynamic forces on this missile have been investigated experimentally, and the longitudinal characteristics are reported in reference 19. Theoretical predictions of these characteristics were made in which the lift on each wing panel was replaced by a line vortex of suitable strength, and the resulting pitching-moment characteristics were in close agreement with the corresponding experimental results.

Since the existing experimental information on the induced flow behind wings and wing-body combinations is limited to specific configurations and, for the most part, to small angles of attack, and since no theoretical method has been shown to be applicable to the prediction of these flow characteristics for a general configuration, the present experimental and analytical investigation has been undertaken with the following objectives: (1) to study experimentally the physical nature and origin of the induced flow field behind a family of lifting triangular wings and wing-body combinations at supersonic speeds by means of flow-visualization observations, (2) to measure representative downwash distributions associated with these flow fields, and (3) to compare these distributions with theoretical computations in which the discharged vorticity from the wing is replaced by a system of discrete vortices, and the body is replaced by the corresponding image vortex system.

NOTATION

A	aspect ratio, $\frac{b^2}{S}$
a	body radius, ft
b	total wing span, ft
C_L	lift coefficient, $\frac{L}{qS}$
c_l	wing section lift coefficient, $\frac{l}{qc}$
c	local wing chord, ft
\bar{c}	mean aerodynamic chord, $\frac{2}{S} \int_0^S c^2 dy$, ft
c_0	wing chord at wing center line, ft
c_r	wing chord at body juncture, ft
e	streamwise distance behind the trailing edge for the vortex sheet to become essentially rolled up, ft
i_w	wing incidence, deg
L	lift, lb
l	section lift, lb/ft
M	free-stream Mach number
q	free-stream dynamic pressure, lb/sq ft
R	Reynolds number, $\frac{V_0 c_r}{\nu}$
r_i	radial distance of an image vortex from the body axis, ft
r_v	radial distance of a wing vortex from the body axis, ft
S	total wing area (including the area within the body obtained by an extension of the leading and trailing edges of the wing to the body axis), sq ft
s	wing semispan, $\frac{b}{2}$, ft
V	free-stream velocity, ft/sec

- v, w velocity components corresponding to y and z , respectively, ft/sec
- x, y, z coordinates of a right-hand Cartesian system of axes having its origin at the intersection of the body axis and wing trailing edge, the x axis coincident with the body axis, and the y axis coincident with the wing trailing edge, x positive in the rearward direction, ft
- y_v, z_v y and z coordinates of the center of a vortex
- α angle of attack, deg
- β $\sqrt{M^2 - 1}$
- Γ circulation (positive for counterclockwise rotation, viewed upstream) ft²/sec
- ϵ angle of downwash, deg
- ν kinematic viscosity, ft²/sec

Subscripts

- L.T. linear theory
- S.B. slender-body theory
- C wing-body combination less nose
- W isolated wing
- W(B) wing in the presence of the body

APPARATUS

Wind Tunnel

The experimental investigation was conducted in the Ames 1- by 3-foot supersonic wind tunnel No. 1. This wind tunnel is a closed-circuit, continuous-operation tunnel in which both the Mach number and Reynolds number are variable. Mach numbers from 1.2 to 2.2 are obtained by adjusting the contour of the flexible steel plates which form the upper and lower walls of the nozzle.

Flow-Visualization Apparatus

A flow-visualization technique known as the "vapor-screen method," the apparatus for which is shown schematically in figure 1, was used to investigate the vortex-wake patterns generated by the models. In this technique, a small amount of water is introduced into the air stream to produce a fine fog in the tunnel test section. A narrow plane of intense light, produced by a high-pressure mercury-vapor lamp, is projected across the test section in a plane essentially perpendicular to the air stream. This plane of light is visible as a lighted screen because of the scattering of the light by the water particles in the wind tunnel. In regions of undisturbed flow this lighted screen appears uniform; however, flow disturbances produced by the model affect the amount of light scattered which results in the flow disturbances appearing on the lighted screen as areas of contrasting light intensity. Photographs of the vortex-wake patterns were taken with a camera looking through the test-section window and giving approximately a three-quarter front view of the model (see fig. 1(b)) and vortex-wake pattern. Because of this oblique angle between the camera and the light plane, the resulting photographs of the vortex-wake patterns were distorted. In order to make quantitative measurements from these photographs of the lateral and vertical positions of the vortices (which appear as dark areas) relative to the model, corresponding photographs were obtained of an accurately ruled grid placed at the same position relative to the camera as the light screen. The negative of the grid photograph thus obtained was then superimposed on the original photograph of the flow pattern and the vortex positions relative to a wind-axis system were determined. When the light screen intersected the model ahead of the wing trailing edge, the reflected light from the model sometimes obscured the flow patterns. Under these conditions, photographs of the vapor screen at or ahead of the wing trailing edge were obtained by means of a 16 mm motion-picture camera mounted inside the wind tunnel directly behind one wing panel, as shown in figure 1.

Downwash Survey Apparatus

Spanwise downwash-angle surveys behind the models were made by means of the nulled-cone apparatus shown in figure 2. This device consisted of a 30° cone supported from the side of the test section by a wedge-shaped strut. The cone could be moved laterally across the test section and rotated in pitch until the pressures measured at the top and bottom orifices of the cone indicated that the axis of the cone was in line with the local stream. The lateral range of the surveys was limited by the interference of the cone support with the model on one side and by the interference of the cone support with the tunnel wall on

the other side. Because the longitudinal and vertical position of the survey cone was limited by the locations of the mounting holes in the side plate, it was not always possible to obtain downwash surveys at the longitudinal station and angle of attack for which photographs of the flow pattern had previously been obtained. The downwash surveys were corrected for stream-angle effects by subtracting the stream angles measured in the tunnel without the model present. The presence of a sidewash or pressure gradient between the top and bottom orifice positions could cause some error in the downwash measurement but, because of the small size of the cone, this effect was estimated and found to be negligible.

Several downwash surveys were made both with dry air in the tunnel and with water added to the air stream to form a vapor screen. A comparison of these results indicated that the relatively high water content in the tunnel associated with the vapor-screen technique had a negligible effect on the local stream angle.

Models and Support

The three types of models used during this investigation were the wing-alone models, a body-alone model, and the wing-body-combination models as shown in figure 3. The wing models, which varied in aspect ratio from 0.67 to 4.0, were of triangular plan form with 8-percent-thick symmetrical double-wedge airfoil sections. For wing-alone tests the wings were supported from the rear by a 1/4-inch-wide strut originating from a point aft of the ridge line and extending rearward to a 3/4-inch-diameter sting support as shown in the photograph of figure 1(b). The body-alone model consisted of a conical nose having a semiapex angle of 15° and an ogival transition section that faired into a cylindrical afterbody 1.5 inches in diameter. The fineness ratio of the body was 10. The wing-body combinations were formed by adding the various wing models to the body. All the wings had a common chord of 3 inches at the wing-body juncture.

In addition to these basic models, a limited number of tests were made with two other aspect ratio 4.0 wing-body models. The first of these was a 0.42-scale version of the basic model having an extended afterbody to give a fineness ratio of 25.3. The second model was a 0.75-scale version of the basic model with all-movable wings whose angle of incidence could be varied from 0° to 12° .

TESTS AND RESULTS

The experimental investigation consisted primarily of vapor-screen observations and downwash surveys of the flow in the vicinity of the models for the test conditions given in table I. Systematic tests to determine the effects on the vortex wake of wing aspect ratio, angle of attack, and streamwise distance behind the wing for the wings, body, and wing-body combinations comprised the major portion of these tests. Limited tests were also performed to investigate these effects for changes in afterbody length, wing incidence, Reynolds number, and Mach number for the wing-body combinations, as indicated in table I.

The results of the investigation are presented in figures 4 to 39 of which figures 4 to 23 are representative vapor-screen photographs, and figures 29 to 39 are downwash distributions as indicated in table I. A sketch of the configuration and the wing-leading-edge Mach line is given with each group of vapor-screen photographs, and the viewing position in each case is indicated on these sketches. Table II presents a series of sketches which summarize the wake geometry at a possible missile tail location for the wings, body, and combinations observed from the vapor-screen photographs. The paths of the predominant free vortices at a given angle of attack and the variation in the vortex positions with angle of attack at a particular downstream position for the body and several representative wing-body combinations are plotted in figures 24 to 27, as obtained from the vapor-screen photographs by means of the grid-superposition procedure. Vapor-screen photographs, in addition to those presented in figures 4 to 23, were obtained at intermediate streamwise stations to define the vortex paths given in figures 24 and 26.

A limited study of the boundary-layer flow on the surfaces of the $A = 1.33$ and $A = 4.0$ wing-body combinations was made by means of the china-clay method, which is described in reference 20. The models were given a coating of china clay, which dries a dull white, and then were sprayed with a mixture of eugenol and ethyl phthalate just before being placed in the wind tunnel. The regions of laminar or turbulent boundary-layer flow on the model became apparent when the faster drying turbulent-flow regions began to appear white in contrast to the darker and still wet regions of laminar boundary-layer flow. Still slower to dry than the laminar-flow areas and the last to turn white were the regions of separated flow. Plan-view photographs of the models showing these contrasting regions of boundary-layer flow were obtained and are presented in figure 28.

DISCUSSION

Geometric Characteristics of the Vortex System

The nature and behavior of the vortex systems in the vicinity of the models are shown in the vapor-screen photographs of figures 4 to 23. The following general characteristics of these photographs are noteworthy as an aid in the interpretation of the observed flow-field patterns:

A region of concentrated vorticity appears as a dark circular area, and a vortex sheet (which includes the viscous wake) appears as a dark line of varying width. This correspondence was established by detailed flow-angle surveys of the present investigation, the results of which are presented in a later section. The direction of rotation of the vortices is discernible in some of the vapor-screen photographs (see, e.g., fig. 15(a), $\alpha = 12.8^\circ$).

For the isolated-wing tests, the vapor-screen photographs show that the model sting support itself (see fig. 1(b)) introduced some additional patterns into the flow field. Figure 6(b), for example, shows two pairs of small spots behind the blunt base of the vertical supporting strut on the wing surface, one pair above the sting and one below. These vortices seem to be rapidly dissipated farther downstream (see fig. 7(b)). The second effect of the support observed from the photographs is the creation of a pair of cross-flow-separation vortices on the lee side of the cylindrical portion of the support at the large angles of attack (see, e.g., fig. 7(b), $\alpha = 23.2^\circ$). It is believed that these support effects have only a small influence on the wing vortex wake because the support vortices are relatively far removed from the wing wake.

The presence of shock waves in the flow field is evidenced by a sharp line of demarcation between a light and dark region in the flow field. A conical shock wave, for example, appears as a circle whose interior is lighter than its exterior. In the photographs taken at the most forward positions, portions of the circle corresponding to the shock wave from the body nose or wing apex may be seen (e.g., fig. 4(a)); for the wing-body combinations, both these shock waves are visible and appear approximately as two concentric contours (e.g., fig. 12(b)). In the photographs of the flow just behind the wings, two essentially horizontal lines of demarcation between a light and dark region appear equidistant above and below the vortex wake (e.g., fig. 13(d) at $\alpha = 13.0^\circ$). These lines correspond to the shock waves from the wing trailing edge and tend toward an elliptical shape as the vapor screen is moved downstream. The vapor-screen photographs also show the presence of shock waves in the cross-flow (flow normal to the model

longitudinal axis) field of the lowest-aspect-ratio wings and of the body at large angles of attack. For these cases (see, e.g., figs. 6(a) and 10, $\alpha = 23^\circ$) the vortex wake consists essentially of two concentrated regions of vorticity close together and rotating in the opposite direction. It is observed that as the cross flow just outboard of the vortices progresses around the vortex boundary, an expansion (darkening of the vapor-screen field), or high-velocity region, occurs which terminates in a shock wave near the top of each vortex. As the air flows downward between the two vortices, another similar region is evident which creates one or two normal shock waves joining these vortices. An estimate of the Mach number in this region indicates that the flow approaching these observed shock waves is supersonic.

The effects of some important variables on the nature and behavior of the vortex systems in the vicinity of the wings, body, and wing-body combinations, respectively, are analyzed and discussed in the following paragraphs.

Wings.— The vapor-screen photographs, figures 4 to 8 and table II(a), show that the character of the wing trailing vortex wake is strongly influenced by the angle of attack and aspect ratio. As a general effect, the size of the wake is observed to increase with angle of attack, which would be expected from the familiar relationship that the strength of the trailing vortex system behind a wing is proportional to the lift and, hence, to the inclination of the wing. The initial geometry of the wake as it leaves the wing is shown in figures 4 and 5 to vary markedly with aspect ratio and angle of attack. The photographs of figure 5 show that for all aspect ratios, the vortex wake near the wing trailing edge approaches a flat sheet as the angle of attack tends toward zero. As the angle is increased, the wake at the trailing edge of the low-aspect-ratio wings develops into a single region of concentrated vorticity which leaves the wing surface forward of the trailing edge (see fig. 4(a)). The corresponding wake for the high-aspect-ratio wings remains essentially a flat sheet and continues to leave the wing at the trailing edge (see also fig. 4(b)). These differences in the initial geometry of the wake are caused by flow-separation effects on the upper wing surface which depend upon the wing angle of attack and aspect ratio. The vapor-screen photographs of figures 5 to 8 show that as the vortex wake progresses downstream, it gradually becomes warped and breaks or rolls up into one or more pairs of discrete vortices. The rate at which this development occurs is observed to increase with angle of attack and to decrease with aspect ratio. It is shown in figures 5 to 8 that at small angles of attack, the trailing vortex wake tends to roll up into a single vortex far behind each wing panel for all aspect ratios. At large angles of attack (18° and 23°), however, the wake for aspect ratios up to 2.0 develops into a single vortex behind each wing panel; whereas the wake for an aspect ratio of 4.0 develops

into two such vortices, the inboard pair increasing in size relative to the outboard pair as the angle of attack is increased.

For those conditions in which the vortex wake leaves the wing trailing edge as a flat sheet (small angles of attack or large aspect ratios), the observed distortion or rolling up of the trailing vortex sheet as it progresses downstream and the dependence of the magnitude of these motions on the wing angle of attack and aspect ratio are in qualitative accord with the theoretical results of reference 9. These results show that for triangular wings having a fixed span load distribution, the rate of rolling up of the trailing vortex sheet is directly proportional to the lift coefficient and inversely proportional to the square of the aspect ratio. In addition, the ultimate geometry of the wake (number of vortices into which the vortex sheet rolls up) under these conditions is also in agreement with the theoretical predictions; that is, the results of reference 10 have shown that the vortex sheet from a wing having an elliptic spanwise load distribution theoretically rolls up into a single vortex behind each wing panel. Recent unpublished calculations have shown that the vortex sheet from a wing having a linear load distribution over all or a large part of the span rolls up into two such vortices.

Comparisons of the experimentally determined spanwise load distributions on triangular wings with those predicted by supersonic linearized wing theory are given in references 21 and 22. It is shown that for small angles of attack, the measured spanwise load distributions on these wings (including a wing having its leading edge slightly ahead of its apex Mach cone) were nearly elliptical in nature. Such a distribution is predicted by theory for triangular wings having the leading edge behind the Mach cone. For the wing having its leading edge ahead of the Mach cone, this type of distribution results from detachment of the leading-edge shock wave, due to wing thickness effects and a subsequent subsonic flow over the wing leading edge. This elliptic span load distribution thus accounts for the experimentally observed and theoretically predicted rolling up of the trailing vortex sheet into a single vortex behind each wing panel at small angles of attack. The experimental results of references 21 and 22 further show that as the angle of attack is increased, a progressive change occurs from an elliptic type of span load distribution to an essentially linear distribution. Thus, for the largest-aspect-ratio wing from which the wake leaves the trailing edge as a sheet, a correspondence also exists at large angles of attack between the spanwise load distribution and the observed nature of the vortex wake which agrees with the theoretical prediction of the vortex-wake geometry for a linear span load distribution. However, no such agreement is present for the lower-aspect-ratio wings ($A = 0.67$ to 2.0) at large angles of attack, due to the fact that the vortex wake from each wing panel is effectively rolled up into a single vortex before it reaches the trailing edge.

Body.- The vapor-screen photographs of figures 9 to 11 and the sketches of table II(a) show that as the body angle of attack is increased, a symmetrical pair of vortices is formed on the lee side which increases in strength and is discharged as two free vortices. This effect is in accord with the results of reference 23 in which a study was made of the cross flow around inclined bodies of revolution. This study showed that the body vortices are the result of viscous cross-flow separation and that the accompanying viscous cross force increases with angle of attack. Thus, the strength of the body vortices would be expected to increase with increasing angle of attack, as observed in the photographs of the present investigation. At the largest angles of attack (e.g., $\alpha = 23^\circ$), the body photographs (figs. 9 to 11) show the same transonic cross-flow phenomena which were observed for the lowest-aspect-ratio wings at large angles of attack, that is, an oblique shock wave near the top side of each body vortex and a normal shock wave between these two vortices.

The paths of the body vortices (fig. 24) show that for a fixed angle of attack, the two vortices move apart to an essentially constant lateral spacing and move downward along an approximately straight line having an inclination less than that of the body. Figure 25 shows a similar motion of the vortices at a fixed downstream station as the result of an increase in angle of attack.

Wing-body combinations.- The vapor-screen photographs of figures 12 to 17 and the sketches in table II show that the vortex wake induced by the wing-body combinations is essentially a superposition of the wake induced by the wings (figs. 4 to 8) and that induced by the body (figs. 9 to 11). It is noted that the dependence of the wing vortex wake on the angle of attack and aspect ratio and the formation of body cross-flow vortices for these combinations is similar to the effects discussed previously for the wings and body. The paths of the predominant vortices for three wing-body combinations (fig. 26) show an inward and upward motion of the wing-tip vortices relative to the free stream which increases with increasing angle of attack. The inboard wing vortices (figs. 26(b) and (c), $\alpha = 18^\circ$), however, exhibit a slightly downward motion. Figure 27 also shows the influence of angle of attack on the vortex positions. The body-vortex paths and their variation with angle of attack appear to be similar to those observed for the isolated body (figs. 24 and 25).

China-clay photographs of the $A = 1.33$ and 4.0 wing-body combinations (fig. 28) show evidence of the separation vortex formed on the upper wing surfaces at large angles of attack. The dark area on each surface near the midspan position and originating at the leading edge of the wing-body juncture indicates the locations of these vortices.

The addition of the body to the wings has three effects on the trailing vortex system, the magnitude of these effects depending on the size of the body relative to the wing. First, the wing lift and spanwise load distribution are changed by the addition of the body, and, consequently, the magnitude and initial distribution of the vorticity in the wing wake are changed correspondingly. Second, the resulting motion of the trailing vortex wake from the wing is influenced by the presence of the afterbody (portion behind the wing) which produces, effectively, an image vortex system of the wing wake. Third, this motion is also affected by the velocity field associated with the cross flow around the body and, at moderate or large angles of attack, one or more additional pair of vortices are introduced into the flow field by virtue of separation of the body cross flow. This effect is evidenced by the presence of the body cross-flow separation vortices in the vapor-screen field. For the isolated body (figs. 9 to 11) a single symmetrically disposed vortex pair is discharged from the upper side, whereas, for the wing-body combinations (e.g., fig. 16(c), $\alpha = 18.2^\circ$), two such vortex pairs are generated, one from the forebody and one from the afterbody. The paths of these body vortices are shown in figures 24 and 26. The observed differences in the body vortices caused by the addition of a wing is due to the elimination of the cross flow around the portion of the body in combination with the wing and to the wing downwash field. Close examination of the photographs indicates that the vortex pair from the forebody diminishes in size as it progresses downstream; whereas the vortices from the isolated body or from the afterbody tend to maintain or increase their size. This effect seems reasonable since the forebody vortices cease to be generated downstream of the wing leading edge and, hence, become disconnected from the body and gradually diminish in strength due to viscous dissipation and mutual interaction with adjacent vortices. The vortices from the isolated body or from the afterbody, on the other hand, presumably are being amplified in strength as they travel downstream because of the discharge of vorticity all along the body. The marked influence of the wing induced flow field on the body cross flow is evident from a comparison of the vapor-screen photographs for the body (e.g., fig. 10) with those for the wing-body combination (e.g., fig. 15). It is observed that the addition of the wing causes a reduction in the apparent strength of the body vortices, indicating a suppression of the body cross flow as would be expected from the influence of the wing downwash field. It is also noted that addition of the wing causes these vortices to move farther apart, especially at the greatest downstream positions and at the largest angles of attack (cf. figs. 11 and 16 at $\alpha = 23^\circ$). This effect is due to the fact that the body vortices are located below the wing wake and, hence, are in an outwash flow field. Figure 17, which shows a detailed sequence of photographs for a low-aspect-ratio wing-body combination at a large angle of attack, illustrates the development and mutual interaction of the vortex systems generated by the body and by the wing.

Theoretical calculations have been made of the motions of the trailing vortex wake behind the wings of two representative wing-body combinations which were tested in the present experimental investigation at a Mach number of 2. These calculations, the results of which are not presented in this report, were made by means of the method described in the appendix. One combination was assumed to have an elliptic-type spanwise load distribution over the exposed wing panels ($A = 0.67$ wing-body combination), and the other had a linear distribution over the outer portion of the span ($A = 4$ wing-body combination). The span load distribution on each wing panel was replaced by ten vortices, and the body by the corresponding image system. The subsequent motions of these vortices were then calculated in downstream intervals of one-half body radius, which was found to be adequate for these calculations. The results showed that the vortex sheet for the low-aspect-ratio case rolled up into a single concentrated region of vorticity behind each wing panel, as would be expected. This result is in agreement with the corresponding vapor-screen observations of the present investigation and also with the theoretical results for an isolated wing as reported in reference 11 and as previously discussed. For the high-aspect-ratio case, the portion of the wake associated with the linear loading tends to roll up into two regions of vorticity corresponding to two vortices behind each wing panel rotating in the same direction. This result is also the same as the corresponding theoretical result for the isolated wing as discussed previously and is in agreement with the vapor-screen observations for this wing-body combination at large angles of attack. Thus, it is apparent from both experimental and theoretical evidence that the basic nature and behavior of the wing trailing vortex system are not changed by the presence of the body.

The influence of the body flow field on the nature of the vortex wake behind the aspect ratio 4 wing-body combination is indicated by the vapor-screen photographs of figure 19 in which the effect of the body inclination is shown for a given wing angle of attack. Perhaps the most readily noticeable effect is the increase in the distance of the wing wake above the body. This effect is primarily one of geometry; that is, the wing wake tends to trail in approximately the stream direction, and the inclined body moves farther away from the wake with increasing downstream distance. The presence of the upwash field adjacent to the inclined body also contributes to this effect. The major difference in the nature of the trailing vortex wake due to the inclination of the body appears to be in the presence of the inboard vortex from each wing panel. It is observed that with the body at zero angle of attack ($\alpha = 0^\circ$, $i_w = 12^\circ$), this vortex is not present behind the wing as it is for the body inclined with the wing at zero angle ($\alpha = 12^\circ$, $i_w = 0^\circ$). The photographs just behind the wing trailing edge ($x/c_r = 0.1$) show that for the body at zero inclination, the wing vortex sheet appears as a thin relatively uniform line; whereas that for the inclined body shows a pronounced thickening near the body which

becomes entrained in a discrete inboard vortex farther downstream. Thus, it appears that these differences in the vortex wake due to the body inclination stem, primarily, from the resulting flow changes over the wing surfaces rather than from the cross flow over the afterbody. These flow changes are presumably caused by the induced flow field from the forebody which effectively subjects the wing elements to an increased angle of attack, particularly near the body, and thereby serves to promote early separation of the boundary layer in this region, with the consequent change in the span load distribution and the formation of a vortex behind the wing and near the body.

As the vortex wake progresses to large distances behind the wing, it is observed from figure 18 that a gradual asymmetry develops in the body and wing vortices of the aspect ratio 4 wing-body combination. This asymmetry is believed due to the characteristic behavior of the body cross flow at large angles of attack and at a large number of diameters behind the body nose. Reference 23 has shown that under such conditions the body cross-flow vortices become asymmetrically disposed and are shed alternately from the body followed by similar shedding of subsequent vortices as the body inclination is further increased. Vapor-screen studies of the isolated body corresponding to figure 18 show that the body vortices are asymmetric in those cases where a similar condition exists for the wing-body vortices. Thus, it appears that the asymmetry in the wing vortices is due to the influence of the body cross flow.

The influence of variations in Reynolds number on the observed vortex-wake patterns behind two representative wing-body combinations is shown in the vapor-screen photographs of figure 20. It is observed that an increase in Reynolds number from 0.3 to 1.0 million results in a reduction in the size of the outboard vortex relative to that of the inboard vortex for the $A = 1.33$ wing-body combination at an angle of attack of 5° . A similar change also occurs in the size of the body vortices relative to that of the wing vortices for both wing-body combinations at an angle of attack of 18° . These results are consistent with the previously discussed effects that the outboard vortices from low-aspect-ratio wings and the vortices from the body are associated with flow separation; that is, the tendency of a flow to separate decreases as the Reynolds number is increased and, thus, the relative size of these vortices would also be expected to show a corresponding reduction, based on the presumption that the observed size of the vortex is directly related to the size of the vortex core.

The influence on the observed vortex-wake patterns of a change in Mach number from 1.5 to 2.0 is shown by a comparison of the vapor-screen photographs of figures 21, 22, and 23 with those of figures 13, 15, and 16, respectively. Such a comparison indicates that no essential change in the number, arrangement, or behavior of the vortices comprising

the wake occurs as the result of this Mach number variation. It is noteworthy that this result includes the $A = 2.67$ wing-body combination for which the wing leading edge is supersonic (swept ahead of the Mach cone) at $M = 2.0$ and subsonic (swept behind the Mach cone) at $M = 1.5$. The vapor-screen photographs also indicate, however, that a change in Mach number affects the apparent intensity of the body cross-flow vortices relative to that of the wing vortices. Figures 13(b) and 21(a) at $\alpha = 18^\circ$, for example, show that an increase in the size and stage of development of the body vortices relative to those of the wing vortices occurs as the Mach number is increased. This effect is presumably due to the decrease in lift-curve slope $dC_L/d\alpha$ of the wing and, hence, in the trailing vorticity at a given angle of attack as the Mach number is increased, and also to a corresponding increase in strength of the body cross-flow vortices. The latter effect is associated with an increase in cross-flow drag coefficient with Mach number which occurs because both the cross-flow Mach number and Reynolds number at angles of attack above approximately 13° are in the ranges where such an increase would be expected (see ref. 23).

Downwash Characteristics

The experimentally determined spanwise distributions of downwash are presented in figures 29 to 39 for the wings, body, and wing-body combinations, and are discussed in the following paragraphs. The model cross section and the location of the prominent discrete vortices (measured from the vapor-screen photographs) relative to the downwash-survey line are also shown in these figures. The downwash results are correlated with the geometric characteristics of the vortex system as discussed in the preceding section and are compared in a number of representative cases with the corresponding results obtained by the theoretical calculations described in the appendix.

Wings.— Figure 29 presents spanwise downwash distributions near the center of the vortex wake at two longitudinal positions behind the $A = 1.33$ wing. For these positions the influence of the model support on the induced flow field would be expected to be small because of the small lateral dimension of the support. These distributions show an abrupt reversal in the flow direction from a large downwash inboard to a large upwash angle near the midsemispan position. Outboard of this location, only upwash angles occur which vary abruptly in the region between the midspan location and that of the wing tip. Outboard of the tip, the upwash diminishes smoothly to zero. An examination of the corresponding vapor-screen photographs (figs. 5(b) and 6(b)) shows that these downwash distributions are in good qualitative correlation with the observed geometry of the vortex wake; that is, near the midsemispan position, a strong vortex or region of vorticity is present which causes

the large change from downwash to upwash. Farther outboard, a weaker region of vorticity is present which gives rise to the sharp variations in upwash at this spanwise location. At $x/c_r = 0.1$ (fig. 29(a)) it is noted that a large number of these variations occur outboard of the predominant vortices, as would be expected from the corresponding wake pattern (fig. 5(b)) in which the remainder of the vorticity appears to be distributed. At $x/c_r = 0.6$, however, only two double reversals in the slope of the upwash curve are present in this region (fig. 29(b)) which correspond to the two discrete vortices in the wake near the wing tip (fig. 6). It appears from both the downwash distribution and the vapor-screen photographs that the outer vortex in this case has negative rotation, which implies a small negative loading near the wing tip.

Body.- The experimental downwash field in the vicinity of the isolated body is presented in figures 30 and 31, and the corresponding results from two-dimensional potential-flow theory in the absence of vortices are shown for comparison. These results show that the downwash distributions on or near the meridian plane ($z = 0$), figure 30, are essentially in agreement with the theoretical results for all angles of attack. On the basis of these and previous experimental results, it would be expected that the entire downwash field on the windward side of the body ($z < 0$) would also be in agreement with that predicted by potential-flow theory. The spanwise downwash distributions on the lee side of the body ($z > 0$) at moderate and large angles of attack (fig. 31), however, are considerably different from those predicted by potential-flow theory, due to the formation of body cross-flow separation vortices as previously discussed. The positions of these vortices are indicated in the downwash distributions of figures 31. The downwash distribution computed by means of potential-flow theory without vortices for the meridian plane ($z = 0$) is shown for comparison with the experimental distributions on the lee side of the body. It is noted that in all cases, these theoretical results are in considerably closer agreement with experiment over most of the span than the potential-theory results for the actual vertical location. This result might be expected from the concept that the separated air on the lee side of the body may be considered to act somewhat as an extension of the boundary of the body.

Wing-body combinations.- The experimental downwash distributions downstream of the wing-body combinations are shown in figures 32 to 39, and the corresponding theoretical results obtained from the method described in the appendix are shown for comparison in several representative cases.

Consider first the downwash field behind the low-aspect-ratio wing-body combinations at small angles of attack. Figure 32 shows a downwash distribution near the wing wake which is characteristic of an isolated discrete vortex having positive rotation. The corresponding vapor-screen photograph (fig. 14) shows that the vortex wake from each

wing panel actually does consist of a single vortex. The theoretical distribution of downwash with body cross-flow effects included is seen to be in close agreement with the experimental results, regardless of whether one or three vortices are used to replace the flow field from each wing panel. A comparison of the two theoretical curves with and without body cross flow shows that the body cross-flow effects on the induced flow are of the same order of magnitude as those due to the wing wake, despite the close proximity of the survey station to the wing vortex wake. This result may be attributed to the large size of the body relative to the wing for this configuration. Figure 38 shows the downwash distribution behind this wing-body combination at the same angle of attack, but at a farther distance behind the wing and farther away from the wing wake in the windward direction. As in the previous case (fig. 32), this distribution is in agreement with the theoretical results. In this case, the downwash is caused almost entirely by the body cross-flow field. The calculated effect of the wing wake is negligible because of the relatively large vertical distance between the survey station and the wing trailing vortex system as shown by the vortex-position sketch in figure 38.

The downwash distributions behind the wing-body combinations having subsonic-leading-edge wings at large angles of attack are shown in figures 33, 35, and 36. The vapor-screen photographs of figures 15 and 16 show that the vortex system for these combinations consists essentially of a single vortex from each wing panel and a pair of body cross-flow separation vortices. It is noted that the lateral positions of the wing vortices as indicated by the downwash distributions are in close agreement with the corresponding values obtained from the vapor-screen photographs. In some instances, the influence of the body cross-flow field on the downwash distributions near the body or the body vortices can be seen (see, e.g., figs. 33 and 36(b)) by the departure of these distributions from those characteristic of a single wing vortex. The downwash distribution of figure 33 and the corresponding vapor-screen photograph of figure 14(b), $\alpha = 12.8^\circ$, indicate the presence of a relatively weak vortex outboard of the principal wing vortex. The spanwise locations of these two vortices as measured from the vapor-screen photographs are in reasonable agreement with the locations indicated by the downwash distributions (point midway between peaks for each vortex).

The downwash distributions calculated by means of the line-vortex method are shown in figures 35 and 36 for the $A = 0.67$ and 2.0 wing-body combinations at large angles of attack. For these calculations, a single line vortex was used to represent the trailing vortex wake. A comparison of these downwash distributions shows that the calculated results are only in qualitative agreement with the experimental results. The lack of quantitative correlation is primarily due to the inability of these calculations to predict accurately the position of the wing

vortex in the yz plane. In all cases the theoretical vortices are slightly below and considerably more outboard than the observed vortices. This difference is believed to be due primarily to differences in the wing span load distribution between theory and experiment at large angles of attack and to the approximate method used to account for the effects of the body cross flow on the wing vortex paths and on the downwash distributions at the specified distance behind the wing. As discussed previously, experimental results show that increasing angles of attack cause an inboard shift in the wing center of vorticity and, hence, in the location of the trailing vortex system, which is in the direction necessary to bring the theoretical vortices of the present calculations into conformity with the actual vortices. Also, as discussed previously in connection with the body cross flow at large angles of attack, the lateral downwash distribution on the lee side of the body is taken as the theoretical potential-flow distribution corresponding to the meridian plane ($z = 0$). Along this plane the sidewash is theoretically zero. It is noted, however, that the downwash survey of figure 35(c) was made on the lee side of the body cross-flow separation vortices and, hence, the assumed body flow field in this region may be considerably in error; that is, the downwash distribution would be different, and the sidewash would not be zero, due to the convergence of the flow (inwash) behind the body vortices. Thus, if these effects were accounted for, it is clear that the theoretical wing vortices would lie farther inboard as do the actual wing vortices. No completely analytical solution to this flow field exists, but the downwash comparison of figures 33, 35, and 36 indicate that such a solution must be found in order to predict accurately the induced flow field behind wing-body combinations at large angles of attack which incorporate a large body relative to the wing.

Spanwise distributions of downwash behind the $A = 4$ wing-body combination at small angles of attack are given in figures 34(a) and 39(a). It is noted that the magnitude of the downwash is small and the distributions are smooth, indicating an essentially continuous sheet as observed in figures 14 to 16. The theoretical downwash distribution computed by the line vortex method is shown in figure 34(a). This figure shows that the use of three vortices afforded a closer approximation with experiment than a single vortex, which follows from the previously observed character of the vortex wake. Consequently, the use of a still larger number of theoretical vortices to replace the wake would be expected to give even closer agreement with the experimental results. The effect of the body cross flow on the theoretical downwash distribution computed with one vortex representing each wing is also shown in figure 34(a). It is noted that this effect is important only near the body, as would be expected.

Spanwise downwash distributions behind the aspect ratio 4 wing-body combination at large angles of attack are shown in figures 34(b),

37, 39(b), 39(c), and 39(d) for various vertical locations. As discussed previously, the vortex wake associated with this configuration at large angles is characterized by two vortices from each wing panel, one near the wing tip and one near the body, and a pair of body cross-flow separation vortices as shown by the vapor-screen photographs of figures 14 to 16. The downwash distributions near the wake (figs. 34(b), 37(b), 37(c), 39(c), and 39(d)) show the influence and indicate the relative strengths of the two predominant wing vortices. From the experimental change in downwash through the centers of the tip and inboard wing vortices (figs. 39(c) and 39(d), respectively), the indicated strength of the inboard vortex is approximately 60 percent of the tip vortex strength. Downwash distributions calculated by the line vortex method using a single vortex to represent the wing wake are shown in figure 37. A comparison of these results with the experimental data shows poor agreement which is primarily due to the use of a single theoretical vortex to replace the wing wake, whereas two discrete vortices actually exist. The use of two theoretical vortices of equal strength would presumably result in some improvement in the downwash prediction, but in order to obtain quantitative agreement it appears that the inner vortex should be assigned a lower strength than the outer vortex, as indicated by the experimental results. However, no existing theory is capable of determining this strength distribution. A second factor contributing to the differences in downwash between theory and experiment is the approximate method used in accounting for the body cross flow at large angles of attack, as discussed previously. The influence of this factor would be manifest primarily in the region near the body. Another approximation involved in these calculations is the use of a theoretical wing span load distribution which assumes an attached leading-edge shock wave. Due to the combined angle of attack and leading-edge sweepback of this wing, however, the shock wave becomes detached from the leading edge with a resulting change in the spanwise load distribution.

CONCLUSIONS

An investigation has been conducted to observe the nature and behavior of the vortex wake behind triangular wings of various aspect ratios alone and in combination with a pointed cylindrical body at supersonic speeds, and to measure the downwash associated with these vortex systems. The results of the experimental investigation and of theoretical calculations have led to the following conclusions:

1. Downwash-survey results generally confirm the flow-visualization observations as to the identity and location of the vortices in the flow field.

2. The trailing vortex wake from the wings alone or in combination with the body at small angles of attack is observed to leave the wing trailing edge as a sheet and proceeds to roll up into a single region of vorticity behind each wing panel as it progresses downstream. The rate at which this rolling up takes place increases with angle of attack and decreases with increasing aspect ratio. These results are in accord with effects determined by theoretical calculations. For the case of high-aspect-ratio wings at large angles of attack, the wing trailing vortex sheet rolls up into two regions of vorticity behind each wing panel. This result would also be anticipated by theory, due to the change in the spanwise load distribution from essentially elliptic at small angles of attack to partially linear at large angles.

3. The vortex wake from the low-aspect-ratio wings at large angles of attack fails to leave the trailing edge as a sheet since the vorticity discharged from each wing panel rolls up into a single vortex ahead of the trailing edge.

4. The presence of the body in combination with the wings affects the position of the wing vortex wake. The magnitude of this effect depends on the size of the body relative to the wing. At moderate or large angles of attack, two more pairs of vortices are introduced into the flow field by the body as a result of body cross-flow separation. One pair is discharged from the forebody and another from the afterbody.

5. The downwash measured in the neighborhood of the isolated body at small angles of attack was in good agreement with that predicted by two-dimensional potential-flow theory for the flow about a circular cylinder. At large angles of attack, the influence of viscous cross-flow separation was found to produce large differences in the flow field close to the vortices associated with this separation.

6. At small angles of attack, the experimental downwash field behind wing-body combinations having low-aspect-ratio subsonic-leading-edge wings was closely predicted by theoretical calculations in which a single vortex was used to replace the wake from each wing panel. For a combination having an aspect ratio 4 supersonic-leading-edge wing, three vortices were required in the theoretical calculations to predict the measured downwash distributions. At large angles of attack the agreement between the experimental and theoretical downwash was, at best, only qualitative, primarily as the result of flow-separation effects on the wing and body.

Ames Aeronautical Laboratory
National Advisory Committee for Aeronautics
Moffett Field, Calif.

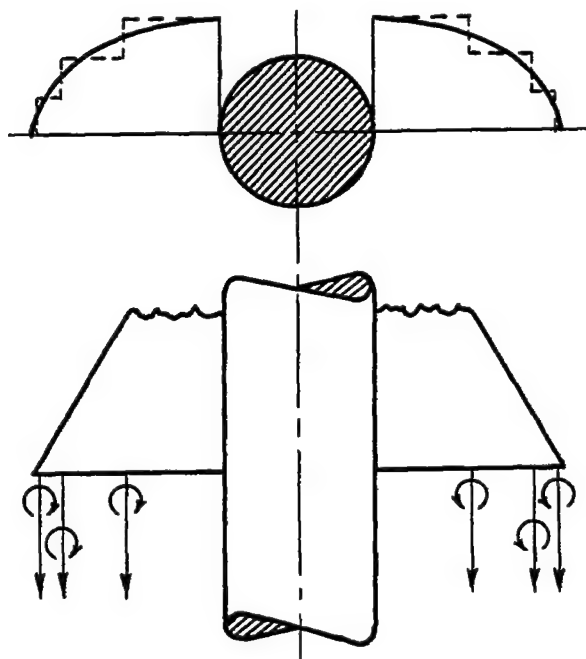
APPENDIX

THEORETICAL CALCULATION OF DOWNWASH

Description of Method

The theoretical downwash fields behind the wing-body combinations of the present investigation have been calculated by a method in which the trailing vortex wake from the wing is represented by a number of discrete line vortices. The elements of this method are described in the following paragraphs.

Initial distribution of vorticity.- The trailing vortex wake is assumed to originate at the wing trailing edge and, for this condition, the initial spanwise distribution of trailing vorticity is equal to the spanwise gradient of the wing circulation distribution. For the cases considered in the present investigation, the circulation distribution is theoretically proportional to the span loading distribution, and the method used in the present calculations for the estimation of these distributions are described in a later section entitled "Wing Span Load Distribution." The initial distribution of the trailing line vortices representing the vortex wake was obtained from the spanwise circulation (span loading) distribution in the following manner: The circulation distribution was replaced by a step function, as shown in sketch (a), representing a given number of line vortices originating at the wing trailing edge. The strength of each vortex is proportional to the height of its step on the circulation-distribution curve and, for convenience, the same strength was assigned to all the vortices for a given condition in the present calculations. The initial spanwise locations of the vortices were chosen so that the resulting area under the stepped curve was the same as that for the circulation curve. The bound vorticity, which represents the wing-chord loading, has been neglected, as the probable tail-plane locations considered in the present downwash calculations are sufficiently far downstream to justify this simplification.

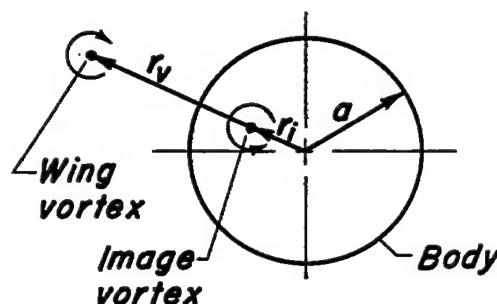


Sketch (a)

Effects of the body.- The presence of the body in combination with a wing influences the spanwise load distribution over the exposed wing panels, as discussed in the section "Wing Span Load Distribution," and thus contributes to the initial distribution of the wing trailing vorticity. The presence of the afterbody (the portion of the body behind the wing trailing edge) influences the wing trailing vortex paths and the induced flow field in two ways. First, it imposes the boundary condition that the flow at the body surface shall be tangential to the surface. This condition is satisfied in the wing trailing vortex field by the introduction of an image line vortex within the body corresponding to each wing vortex. At any given streamwise station, each of the image vortices is located on a radial line from the body center line to the corresponding external wing vortex, as shown in sketch (b), such that the relationship (see, e.g., ref. 24, p. 222)

$$r_v r_i = a^2 \quad (1)$$

is satisfied. Second, the afterbody induces a flow field because of its inclination to the air stream. This body flow field has not only a direct influence on the downwash at a given point behind the wing but also an indirect effect, since the wing vortex positions are changed by the body flow field which in turn changes the downwash due to the wing vortex system. These body effects are calculated from the potential-flow relationships for the induced velocities around an infinite circular cylinder (see ref. 25), the general expressions for which are



Sketch (b)

$$\frac{v}{V_0 \sin \alpha} = - \frac{2a^2 yz}{(y^2 + z^2)^2} \quad (2a)$$

$$\frac{w}{V_0 \sin \alpha} = a^2 \frac{y^2 - z^2}{(y^2 + z^2)^2} + 1 \quad (2b)$$

At large angles of attack, the flow on the lee side of long bodies of revolution has been shown (ref. 23) to depart seriously from the potential-type flow due to the influence of viscous cross-flow separation. For such cases in the present calculations (figs. 35 to 37), the induced velocities on the lee side of the body were computed from equations (2a) and (2b) with $z = 0$. The resulting relations were found to predict the experimental induced flow field in this region to a

closer degree of approximation than the relations using the actual values of z , as discussed in the text.

Vortex paths.- The paths of the wing trailing vortices were determined by means of a stepwise numerical process in which the incremental lateral and vertical displacement of each vortex is obtained from superposition of the displacements corresponding to the induced velocities caused by each of the remaining wing vortices, the image vortices, and the body cross-flow field (component of the flow field normal to the body axis). It was assumed that the wing and image vortices have the induced-flow characteristics of a two-dimensional line vortex (see ref. 25, p. 128), and thus the expressions for the sidewash and downwash velocities induced by a two-dimensional line vortex

$$v = - \frac{\Gamma}{2\pi} \frac{z - z_v}{(y - y_v)^2 + (z - z_v)^2} \quad (3a)$$

$$w = \frac{\Gamma}{2\pi} \frac{y - y_v}{(y - y_v)^2 + (z - z_v)^2} \quad (3b)$$

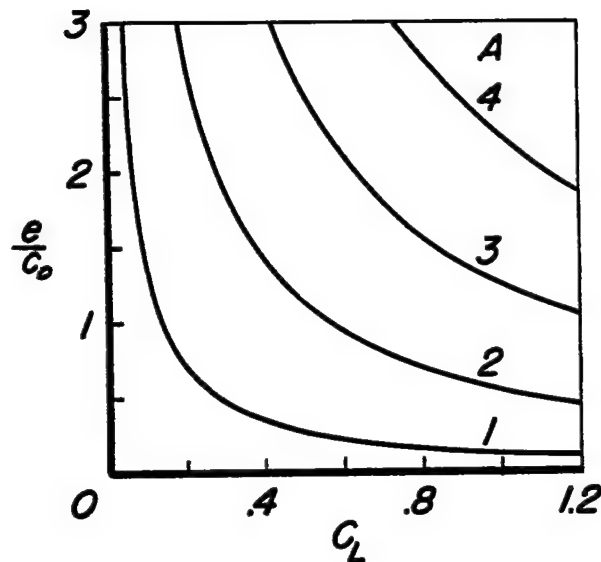
have been used in the present calculations to obtain the vortex paths.

The number of line vortices used to approximate the trailing vortex wake and the size of the streamwise increments employed in the stepwise calculations is dependent on the precision to which the downwash downstream of the wing is desired. In the interests of minimizing the computational labor, it is clearly desirable to use the smallest number of vortices and the largest streamwise increment consistent with this precision. The degree to which the vortex sheet is fully rolled up at a specified distance behind the wing panels influences to a large extent the number of vortices and the size of the streamwise increment necessary for these calculations. It has been shown in reference 10 that the degree of rolling up at a given distance in wing spans behind the trailing edge of a wing is directly proportional to the lift coefficient and inversely proportional to the aspect ratio. For triangular wings having an elliptic span load distribution, the distance in root-chord lengths required for the vortex sheet to become fully rolled up is given by the expression

$$\frac{e}{c_o} = 0.14 \frac{A^2}{C_L} \quad (4)$$

Sketch (c), which is a plot of this relation, shows that for a large class of wings (small aspect ratio or large lift coefficient), the wing vortex wake in the vicinity of a probable tail location is rolled up and, thus, can be represented by a single vortex pair.

Calculation of downwash.— The downwash angle at a given point behind the wing was obtained from the summation of the downwash velocities induced by each of the wing trailing vortices, the corresponding image vortices inside the body, and the body cross-flow field. These velocities were computed by the relations previously discussed.



Sketch (c)

One of the principal purposes of the present theoretical calculations was to indicate the degree to which the use of a single line vortex approximates the experimentally measured downwash field for the various test conditions of the present investigation. Consequently, calculations were first performed for a single vortex pair representing the wing wake. The corresponding downwash distributions were then computed and compared with experiment. When large differences existed from this comparison, the calculations were repeated for a larger number of vortex pairs representing the wing wake.

Wing Span Load Distribution

As indicated previously, the distribution of loading over the span of the exposed wing is required in order to compute the induced flow field for wing-body combinations by the present method. The load distribution over triangular wings at supersonic speeds has been determined by means of linearized theory in references 27 and 28 for those cases in which the leading edge is swept behind the Mach lines from the apex, and in reference 28 for the leading edge ahead of the Mach lines. The corresponding loading on these wings in combination with a body has not been treated theoretically, except in the limiting case of slender wing-body combinations (ref. 29). It was found in the experimental

investigation of reference 30 (which was limited to small angles of attack), however, that the total lift of the wing-body combinations investigated could be predicted satisfactorily by a simple correction of the slender-body value by the ratio of the wing lift calculated from linear theory to that from slender-body theory. Thus, at a given angle of attack,

$$\left[\frac{C_L}{(C_L)_{S.B.}} \right]_C = \left[\frac{(C_L)_{L.T.}}{(C_L)_{S.B.}} \right]_W \quad (5)$$

On the basis of these results, it is assumed that the theoretical span load distribution over the exposed wing panels may be obtained from the expression

$$\left[\frac{c_l}{(c_l)_{S.B.}} \right]_{W(B)} = \left[\frac{(c_l)_{L.T.}}{(c_l)_{S.B.}} \right]_W \quad (6)$$

It is noteworthy that for triangular wings having subsonic leading edges

$$\left[\frac{(c_l)_{L.T.}}{(c_l)_{S.B.}} \right]_W = \left[\frac{(C_L)_{L.T.}}{(C_L)_{S.B.}} \right]_W \quad (7)$$

because the same type of span loading (elliptic) is predicted by both slender-body theory and linear theory. The total lift and lift distribution over the wings in the presence of a body computed from equations (5) and (6) would be expected to closely predict the experimental results only in those cases for which the total and section lift for the wing alone was closely predicted by linear theory. For cases in which such predictions are not realized, the substitution in equations (5) and (6) of experimental values of C_L and c_l , respectively, for those given by linear theory would yield more realistic results for the wing-body combination. Limited measurements of the span load distributions on triangular wings at supersonic speeds (refs. 21 and 22) are in reasonably close agreement with the results of linear theory at small angles of attack, but the agreement diminishes with increasing angles of attack because of such effects as flow separation, local shock-wave formations, and detachment of the leading-edge shock wave. Despite these differences, the span load distributions based on linear theory have been used in all the present calculations because of the lack of experimental measurements directly applicable to the wings of the present investigation.

REFERENCES

1. Lagerstrom, P. A., and Graham, Martha E.: Downwash and Sidewash Induced by Three-Dimensional Lifting Wings in Supersonic Flow. Douglas Rep. SM-13007, 1945.
2. Lomax, Harvard, Sluder, Loma, and Heaslet, Max. A.: The Calculation of Downwash Behind Supersonic Wings With An Application to Triangular Plan Forms. NACA Rep. 957, 1950. (Formerly NACA TN's 1620 and 1803)
3. Ward, G. N.: Calculation of Downwash Behind a Supersonic Wing. Aero. Quart., vol. I, May 1949, pp. 35-38.
4. Martin, John C.: The Calculation of Downwash Behind Wings of Arbitrary Plan Form at Supersonic Speeds. NACA TN 2135, 1950.
5. Mirels, Harold, and Haefeli, Rudolph C.: Line-Vortex Theory for Calculation of Supersonic Downwash. NACA Rep. 983, 1950. (Formerly NACA TN 1925)
6. Mirels, Harold, and Haefeli, Rudolph C.: Calculation of Supersonic Downwash Using Line Vortex Theory. Jour. Aero. Sci., vol. 17, no. 1, Jan. 1950, pp. 13-21.
7. Haefeli, Rudolph C., Mirels, Harold, and Cummings, John L.: Charts for Estimating Downwash Behind Rectangular, Trapezoidal, and Triangular Wings at Supersonic Speeds. NACA TN 2141, 1950.
8. Robinson, A., and Hunter-Tod, J. H.: Bound and Trailing Vortices in the Linearized Theory of Supersonic Flow, and the Downwash in the Wake of a Delta Wing. College of Aero. (Cranfield), Rep. No. 10, Oct. 1947.
9. Spreiter, John R., and Sacks, Alvin H.: The Rolling Up of the Trailing Vortex Sheet and Its Effect on the Downwash Behind Wings. Jour. Aero. Sci., vol. 18, no. 1, Jan. 1951, pp. 21-32.
10. Westwater, F. L.: The Rolling Up of the Surface of Discontinuity Behind an Aerofoil of Finite Span. R&M 1692, British A.R.C., 1936.
11. Perkins, Edward W., and Canning, Thomas N.: Investigation of Downwash and Wake Characteristics at a Mach Number of 1.53. I - Rectangular Wing. NACA RM A8L16, 1949.
12. Perkins, Edward W., and Canning, Thomas N.: Investigation of Downwash and Wake Characteristics at a Mach Number of 1.53. II - Triangular Wing. NACA RM A9D20, 1949.

CONFIDENTIAL

13. Perkins, Edward W., and Canning, Thomas N.: Investigation of Downwash and Wake Characteristics at a Mach Number of 1.53. III - Swept Wings. NACA RM A9K02, 1950.
14. Adamson, D., and Bostright, William B.: Investigation of Downwash, Sidewash, and Mach Number Distribution Behind a Rectangular Wing at a Mach Number of 2.41. NACA RM L50G12, 1950.
15. Graham, Martha E.: Some Linearized Computations of Supersonic Wing-Tail Interference. Douglas Rep. No. SM-13430, 1948.
16. Lagerstrom, Paco A., and Graham, M.E.: Aerodynamic Interference in Supersonic Missiles. Douglas Rep. No. SM-13743, 1950.
17. Lomax, Harvard, and Byrd, Paul F.: Theoretical Aerodynamic Characteristics of a Family of Slender Wing-Tail-Body Combinations. NACA TN 2554, 1951.
18. Wetzel, Benton E., and Pfyl, Frank A.: Measurements of Downwash and Sidewash Behind Cruciform Triangular Wings at Mach Number 1.4. NACA RM A51B20, 1951.
19. Edwards, S. Sherman: Experimental and Theoretical Study of Factors Influencing the Longitudinal Stability of an Air-to-Air Missile at a Mach Number of 1.4. NACA RM A51J19, 1952.
20. Gazley, Carl, Jr.: The Use of the China-Clay Lacquer Technique for Detecting Boundary-Layer Transition. General Electric Rep. No. 49A0536, 1950.
21. Boyd, John W., and Phelps, E. Ray: A Comparison of the Experimental and Theoretical Loading Over Triangular Wings at Supersonic Speeds. NACA RM A50J17, 1951.
22. Hatch, John E., and Hargrave, L. Keith: Effect of Reynolds Number on the Aerodynamic Characteristics of a Delta Wing at Mach Number of 2.41. NACA RM L51H06, 1951.
23. Allen, H. Julian, and Perkins, Edward W.: A Study of Effects of Viscosity on Flow Over Slender Inclined Bodies of Revolution. NACA Rep. 1048, 1951. (Formerly NACA TN 2044)
24. Lamb, Horace: Hydrodynamics. Sixth Ed., Dover Pub., 1945.
25. Glauert, H.: The Elements of Aerofoil and Airscrew Theory. Cambridge University Press, (MacMillan Co.), 1943.

26. Stewart, H. J.: The Lift of a Delta Wing at Supersonic Speeds. Quart. Appl. Math., vol. 4, no. 3, Oct. 1946.
27. Brown, Clinton E.: Theoretical Lift and Drag of Thin Triangular Wings at Supersonic Speeds. NACA Rep. 839, 1946. (Formerly NACA TN 1183)
28. Puckett, Allen E.: Supersonic Wave Drag of Thin Airfoils. Jour. Aero. Sci., vol. 13, no. 9, Sept. 1946.
29. Spreiter, John R.: The Aerodynamic Forces on Slender Plane- and Cruciform-Wing and Body Combinations. NACA Rep. 962, 1950. (Formerly NACA TN's 1662 and 1897)
30. Nielsen, Jack N., Katzen, Elliott D., and Tang, Kenneth K.: Lift and Pitching-Moment Interference Between a Pointed Cylindrical Body and Triangular Wings of Various Aspect Ratios at Mach Numbers of 1.50 and 2.02. NACA RM A50F06, 1950.

TABLE I.- TEST CONDITIONS AND INDEX OF RESULTS

M	R	i_w , deg	Configuration	α , deg	$\frac{x}{c_r}$	Figure	
						Vapor-screen photographs	Downwash distributions
2.0	1.6×10^6	0	Wings	18	-0.3	4	- - - -
				5 to 23	.1	5	29(a)
					.6	6	29(b)
					1.1	7	- - - -
					2.1	8	- - - -
			Body	5 to 23	0	9	- - - -
					1.1	10	- - - -
				3 to 19	1.7	- - -	30 and 31
				5 to 23	2.1	11	- - - -
			Wing- body combinations	5 and 18	-.3	12	- - - -
				5 to 23	.1	13	- - - -
					.6	14	32, 33, 34
					1.1	15	- - - -
				15 to 18	1.6	- - -	35, 36, 37
				3 to 14	1.8	- - -	38, 39
				5 to 23	2.1	16	- - - -
			A = 2 Wing body	18	0 to 2.3	17	- - - -
2.0	0.8×10^6	0	A = 4 Wing body	13 and 18	2 to 8	18	- - - -
	1.6×10^6	0 and 12	A = 4 Wing body	0 and 12	0, 1.0, and 2.0	19	- - - -
	0.3, 1.0, 1.6×10^6	0	A = 1.33 and 4.0 Wing body	5 to 18	1.1	20	- - - -
1.5	1.6×10^6	0	Wing-body combinations	5 and 18	.1	21	- - - -
					1.1	22	- - - -
					2.1	23	- - - -



CONFIDENTIAL

CONFIDENTIAL

NACA RM A53D10

*Table II.- Sketches of vapor-screen results. $M=2.0$, $x/c_r=2.1$
(a) Wings and body.*





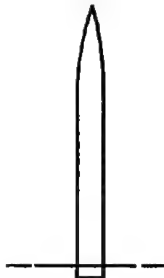




















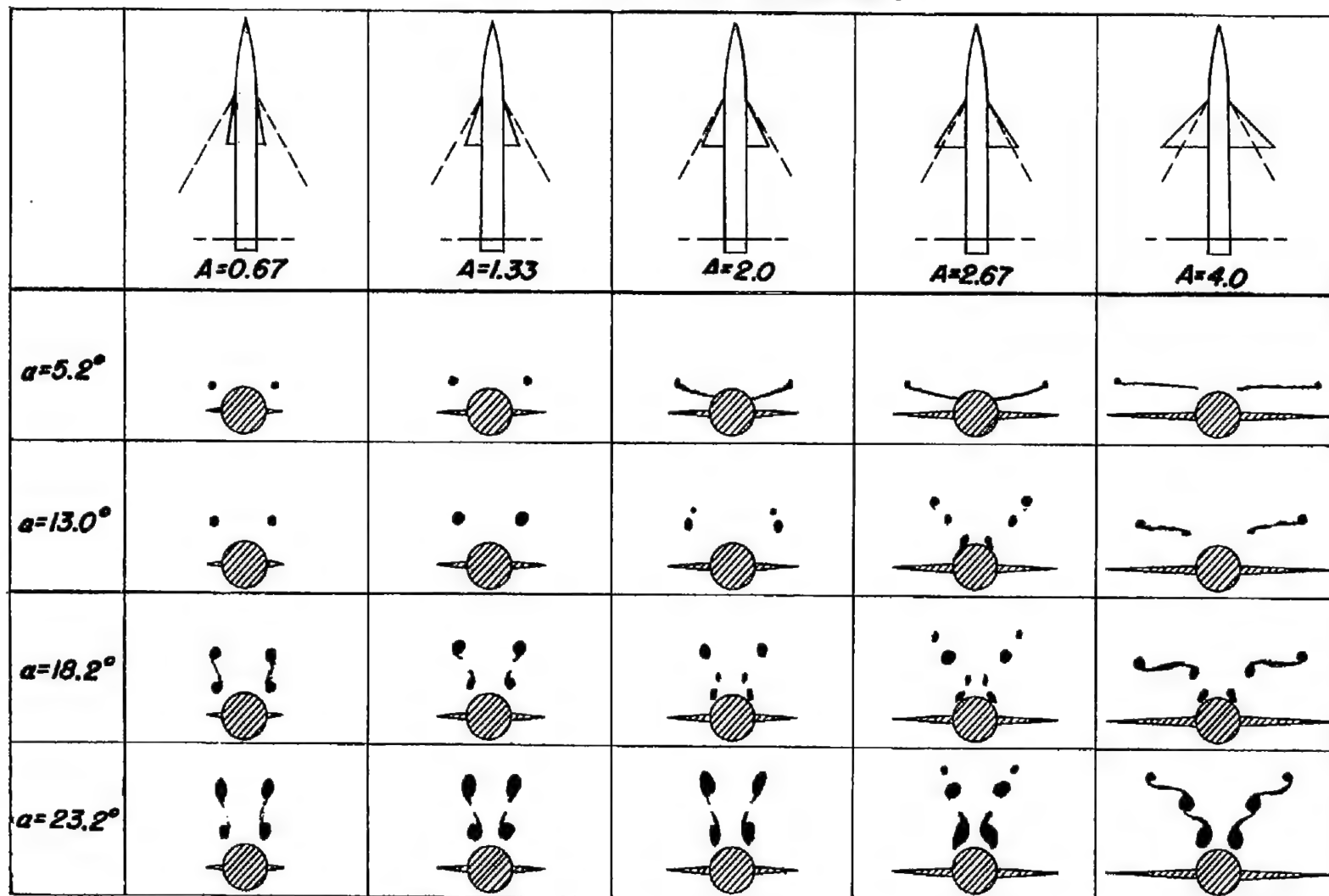
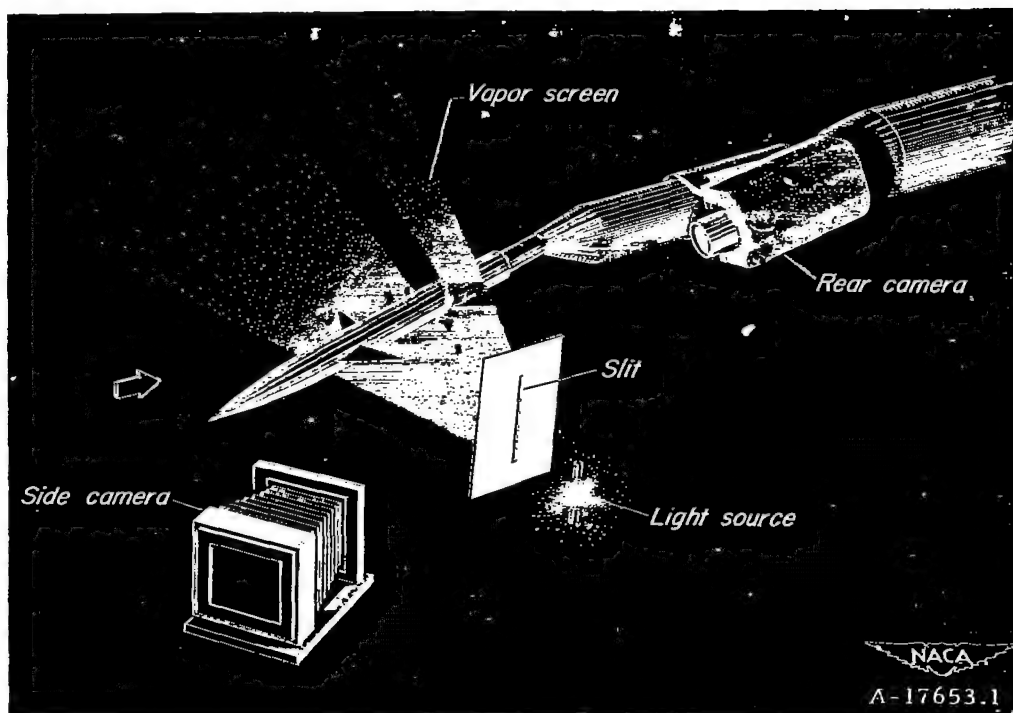
	 $A = 0.67$	 $A = 1.33$	 $A = 2.0$	 $A = 4.0$	
$\alpha = 5.5^\circ$					
$\alpha = 12.8^\circ$					
$\alpha = 18.0^\circ$					
$\alpha = 23.2^\circ$					

Table II.— Concluded .
(b) Wing-body combinations .





(a) Schematic diagram of the apparatus.

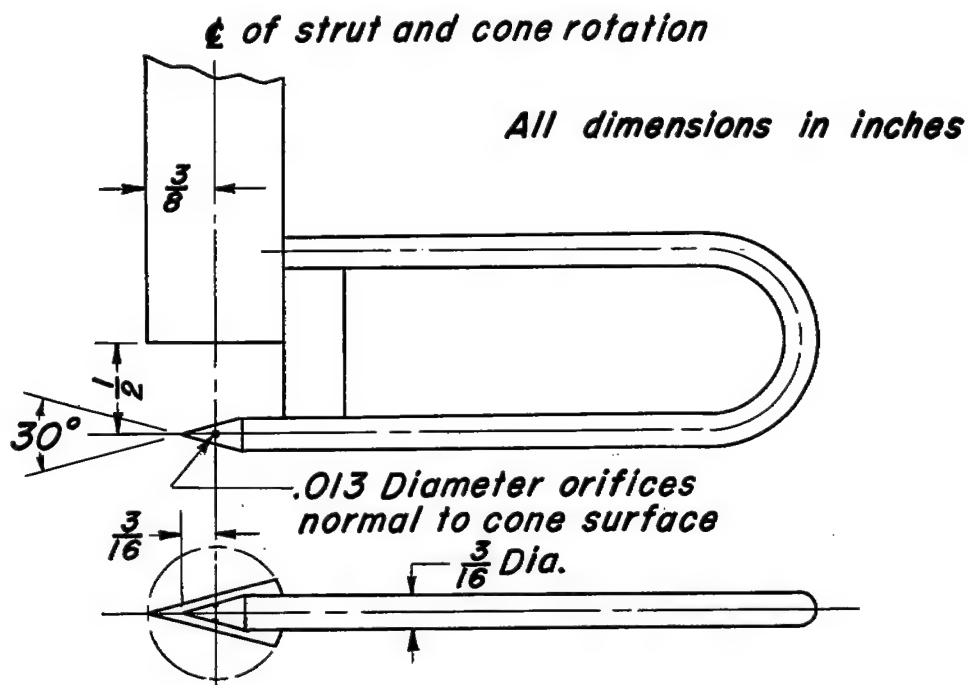


(b) View of wing model from side-camera position. Vapor screen off.

Figure 1.- Vapor-screen flow-visualization apparatus.



(a) Model and survey apparatus installed in wind tunnel.



(b) Survey cone dimensions

Figure 2.- Downwash survey apparatus.

Wing	$b/2$	c_0	A
W_1	1.25	7.43	0.67
W_2	1.75	5.23	1.33
W_3	2.25	4.45	2.00
W_4	2.75	4.10	2.67
W_5	3.75	3.75	4.00

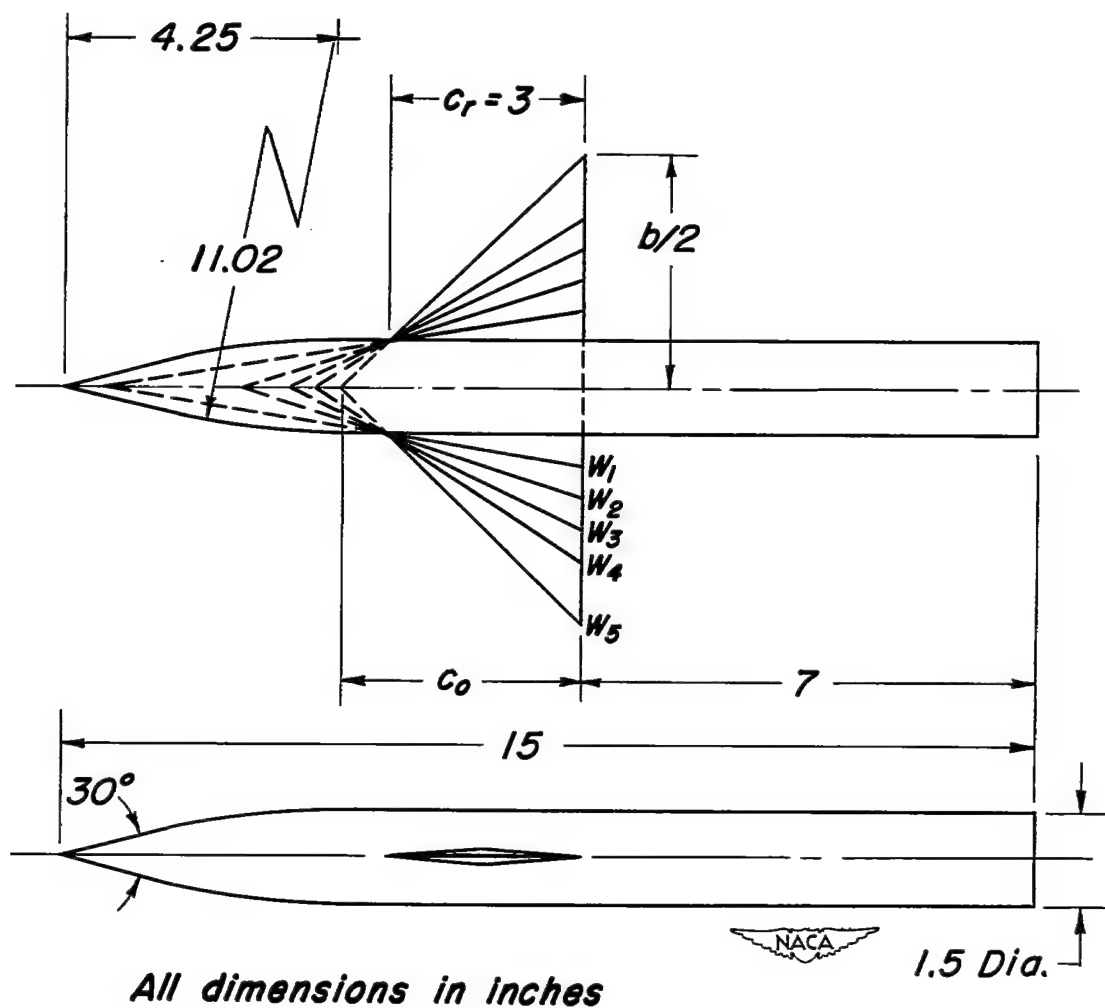


Figure 3.—Dimensions of body, wings, and wing-body combinations.

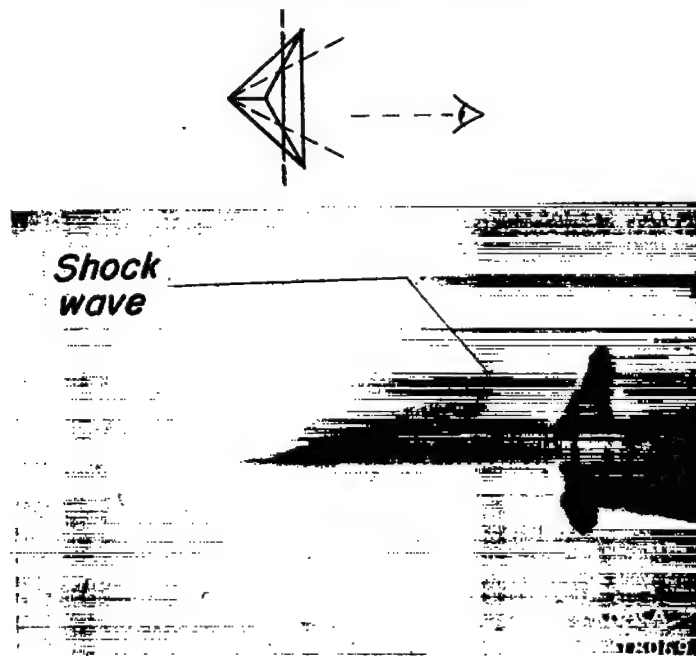
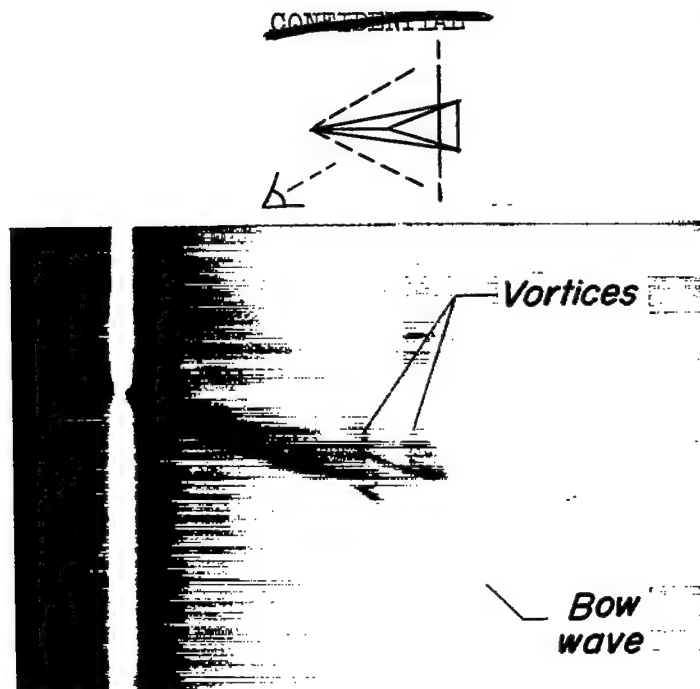


Figure 4.- Vapor-screen photographs of the flow over wing surfaces
at $x/c_r = -0.3$. $M = 2.0$; $R = 1.6 \times 10^6$.

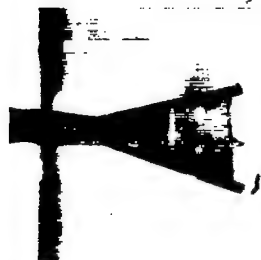
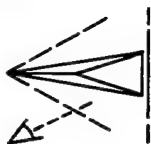
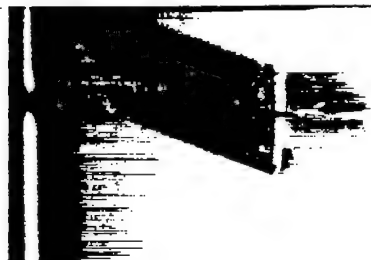
 $\alpha = 5.5^\circ$  $\alpha = 12.8^\circ$  $\alpha = 18.0^\circ$  $\alpha = 23.2^\circ$ (a) $A = 0.67$ (b) $A = 1.33$

Figure 5.- Vapor-screen photographs of the flow over wing surfaces
at $x/c_r = 0.1$. $M = 2.0$; $R = 1.6 \times 10^6$.

~~CONFIDENTIAL~~

NACA RM A53D10

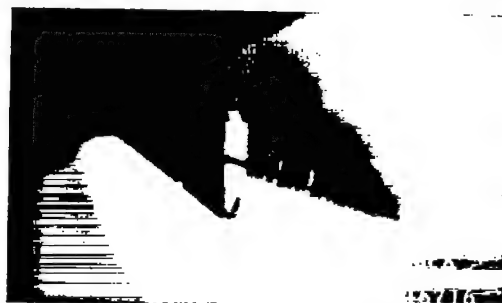
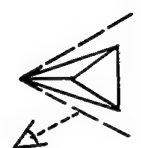
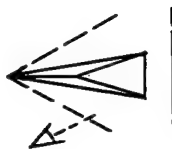
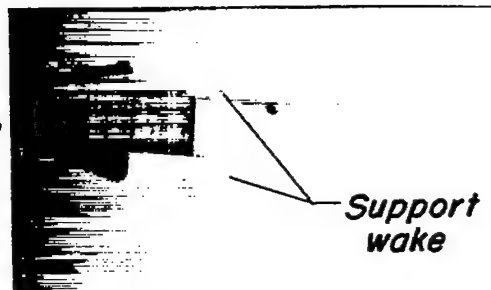
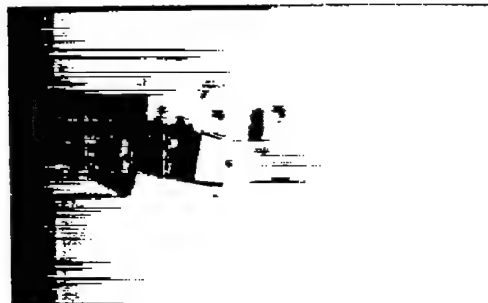
 $\alpha = 5.7^\circ$  $\alpha = 13.0^\circ$  $\alpha = 18.2^\circ$  $\alpha = 23.5^\circ$ (c) $A = 2.0$ (d) $A = 4.0$

Figure 5.- Concluded.

~~CONFIDENTIAL~~


 $\alpha = 5.5^\circ$

 $\alpha = 12.8^\circ$

 $\alpha = 18.0^\circ$

 $\alpha = 23.2^\circ$
(a) $A = 0.67$ (b) $A = 1.33$

Figure 6.- Vapor-screen photographs of the flow over wing surfaces
at $x/c_r = 0.5$. $M = 2.0$; $R = 1.6 \times 10^6$.

~~CONFIDENTIAL~~

NACA RM A53D10

 $\alpha = 5.7^\circ$  $\alpha = 13.0^\circ$  $\alpha = 18.2^\circ$  $\alpha = 23.5^\circ$ (c) $A = 2.0$ (d) $A = 4.0$

Figure 6.- Concluded.

~~CONFIDENTIAL~~

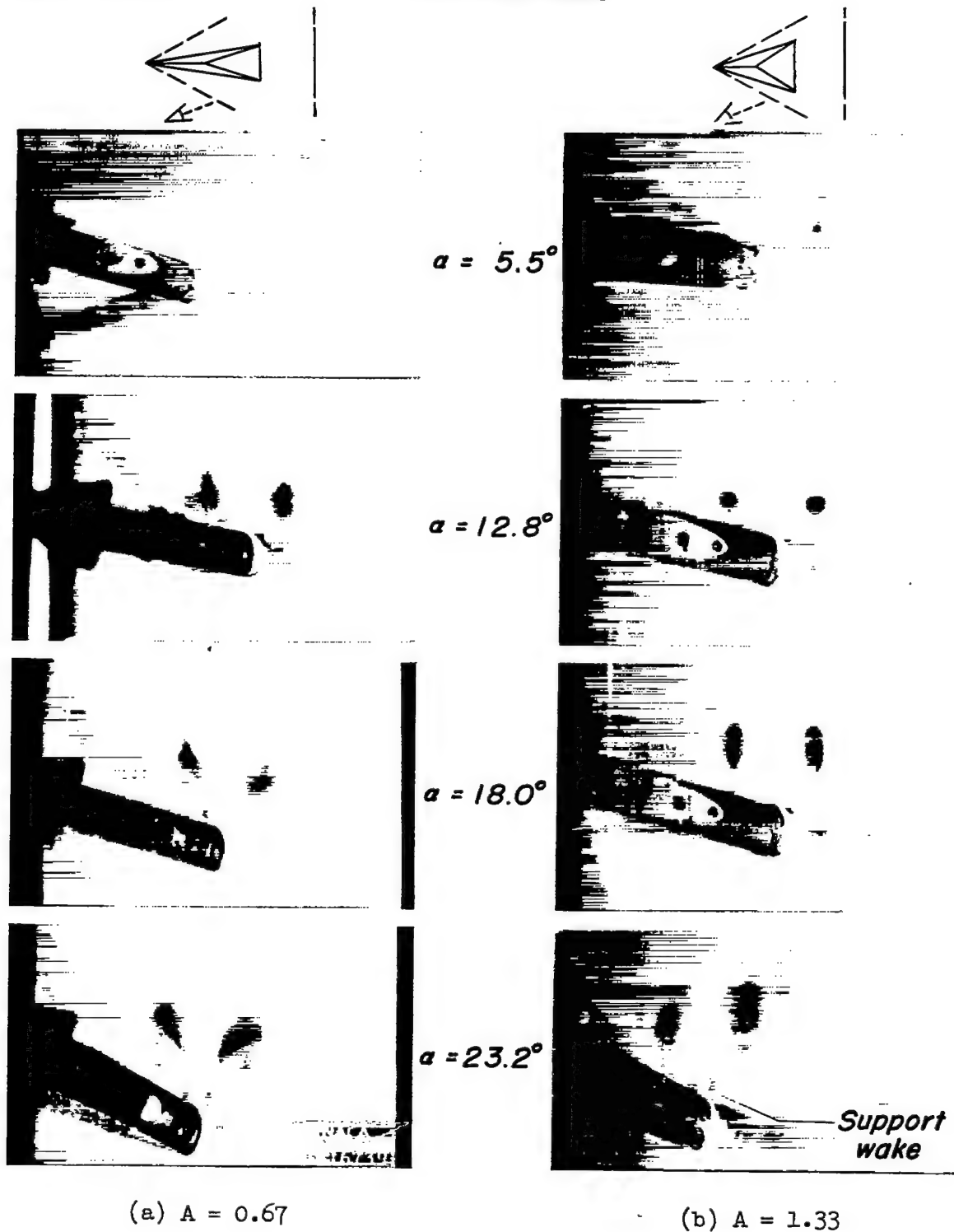


Figure 7.- Vapor-screen photographs of the flow over wing surfaces
at $x/c_r = 1.1$. $M = 2.0$; $R = 1.6 \times 10^6$.

~~CONFIDENTIAL~~

NACA RM A53D10

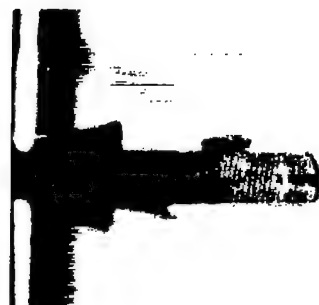
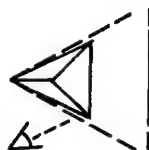
 $\alpha = 5.7^\circ$  $\alpha = 13.0^\circ$  $\alpha = 18.2^\circ$  $\alpha = 23.5^\circ$ (c) $A = 2.0$ (d) $A = 4.0$

Figure 7.- Concluded.

~~CONFIDENTIAL~~

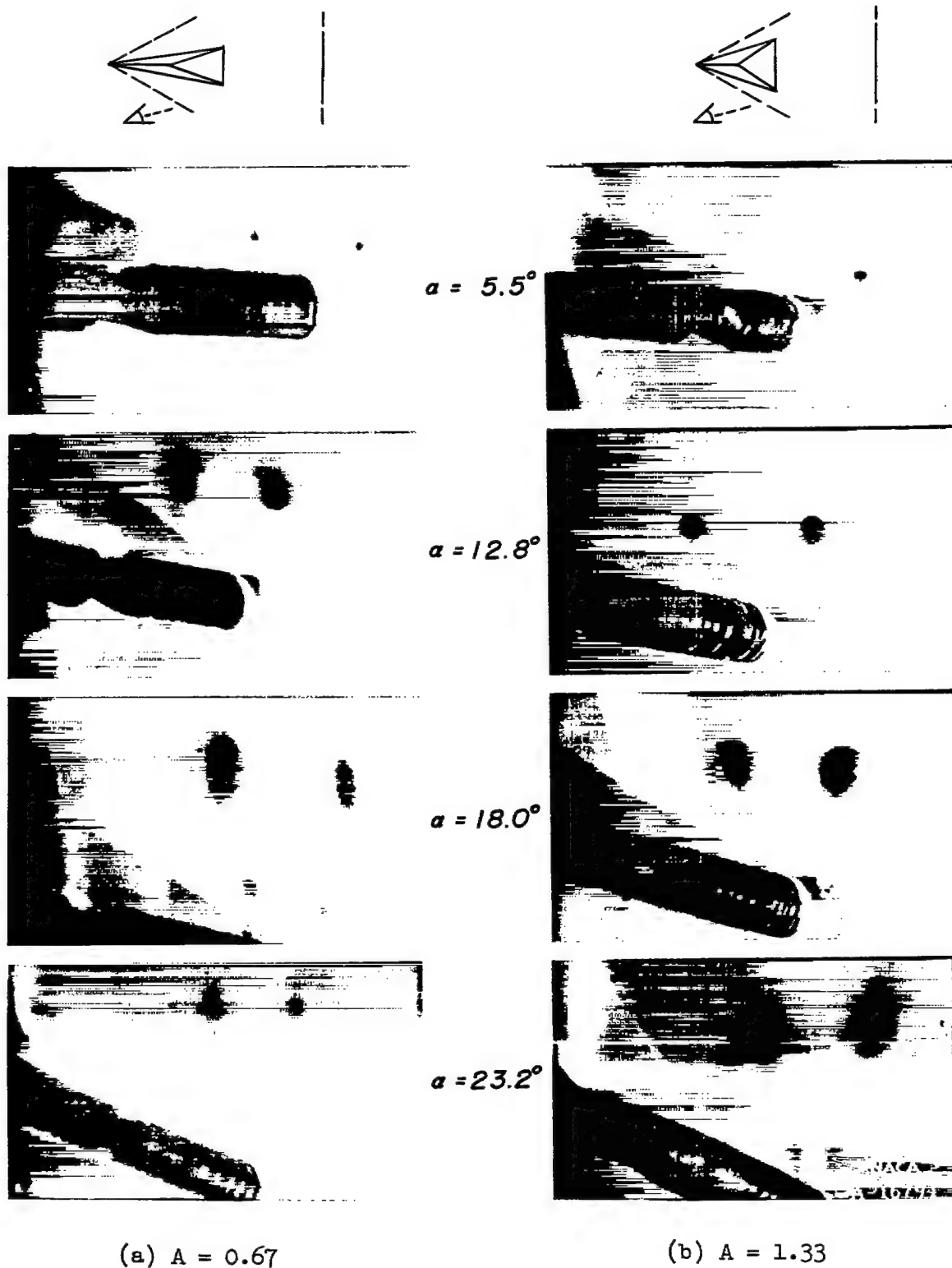


Figure 8.- Vapor-screen photographs of the flow over wing surfaces
at $x/c_r = 2.1$. $M = 2.0$; $R = 1.6 \times 10^6$.

~~CONFIDENTIAL~~

NACA RM A53D10

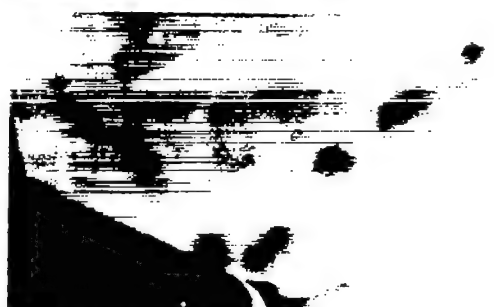
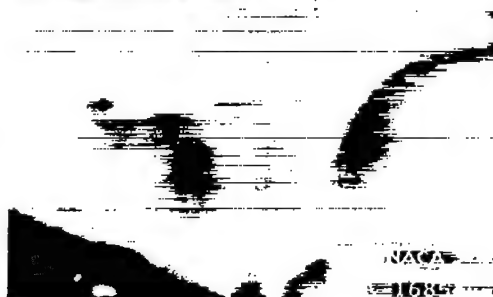
 $\alpha = 5.7^\circ$  $\alpha = 13.0^\circ$  $\alpha = 18.2^\circ$  $\alpha = 23.5^\circ$ (c) $A = 2.0$ (d) $A = 4.0$

Figure 8.- Concluded.

~~CONFIDENTIAL~~

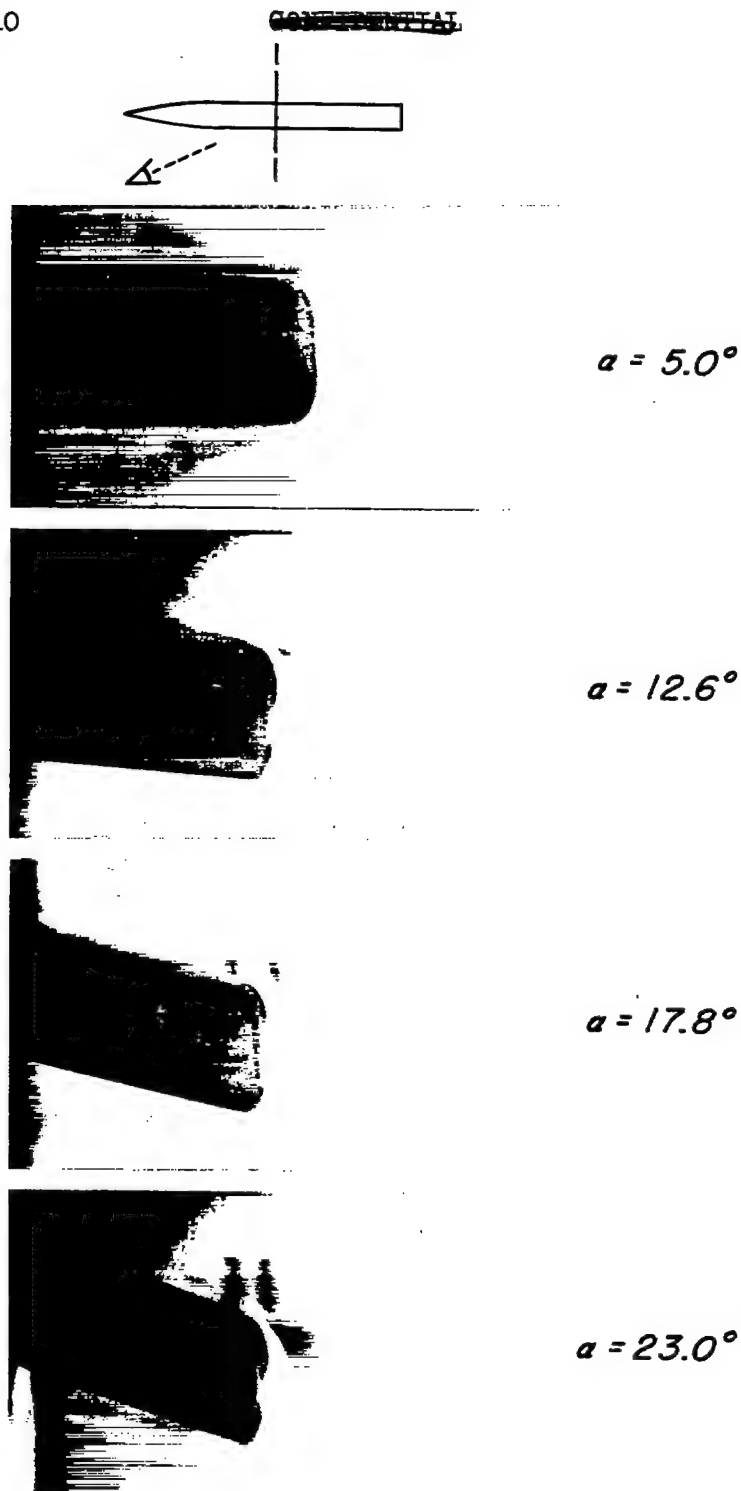


Figure 9.- Vapor-screen photographs of the flow over the body
at $x/c_r = 0.1$. $M = 2.0$; $R = 1.6 \times 10^6$.

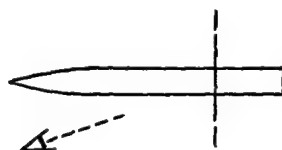
 $\alpha = 5.0^\circ$  $\alpha = 12.6^\circ$  $\alpha = 17.8^\circ$  $\alpha = 23.0^\circ$

Figure 10.- Vapor-screen photographs of the flow over the body at $x/c_r = 1.1$. $M = 2.0$; $R = 1.6 \times 10^6$.

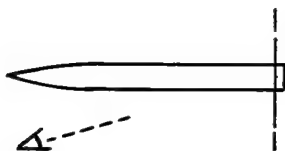
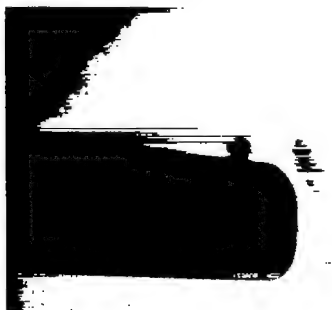
 $\alpha = 5.0^\circ$  $\alpha = 12.6^\circ$  $\alpha = 17.8^\circ$  $\alpha = 23.0^\circ$

Figure 11.- Vapor-screen photographs of the flow over the body
at $x/c_r = 2.1$. $M = 2.0$; $R = 1.6 \times 10^6$.

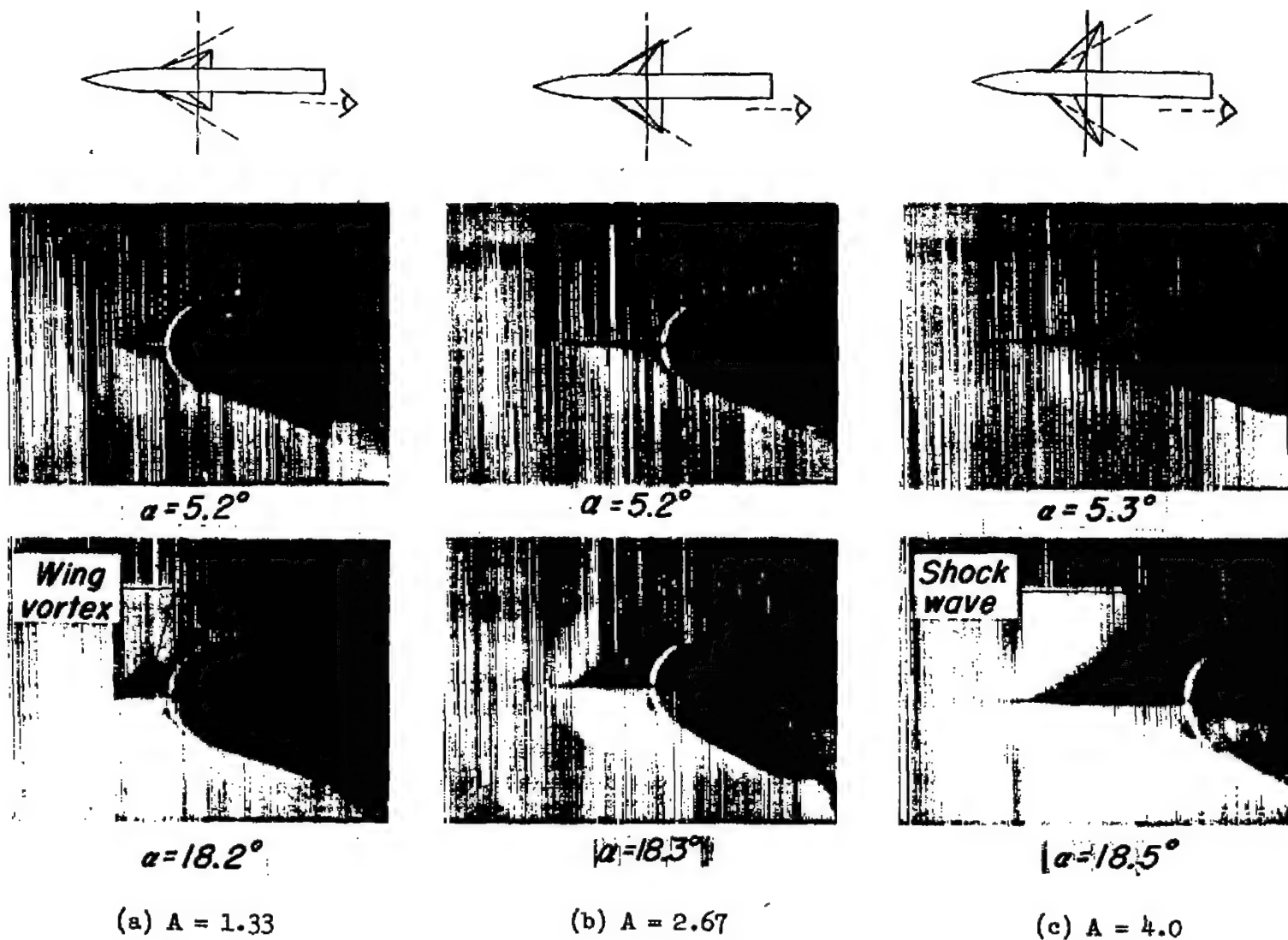


Figure 12.- Vapor-screen photographs of the flow over wing-body combinations
at $x/c_r = -0.3$. $M = 2.0$; $R = 1.6 \times 10^6$.

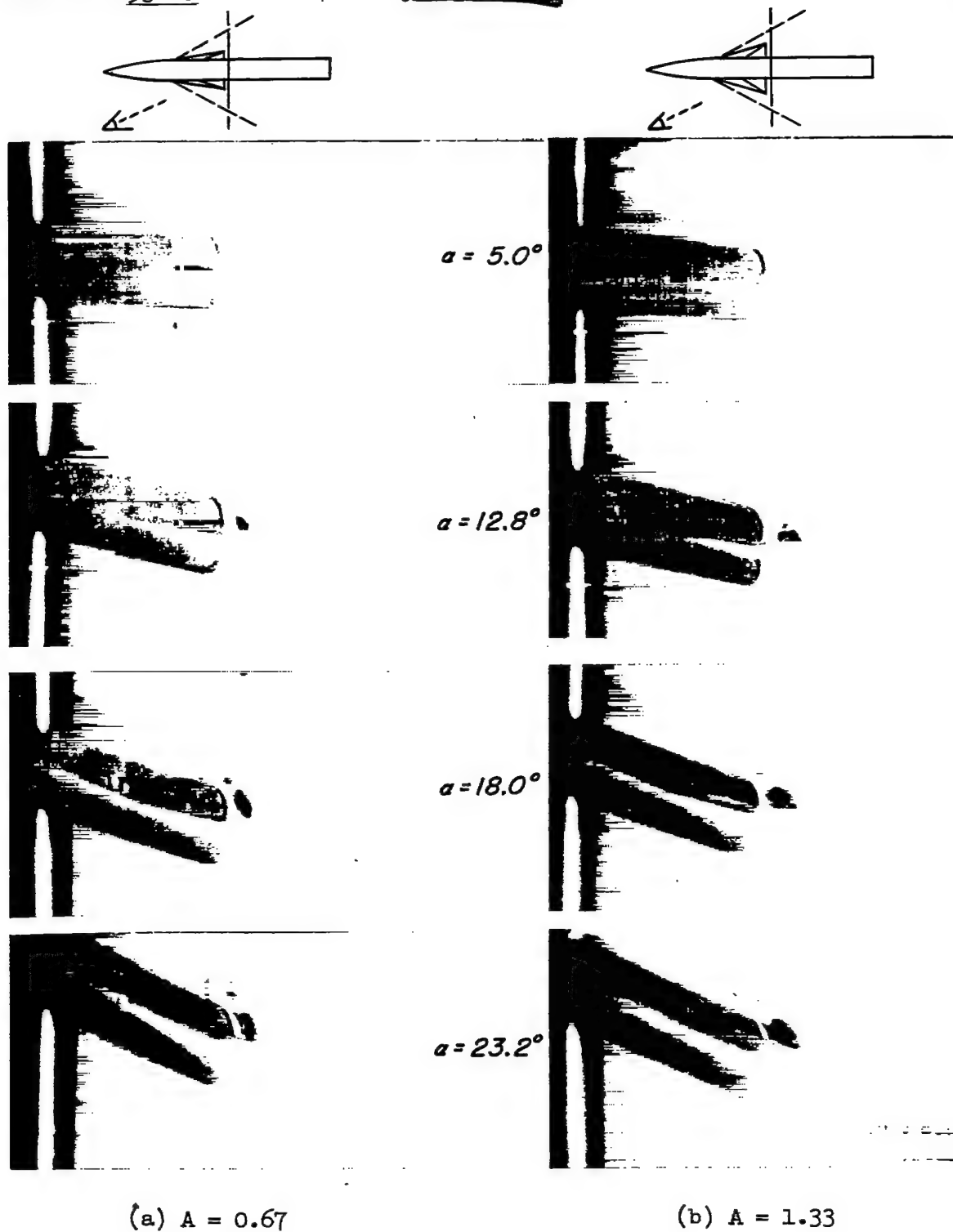


Figure 13.- Vapor-screen photographs of the flow over wing-body combinations at $x/c_r = 0.1$. $M = 2.0$; $R = 1.6 \times 10^6$.

~~CONFIDENTIAL~~

NACA RM A53D10

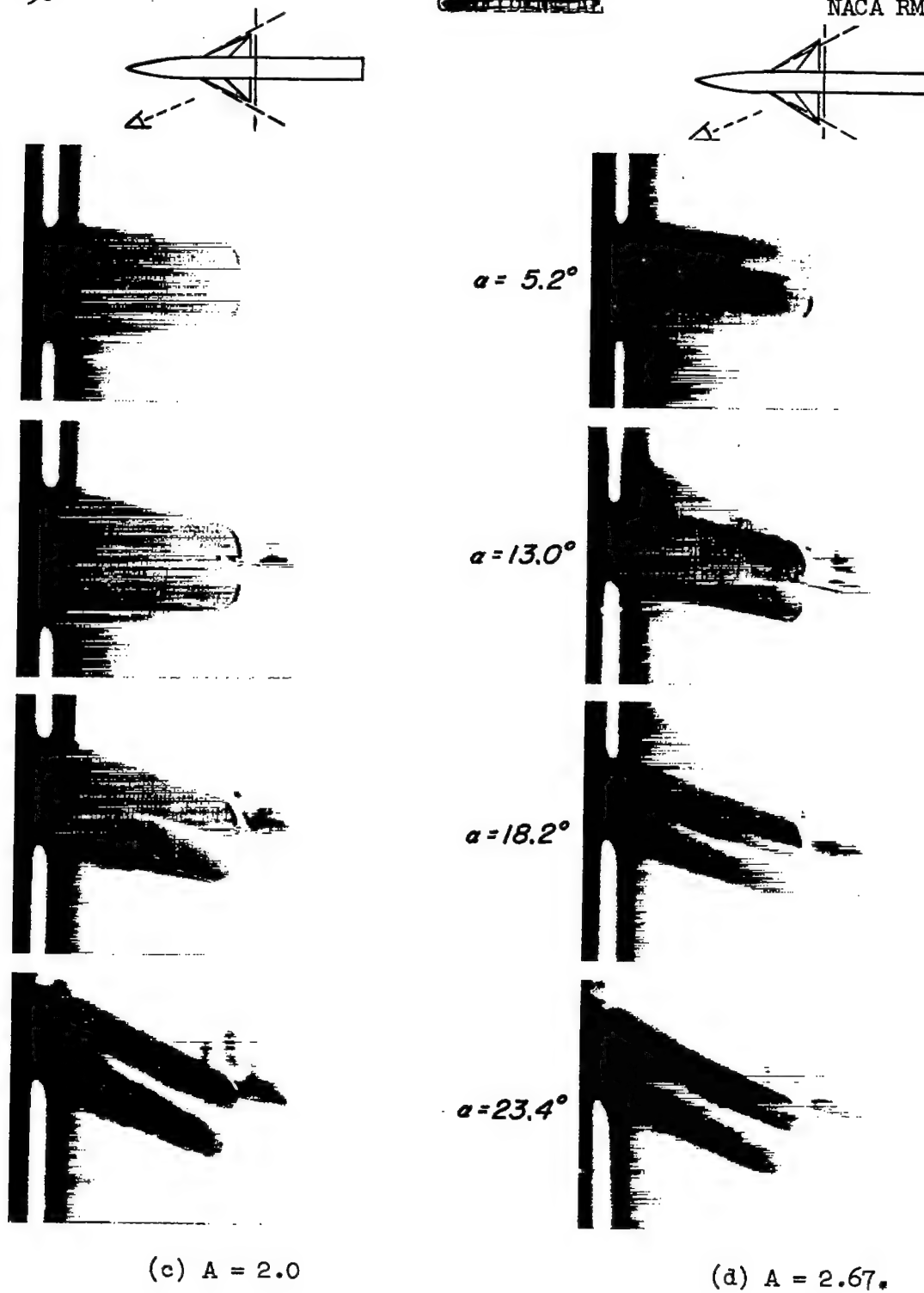


Figure 13.- Continued.

~~CONFIDENTIAL~~

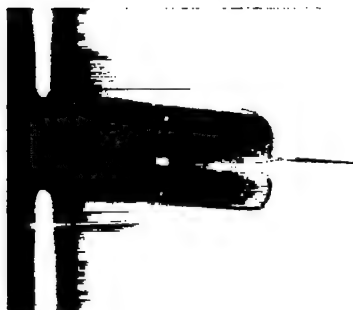
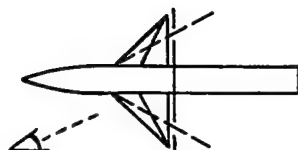
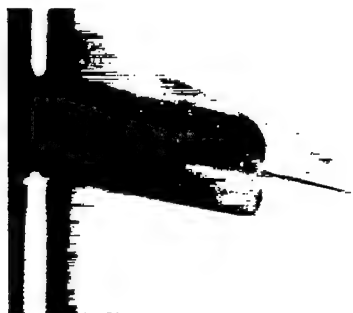
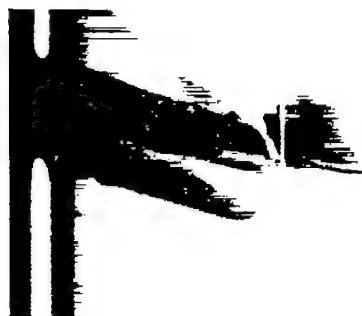
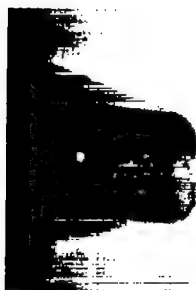
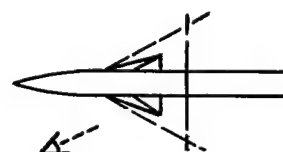
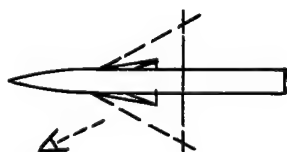
 $\alpha = 5.3^\circ$  $\alpha = 13.2^\circ$  $\alpha = 18.5^\circ$  $\alpha = 23.7^\circ$ (e) $A = 4.0$

Figure 13.- Concluded.


 $\alpha = 5.0^\circ$

 $\alpha = 12.8^\circ$

 $\alpha = 18.0^\circ$

 $\alpha = 23.2^\circ$


(a) $A = 0.67$

(b) $A = 1.33$

Figure 14.- Vapor-screen photographs of the flow over wing-body combinations at $x/c_r = 0.5$. $M = 2.0$; $R = 1.6 \times 10^6$.

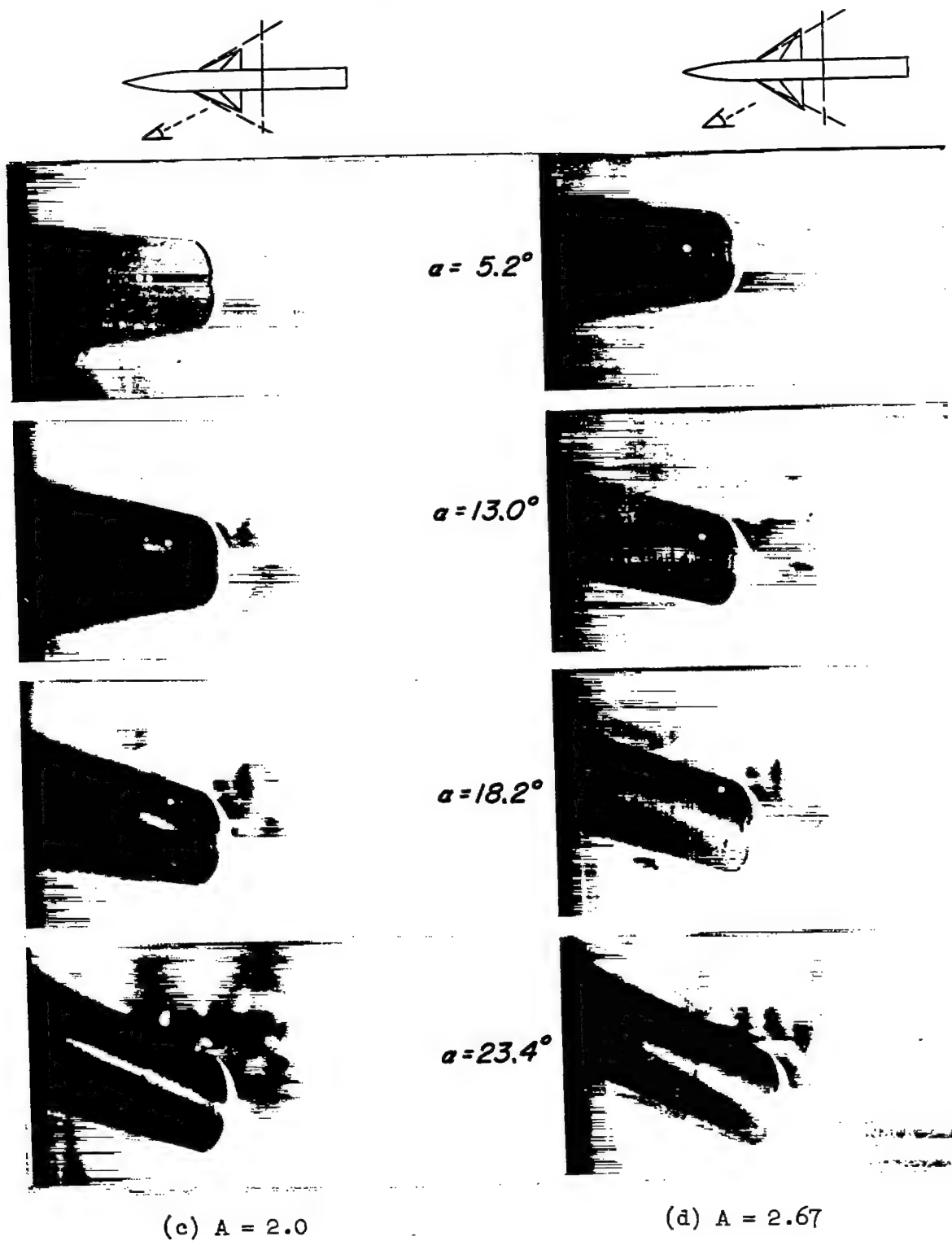


Figure 14.- Continued.

~~CONFIDENTIAL~~

NACA RM A53D10

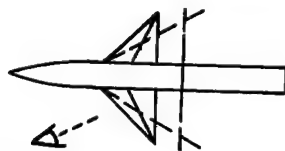
 $\alpha = 5.3^\circ$  $\alpha = 13.2^\circ$  $\alpha = 18.5^\circ$  $\alpha = 23.7^\circ$ (e) $A = 4.0$

Figure 14.- Concluded.

~~CONFIDENTIAL~~

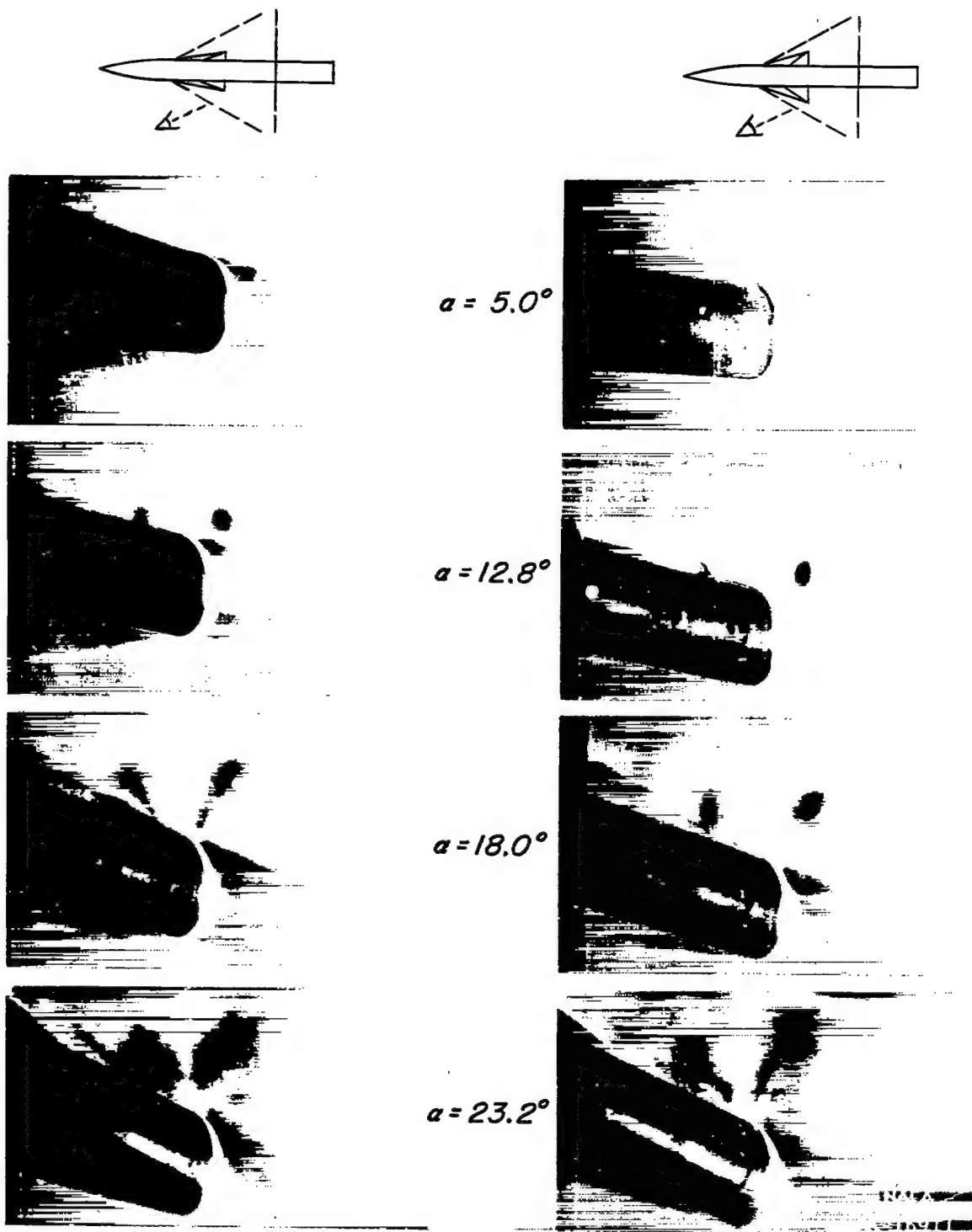


Figure 15.- Vapor-screen photographs of the flow over wing-body combinations at $x/c_r = 1.1$. $M = 2.0$; $R = 1.6 \times 10^6$.

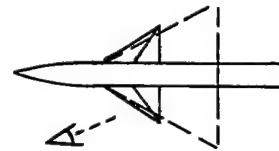
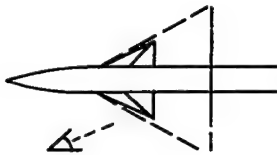
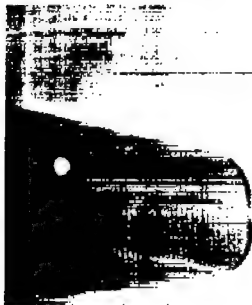
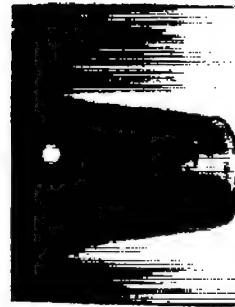
 $\alpha = 5.2^\circ$  $\alpha = 13.0^\circ$  $\alpha = 18.2^\circ$  $\alpha = 23.4^\circ$ (c) $A = 2.0$ (d) $A = 2.67$

Figure 15.- Continued.

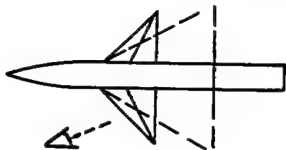
~~CONFIDENTIAL~~ $\alpha = 5.3^\circ$  $\alpha = 13.2^\circ$  $\alpha = 18.5^\circ$  $\alpha = 23.7^\circ$ (e) $A = 4.0$

Figure 15.- Concluded.

~~CONFIDENTIAL~~

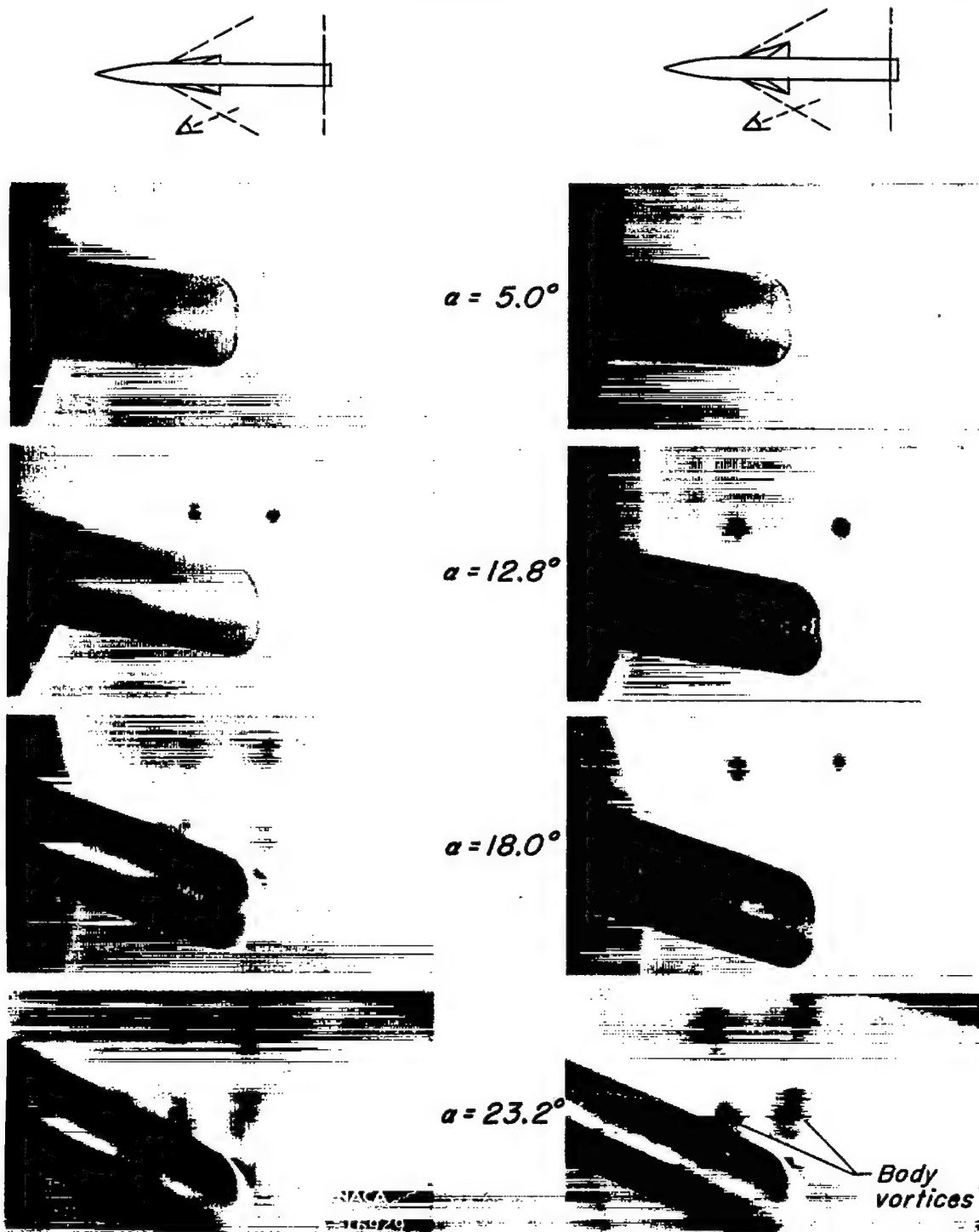
(a) $A = 0.67$ (b) $A = 1.33$

Figure 16.- Vapor-screen photographs of the flow over wing-body combinations at $x/c_r = 2.1$. $M = 2.0$; $R = 1.6 \times 10^6$.

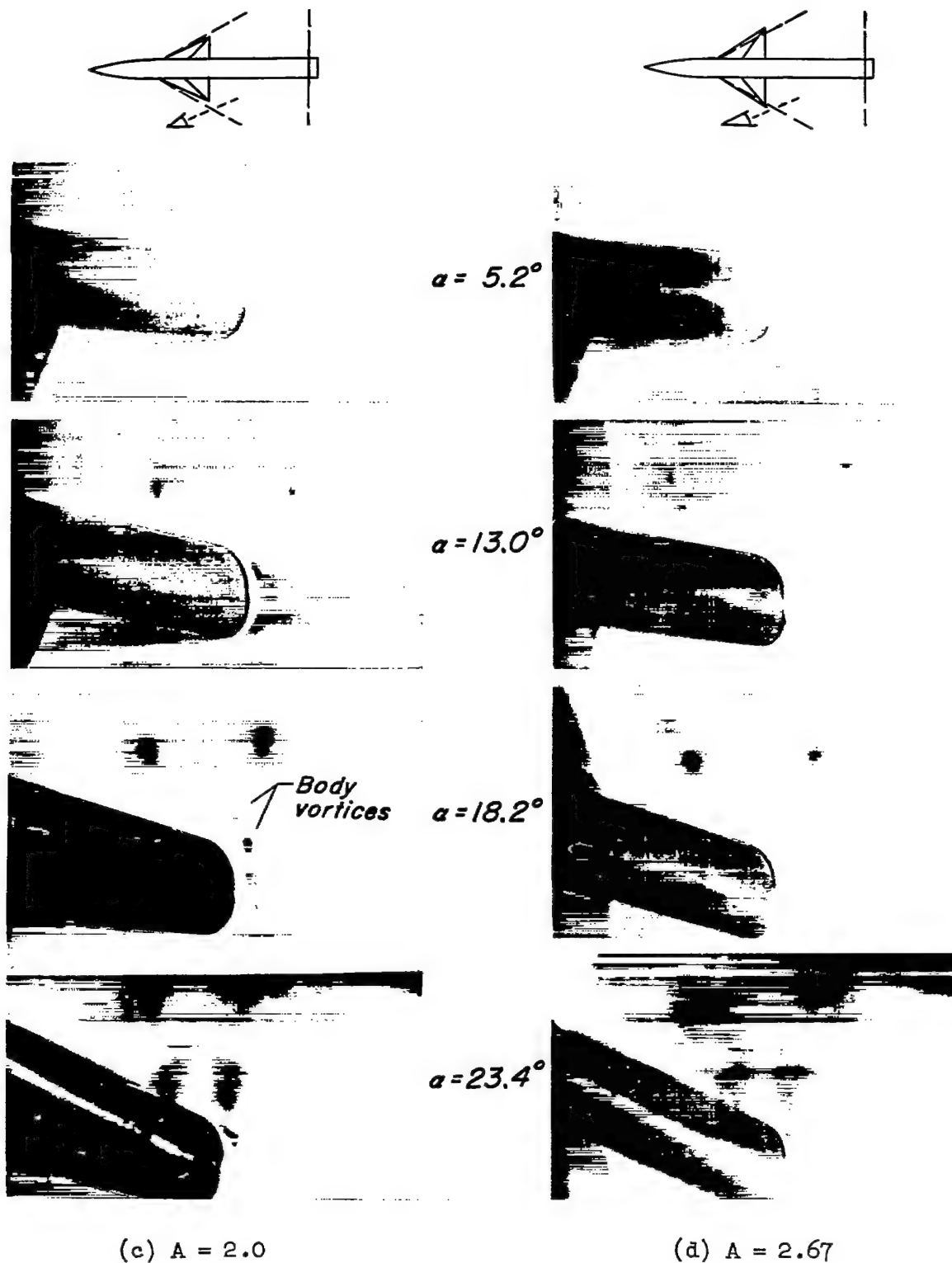


Figure 16.- Continued.

~~CONFIDENTIAL~~

NACA RM A53D10

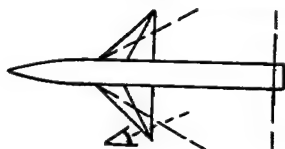
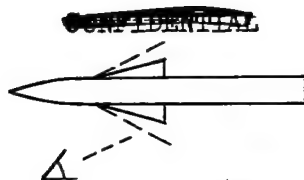
 $\alpha = 5.3^\circ$  $\alpha = 13.2^\circ$  $\alpha = 18.5^\circ$  $\alpha = 23.7^\circ$ (e) $A = 4.0$

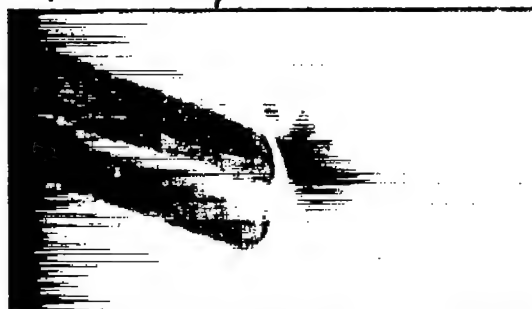
Figure 16.- Concluded.

~~CONFIDENTIAL~~


 $x/c_r = -0.4$

 $x/c_r = 0.9$

 $x/c_r = 0$

 $x/c_r = 1.3$

 $x/c_r = 0.2$

 $x/c_r = 1.8$

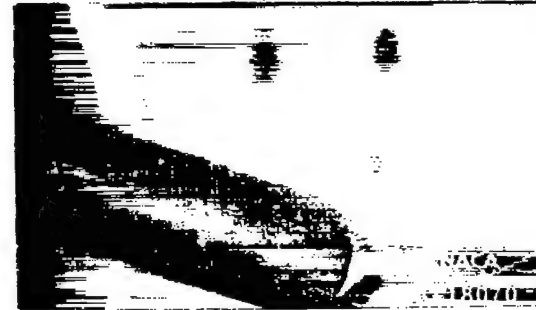
 $x/c_r = 0.5$

 $x/c_r = 2.3$

Figure 17.- Vapor-screen photographs of the wake behind $A = 1.33$ wing-body combination, $\alpha = 18.0$. $M = 2.0$; $R = 1.8 \times 10^6$.

CONFIDENTIAL

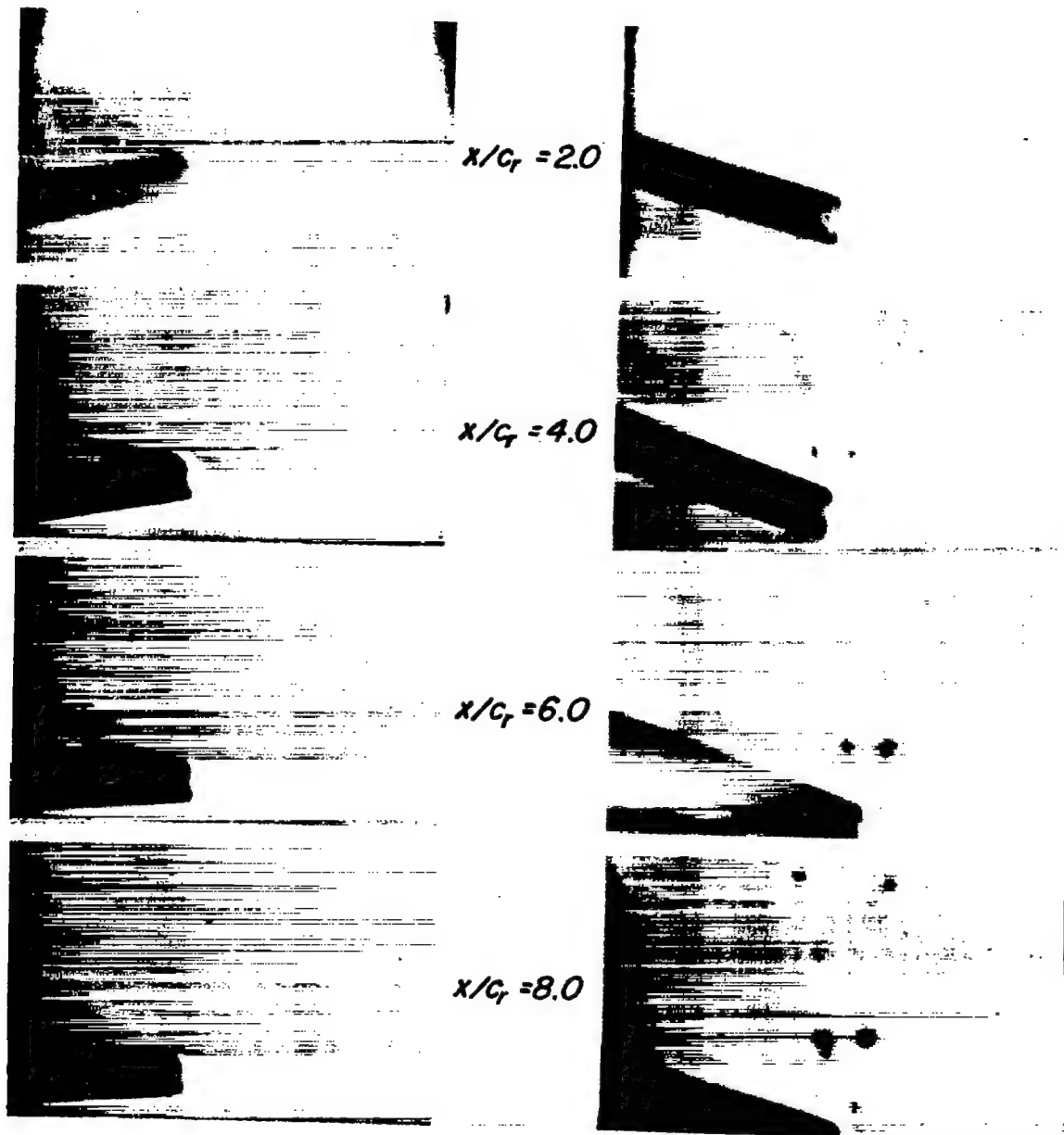
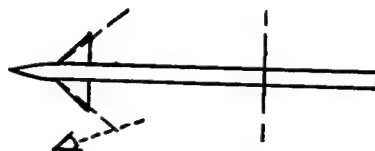
~~CONFIDENTIAL~~(a) $\alpha = 12.6^\circ$ (b) $\alpha = 17.8^\circ$

Figure 18.- Vapor-screen photographs of the wake behind $A = 4$ wing-body combination. $M = 2.0$; $R = 0.8 \times 10^6$.

~~CONFIDENTIAL~~

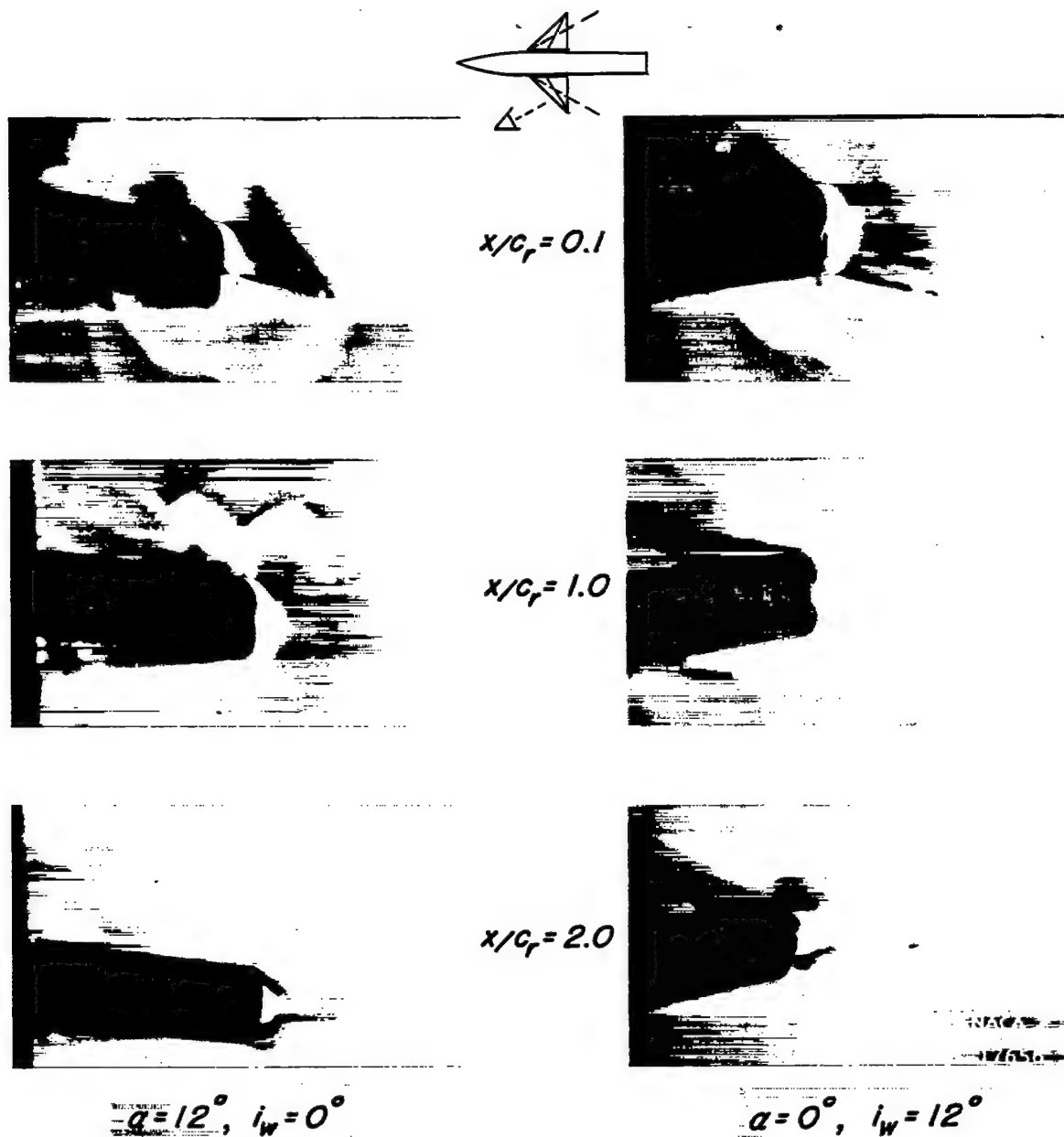


Figure 19.- Vapor-screen photographs of the flow over $A = 4.0$ wing-body combination. $M = 2.0$; $R = 1.4 \times 10^6$.

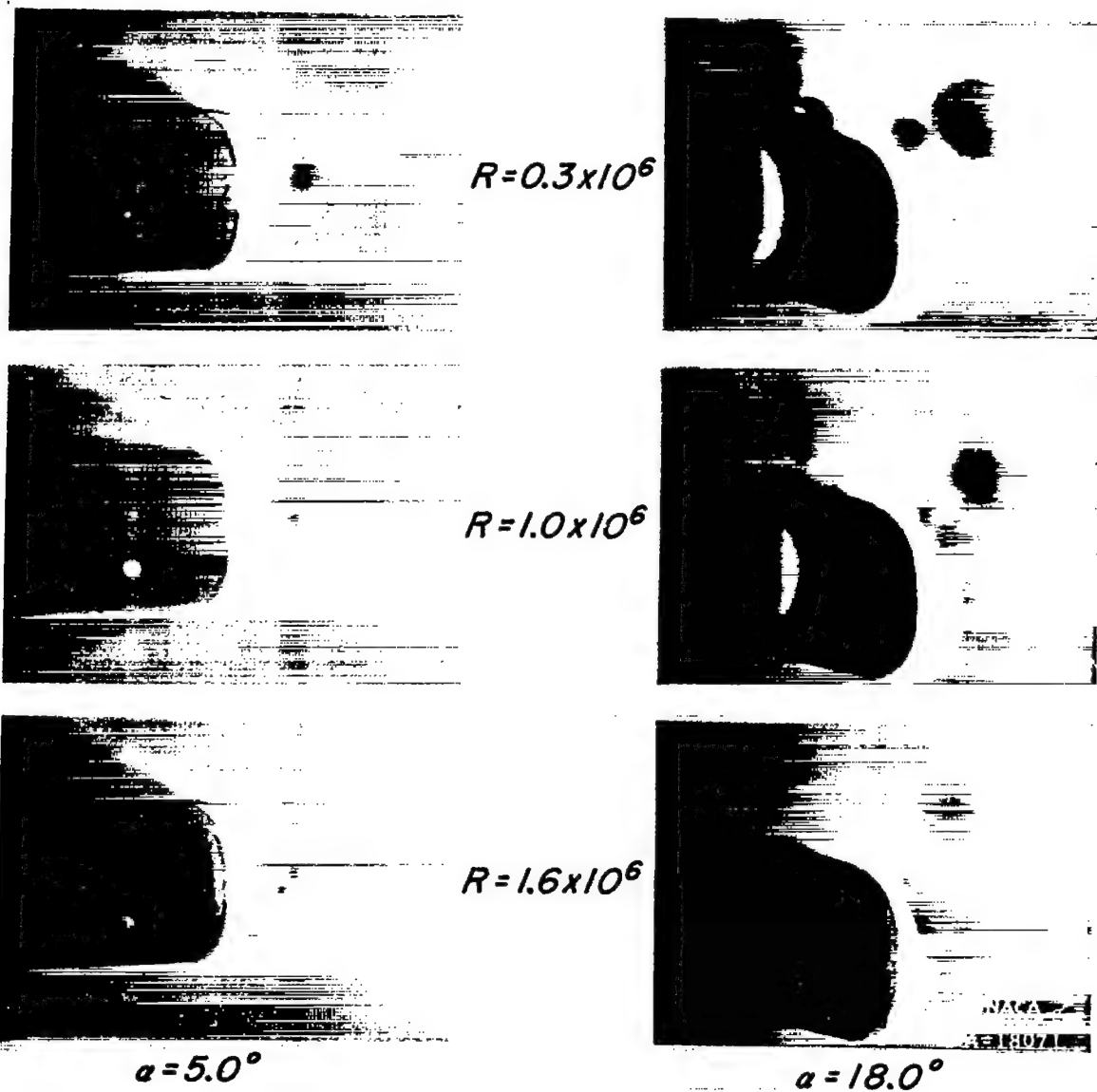
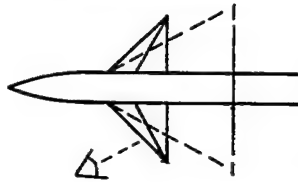
(a) $A = 1.33$

Figure 20.- Vapor-screen photographs of the flow over wing-body combinations at various Reynolds numbers. $x/c_r = 1.1$; $M = 2.0$.



$$R = 0.3 \times 10^6$$



$$R = 1.0 \times 10^6$$



$$R = 1.6 \times 10^6$$

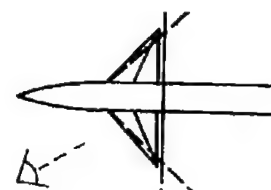
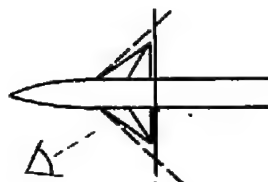
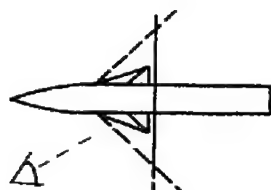
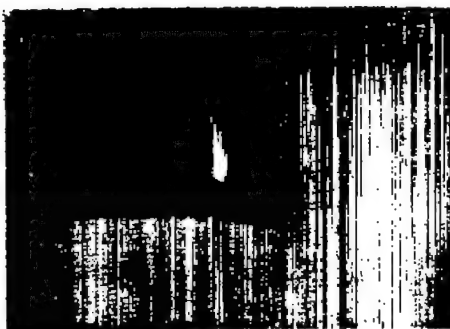


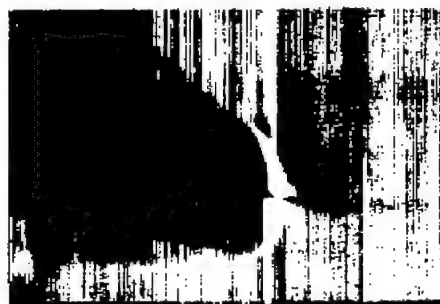
$$\alpha = 13.2^\circ$$

$$\alpha = 18.5^\circ$$

(b) $A = 4.0$

Figure 20.- Concluded.


 $\alpha = 5.2^\circ$

 $\alpha = 5.2^\circ$

 $\alpha = 5.3^\circ$

 $\alpha = 18.2^\circ$

 (a) $A = 1.33$

 $\alpha = 18.3^\circ$

 (b) $A = 2.67$

 $\alpha = 18.5^\circ$

 (c) $A = 4.0$

Figure 21.- Vapor-screen photographs of the flow over wing-body combinations at $x/c_r = 0.1$. $M = 1.5$; $R = 1.5 \times 10^6$.

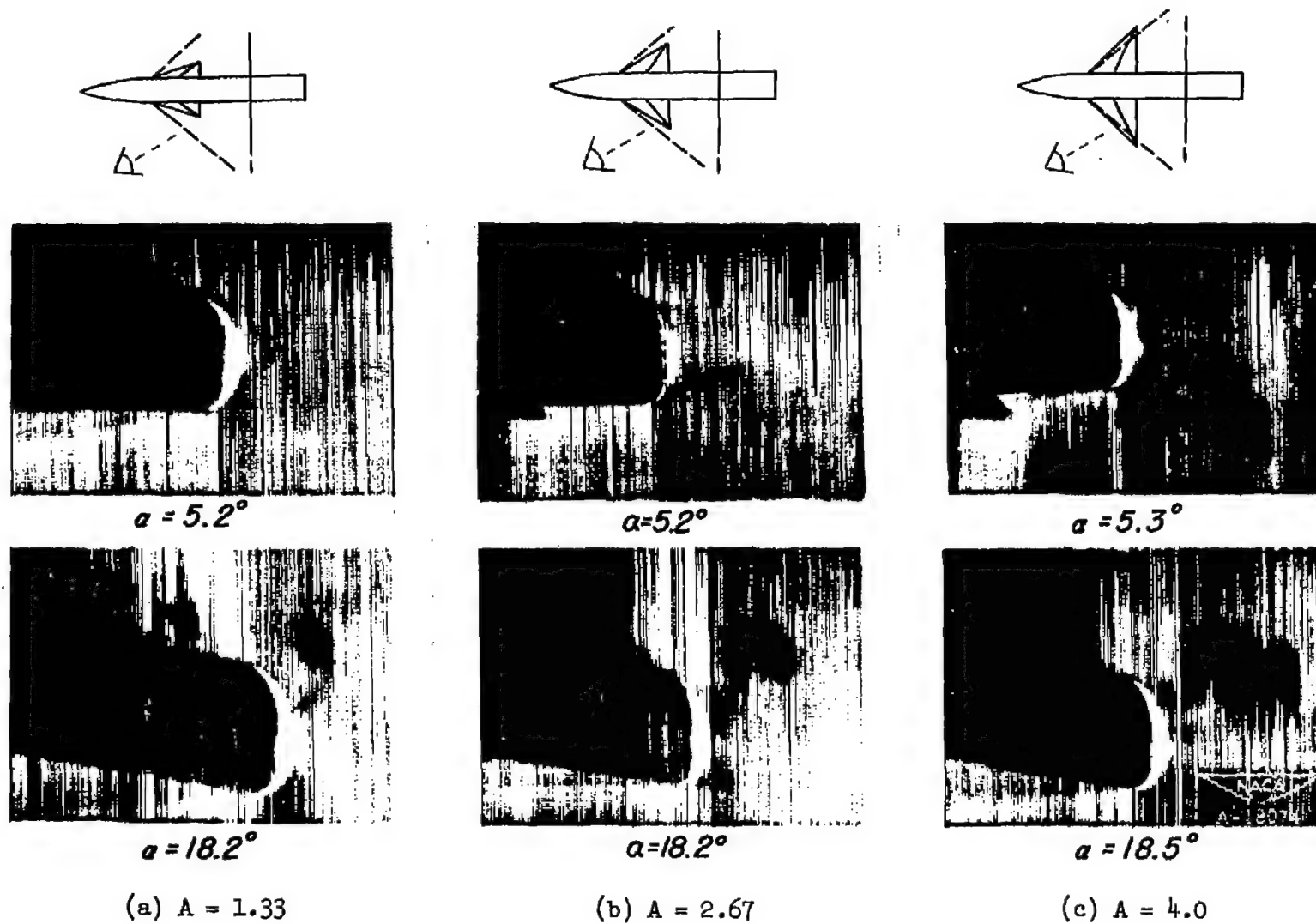


Figure 22.- Vapor-screen photographs of the flow over wing-body combinations at $x/c_r = 1.1$. $M = 1.5$; $R = 1.5 \times 10^6$.

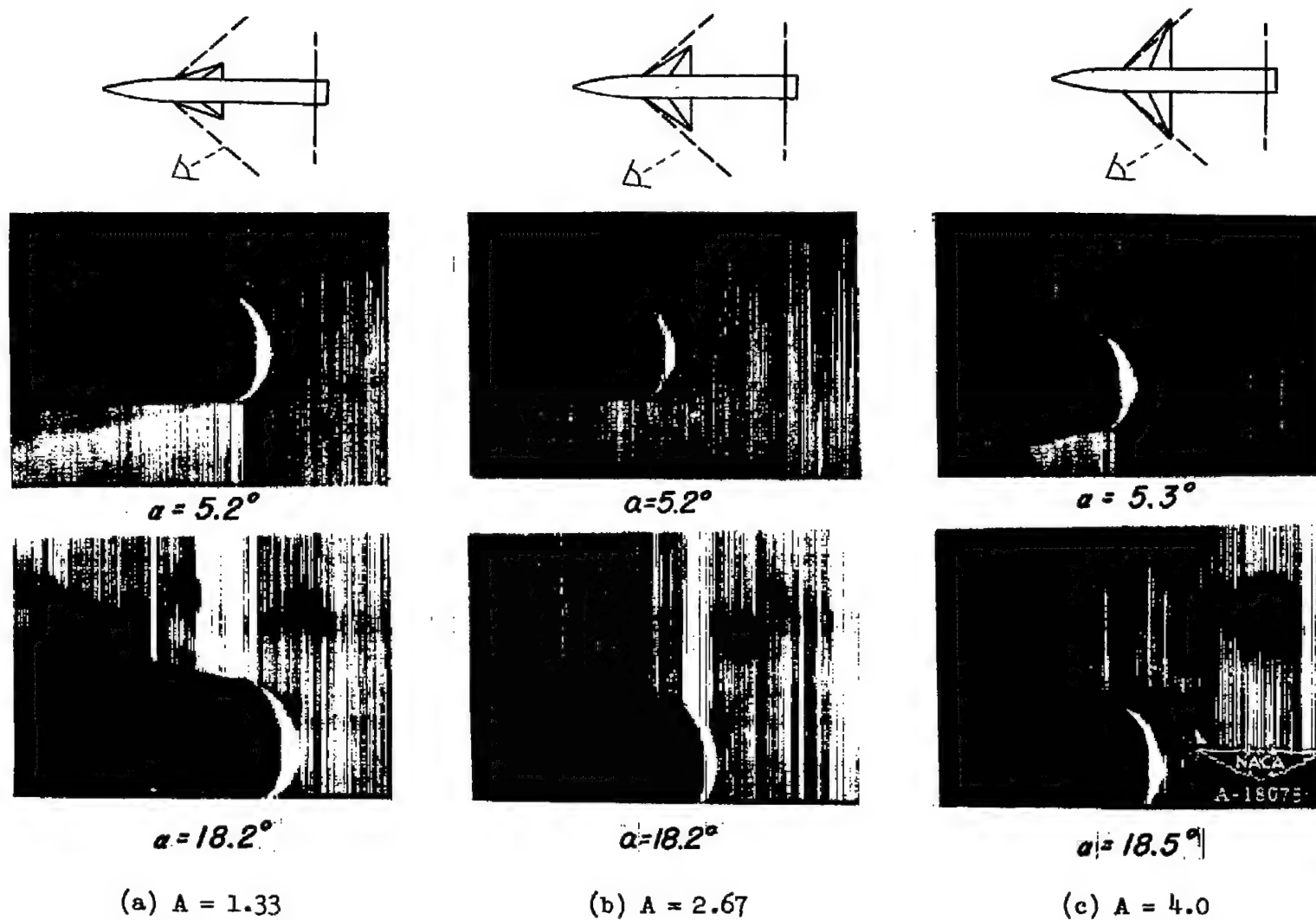


Figure 23.- Vapor-screen photographs of the flow over wing-body combinations at $x/c_r = 2.1$. $M = 1.5$; $R = 1.5 \times 10^6$.

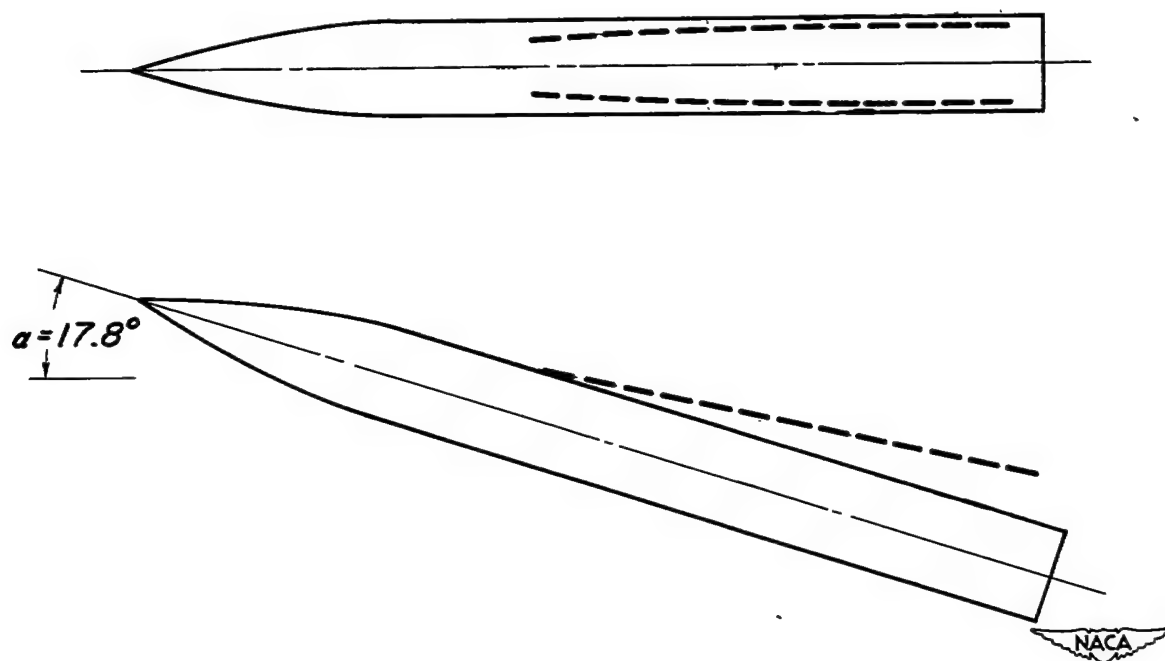


Figure 24.- Vortex paths from vapor-screen photographs of the body.
 $M = 2.0$; $R = 1.6 \times 10^6$.

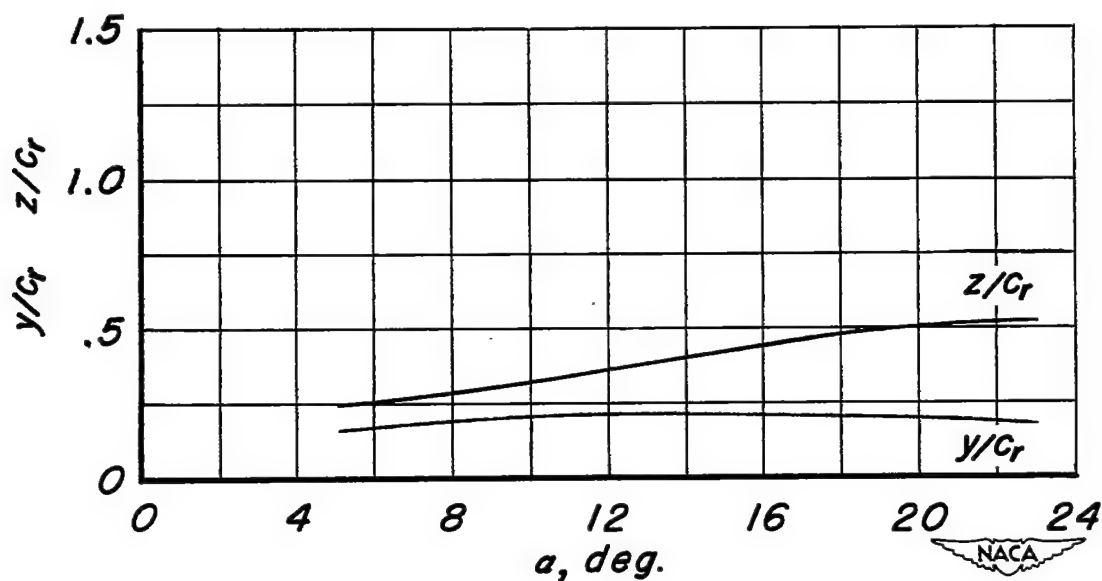
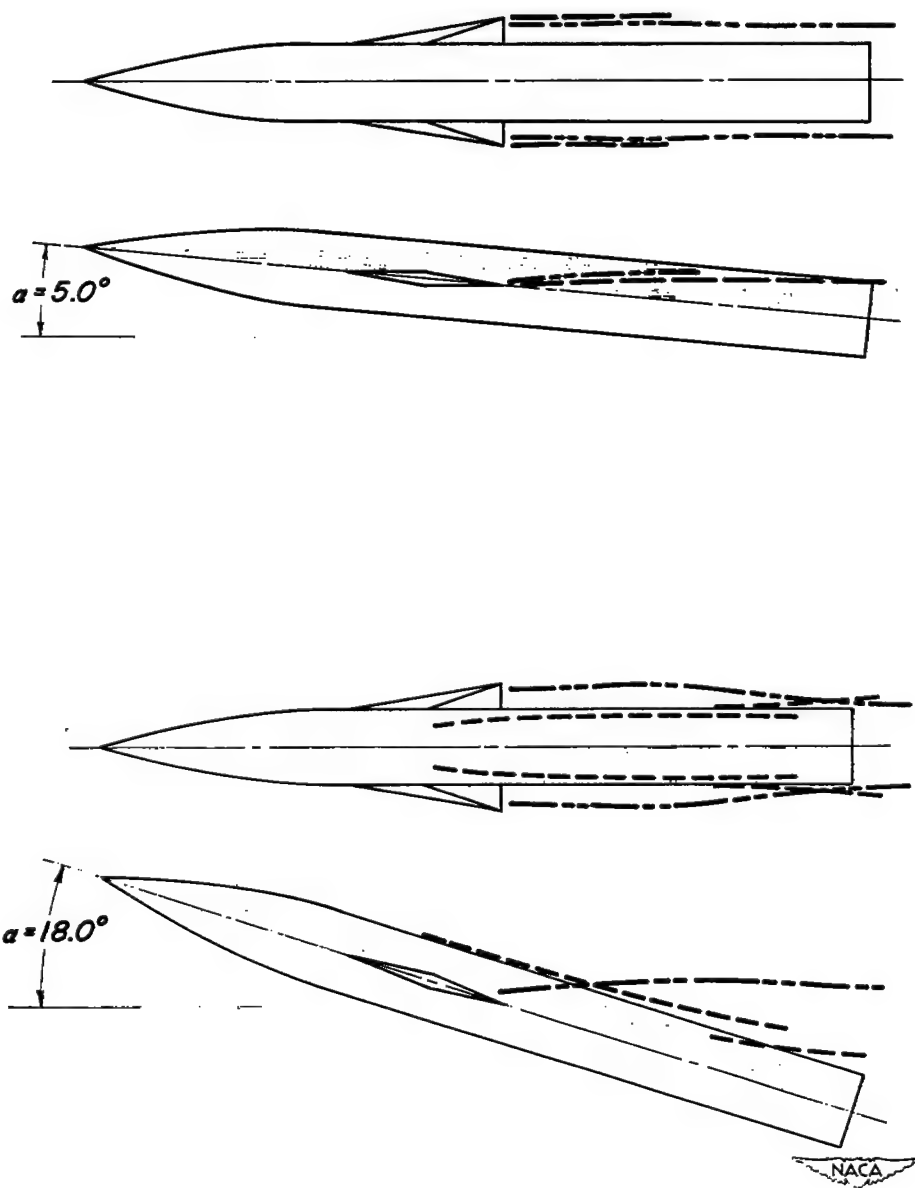
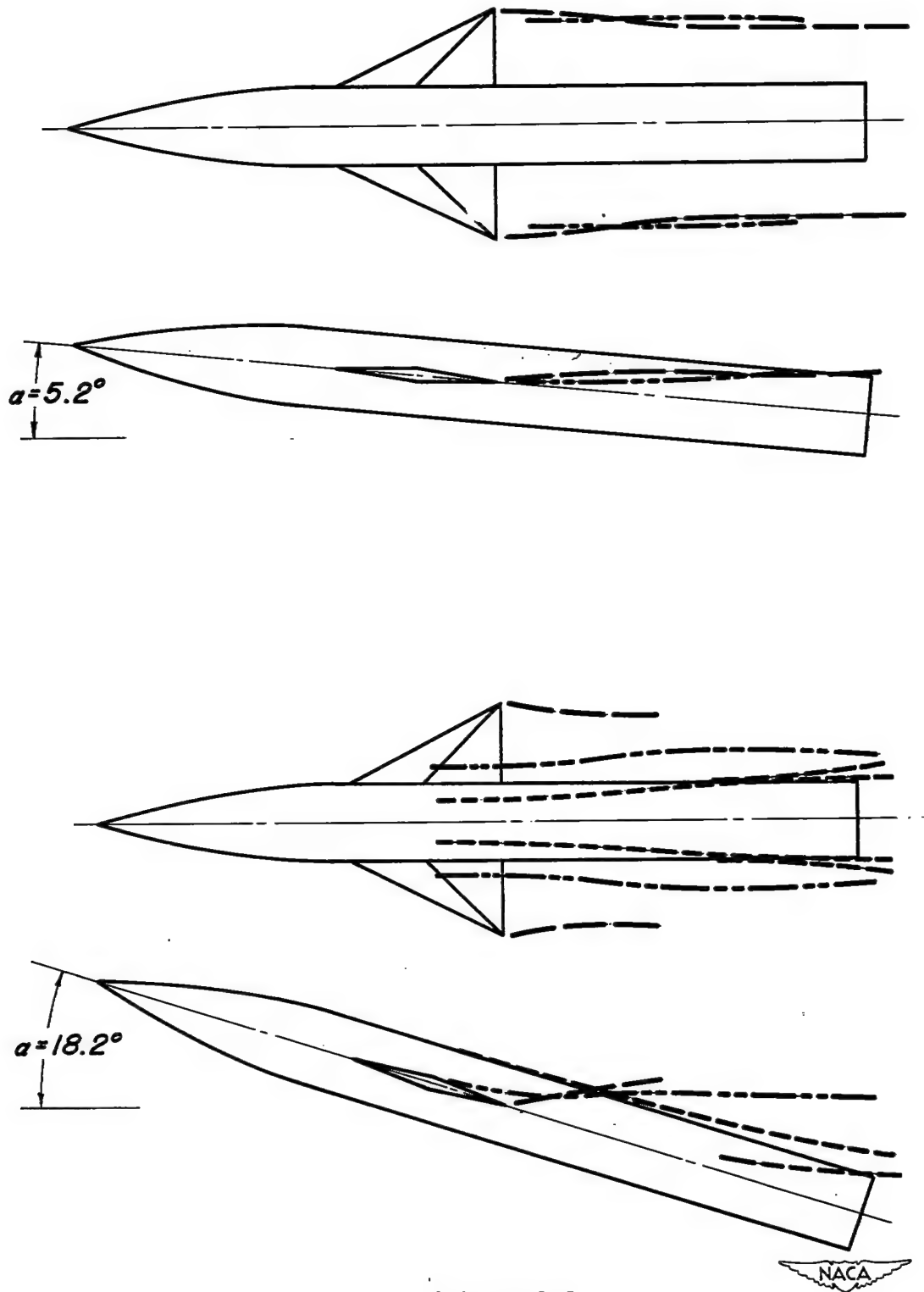


Figure 25.- Variation of vortex positions with angle of attack for the body. $M = 2.0$; $R = 1.6 \times 10^6$; $x/c_r = 1.8$.



(a) $A = 0.67$

Figure 26.- Vortex paths from vapor-screen photographs of wing-body combinations. $M = 2.0$; $R = 1.6 \times 10^6$.

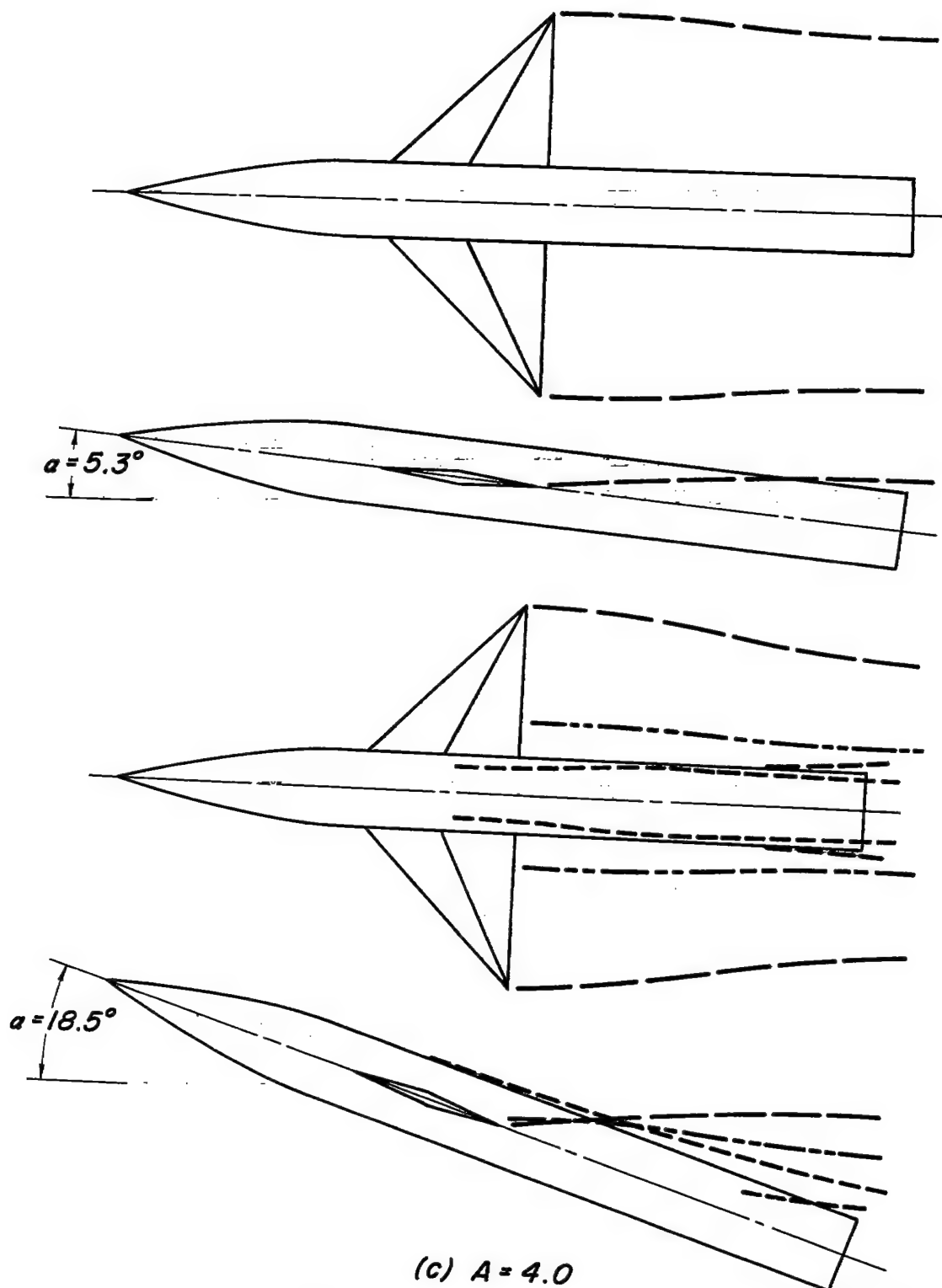


(b) $A = 2.0$

Figure 26.- Continued.

~~CONFIDENTIAL~~

NACA RM A53D10



(c) $A = 4.0$
Figure 26.- Concluded.

~~CONFIDENTIAL~~

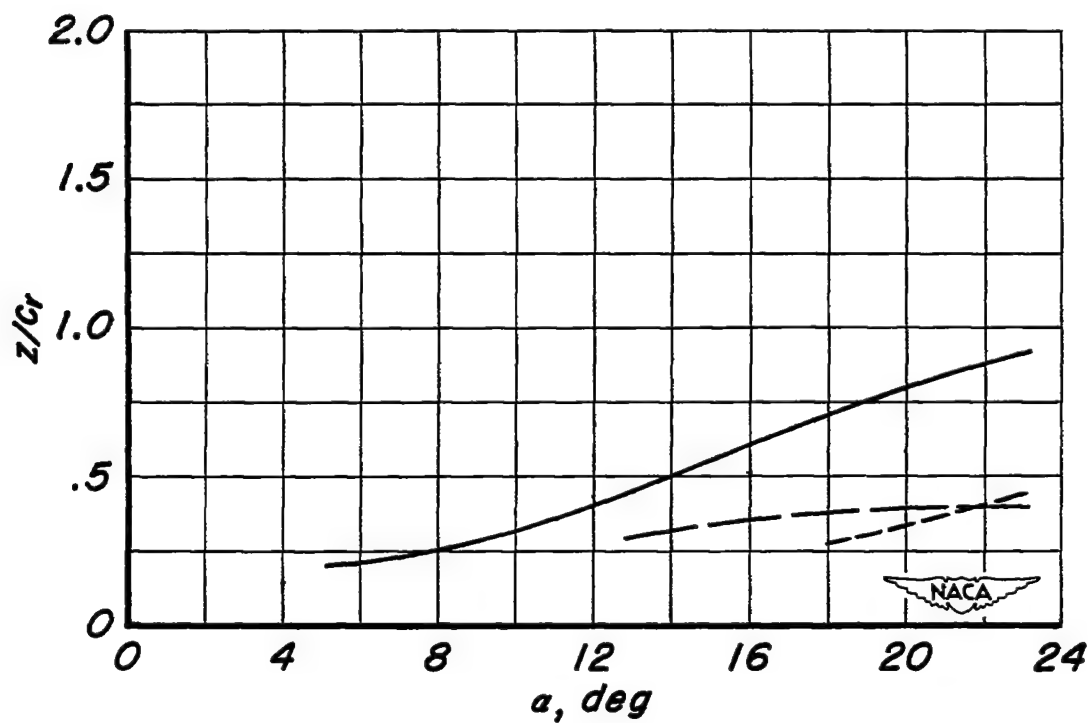
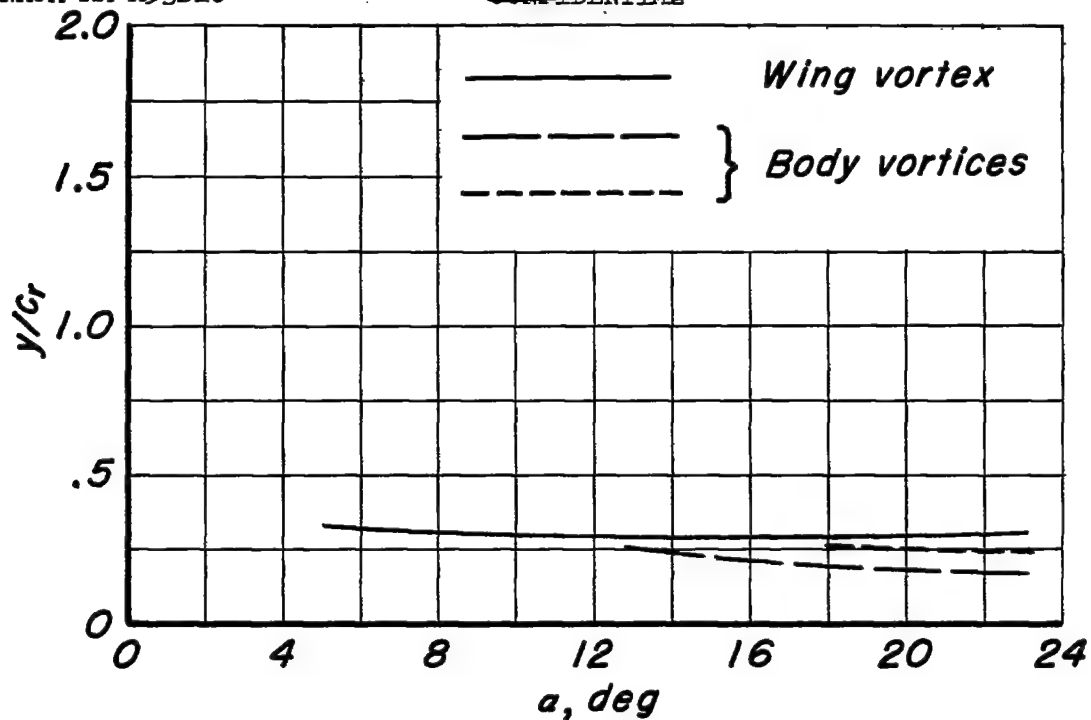
(a) $A = 0.67$

Figure 27.- Variation of vortex position with angle of attack for wing-body combinations. $M = 2.0$; $R = 1.6 \times 10^6$; $x/c_r = 1.8$.

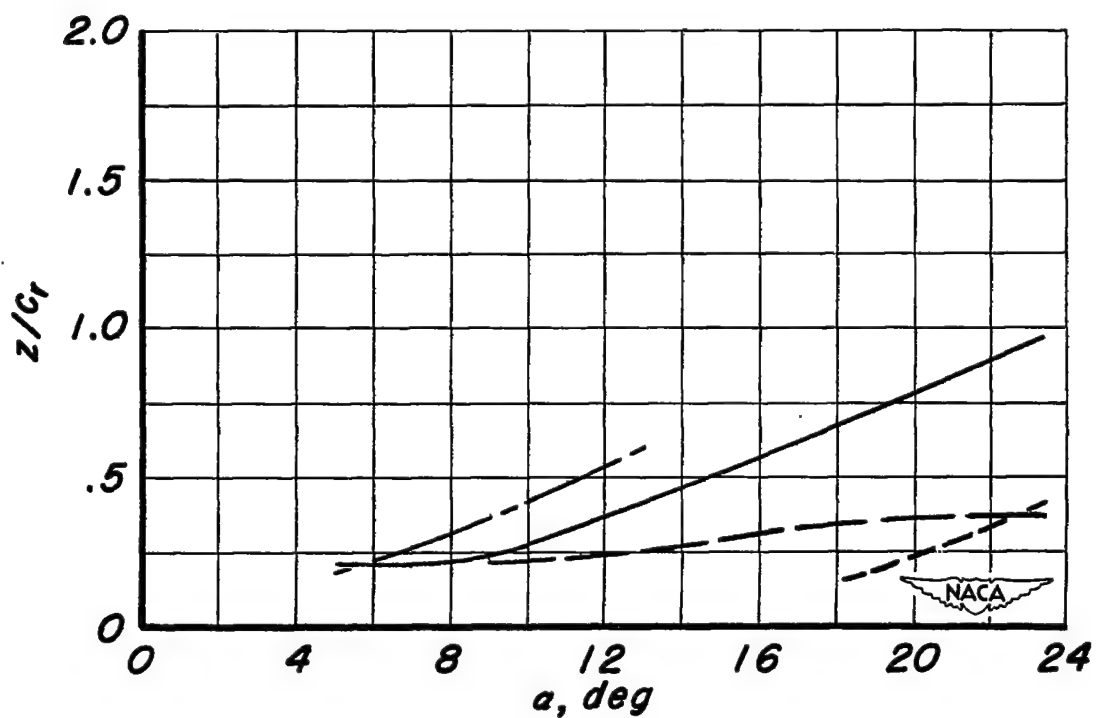
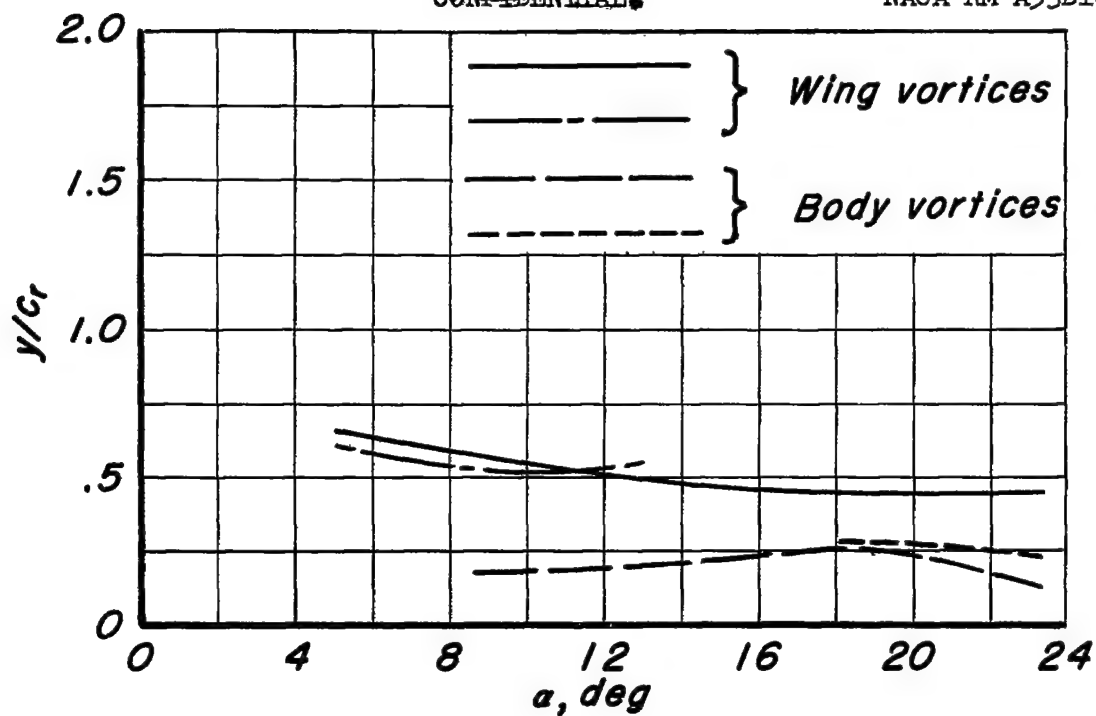
(b) $A=2.0$

Figure 27.- Continued.

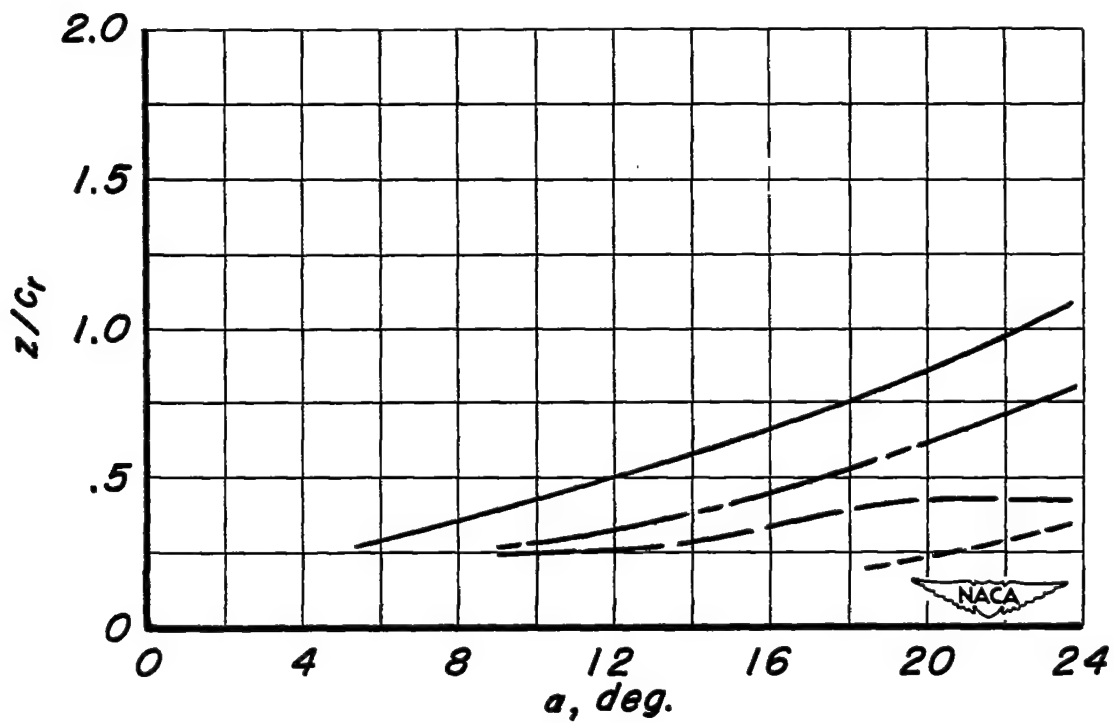
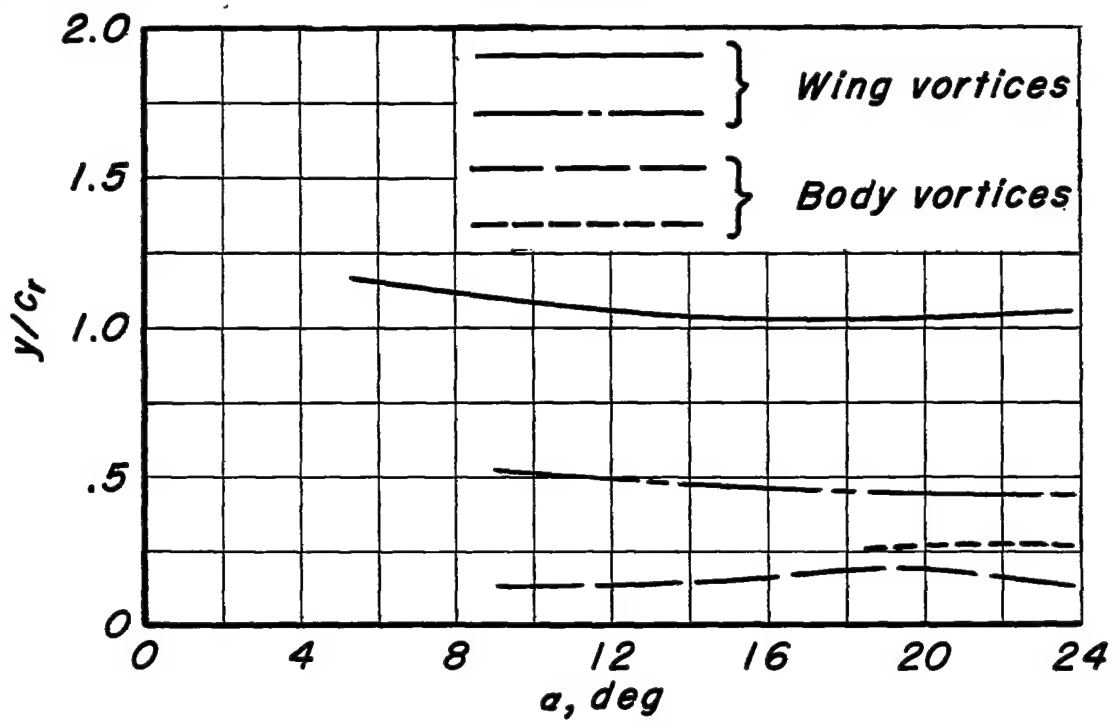
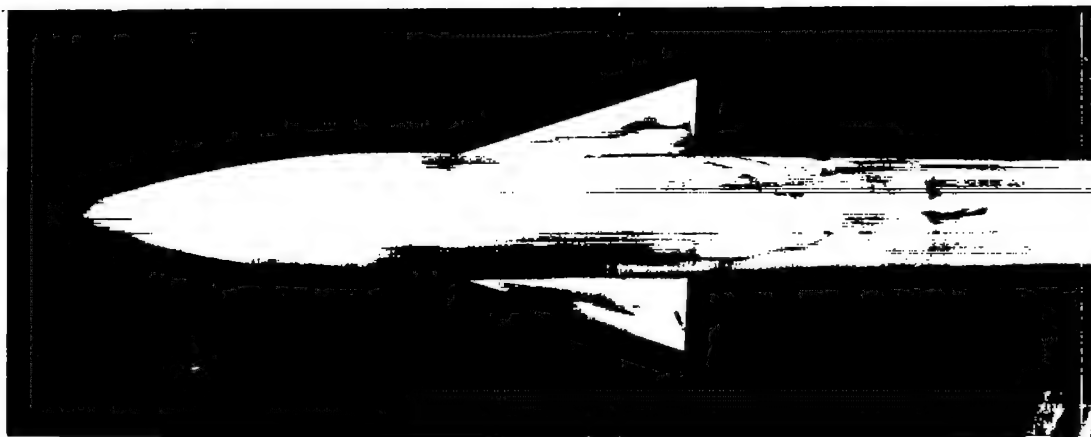
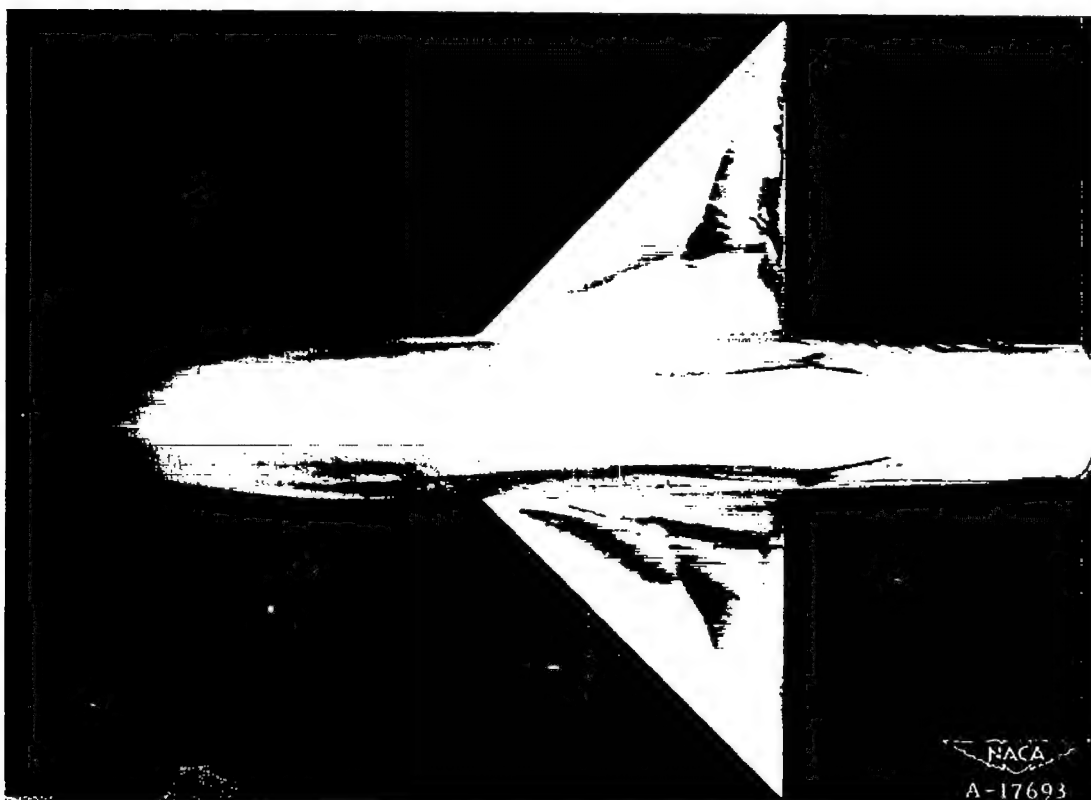
(c) $A = 4.0$

Figure 27.-Concluded.

~~CONFIDENTIAL~~

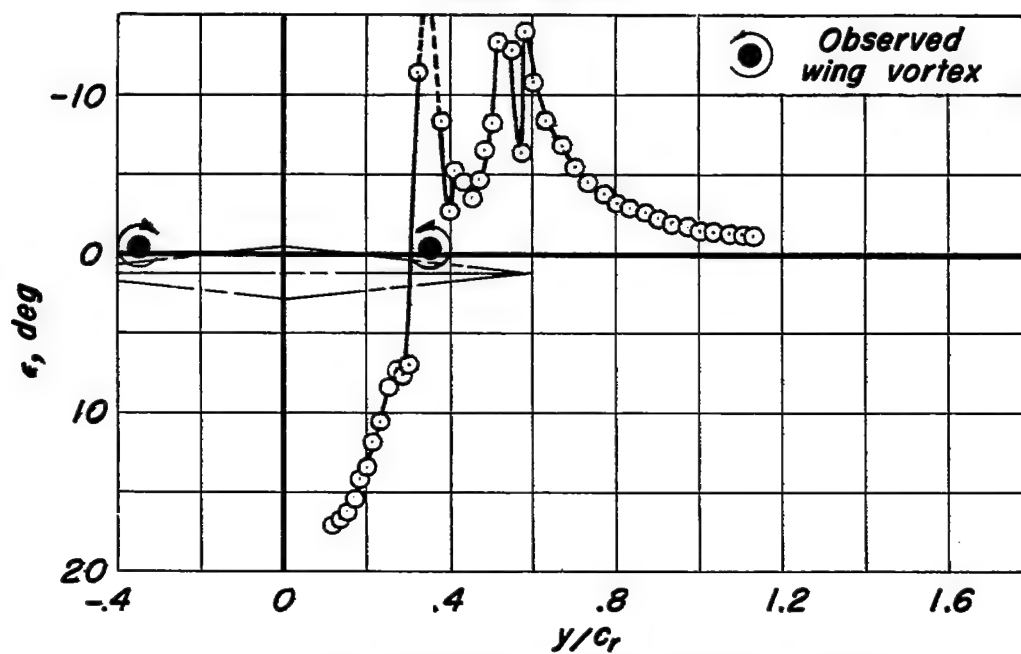
(a) $A = 1.33$; $\alpha = 18.1^\circ$



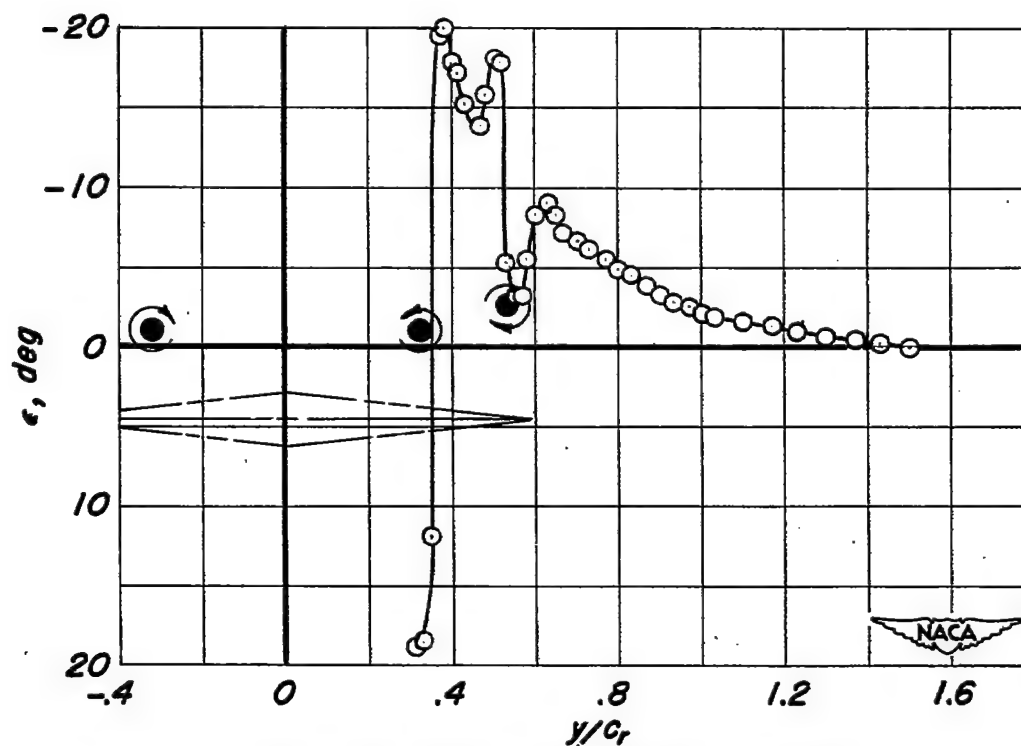
(b) $A = 4.0$; $\alpha = 18.5^\circ$

Figure 28.- China-clay photographs of wing-body combinations.
 $M = 2.0$; $R = 1.6 \times 10^6$.

~~CONFIDENTIAL~~



(a) $x/c_r = 0.1$; $z/c_r = 0.05$; $\alpha = 10.8^\circ$



(b) $x/c_r = 0.6$; $z/c_r = 0.18$; $\alpha = 14.6^\circ$

Figure 29.- Spanwise downwash distributions behind $A = 1.33$ wing
 $M = 2.0$, $R = 1.6 \times 10^6$.

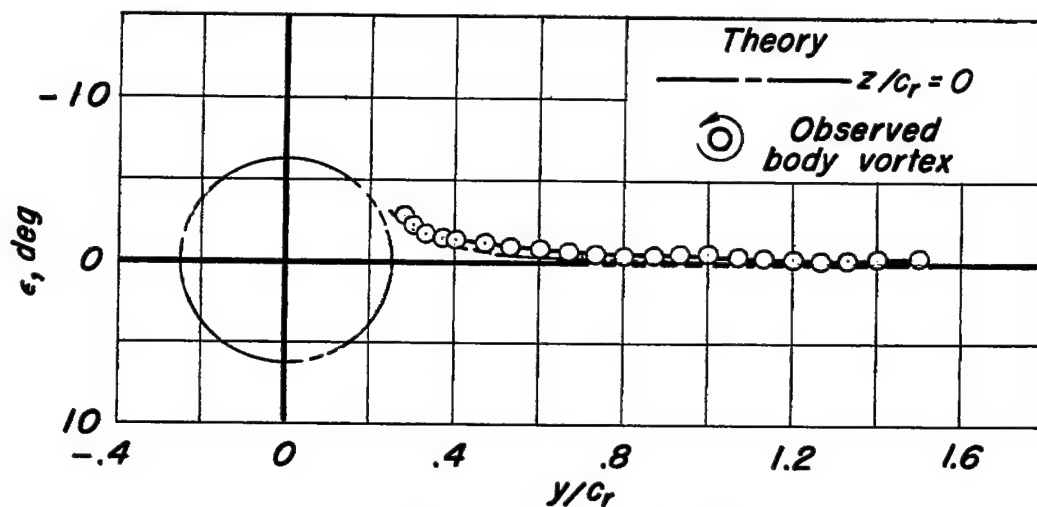
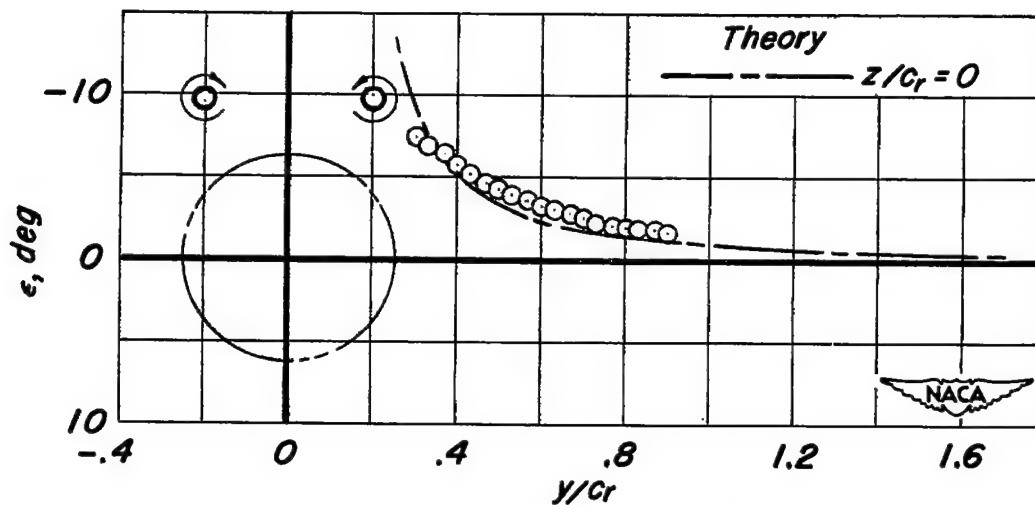
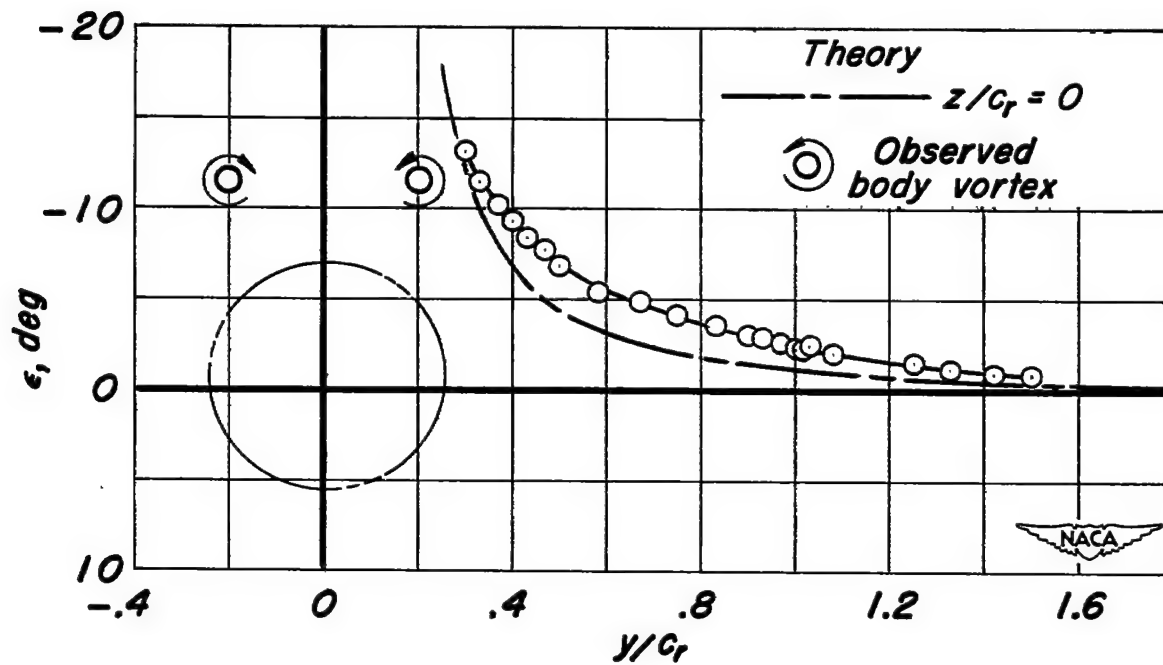
(a) $z/c_r = 0$; $\alpha = 2.8^\circ$ (b) $z/c_r = 0$; $\alpha = 13.3^\circ$

Figure 30.-Spanwise downwash distributions of the body at $x/c_r = 1.8$.
 $M = 2.0$; $R = 1.6 \times 10^6$.



(c) $z/c_r = -0.08$; $\alpha = 17.8^\circ$

Figure 30.- Concluded.

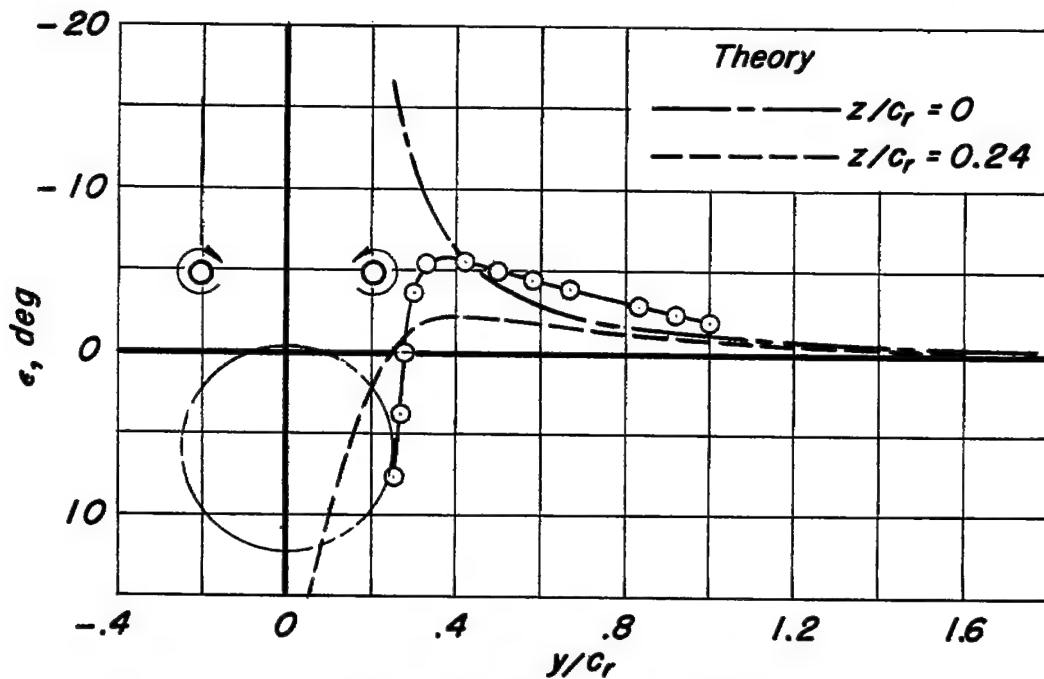
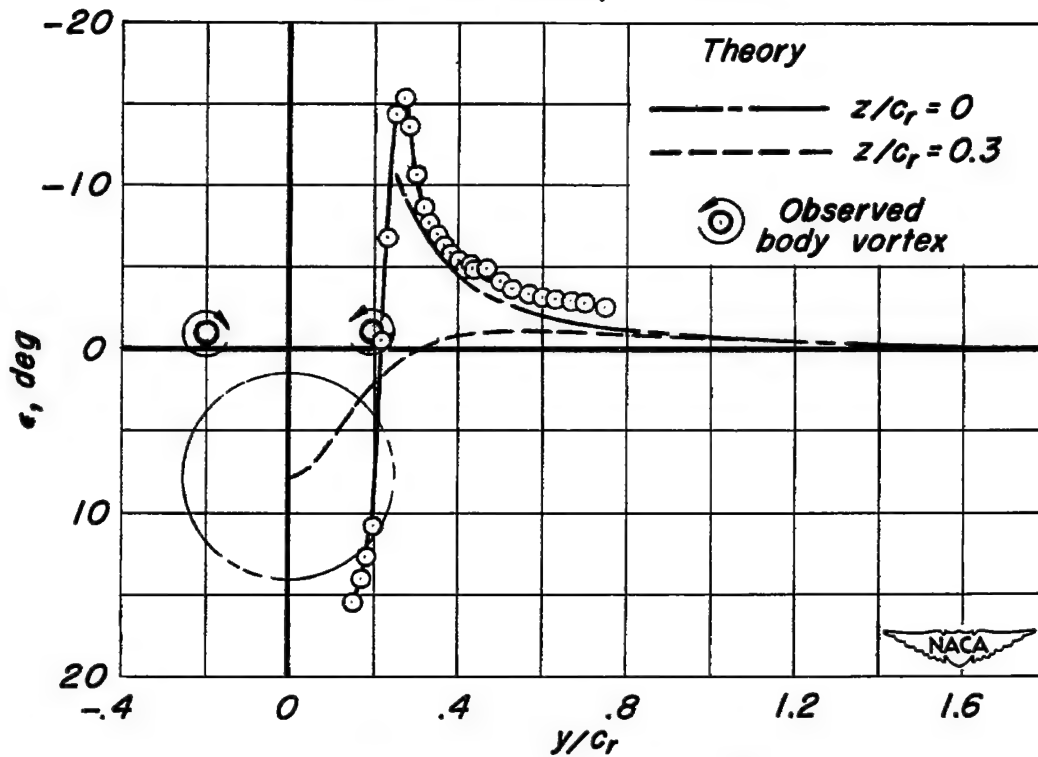
(a) $z/c_r = 0.24$; $\alpha = 16.2^\circ$ (b) $z/c_r = 0.3$; $\alpha = 11.4^\circ$

Figure 31.- Spanwise downwash distributions of the body at $x/c_r = 1.6$.
 $M = 2.0$; $R = 1.6 \times 10^6$

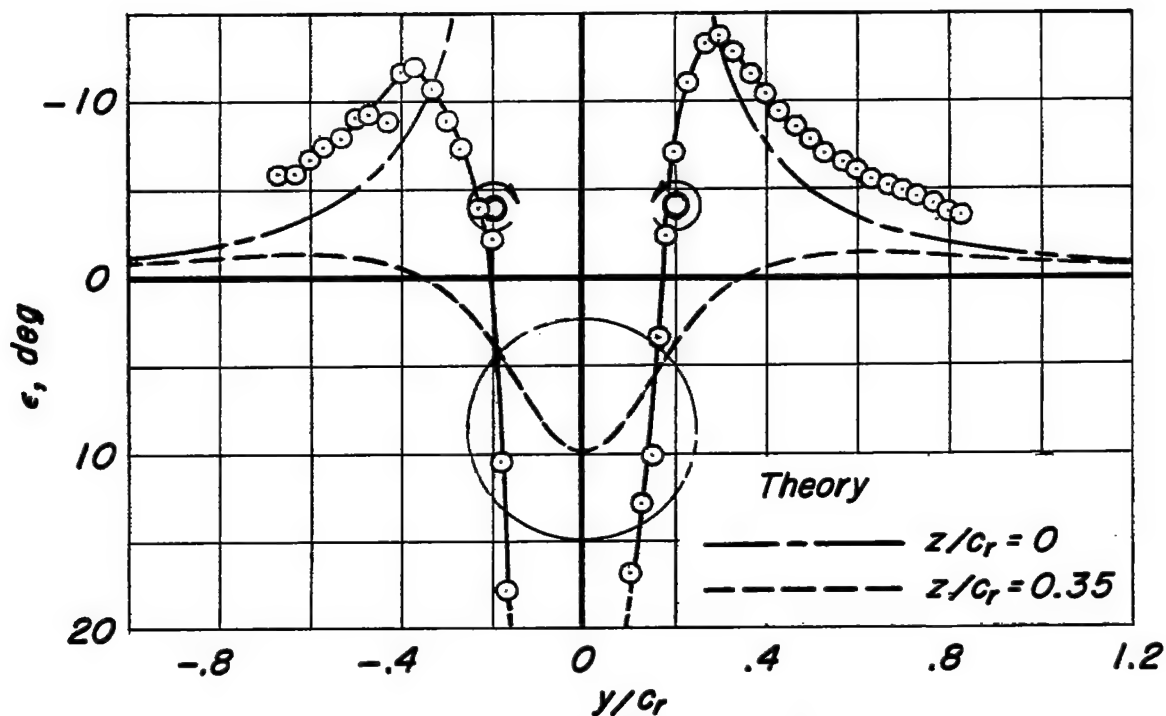
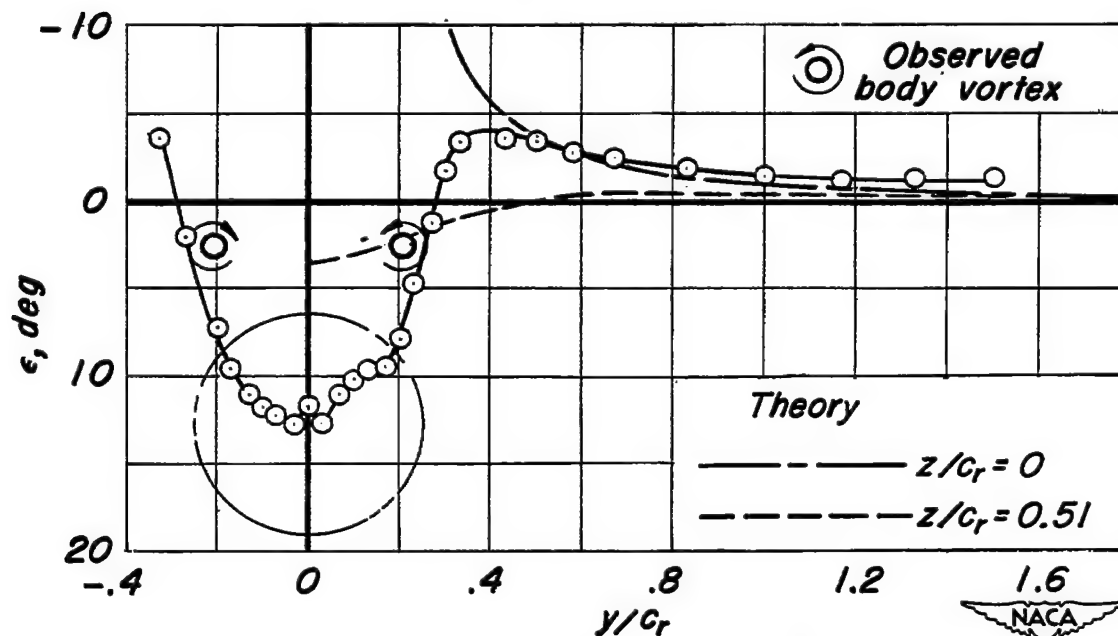
(c) $z/c_r = 0.35$; $\alpha = 19.3^\circ$ (d) $z/c_r = 0.51$; $\alpha = 14.7^\circ$

Figure 31.- Concluded.

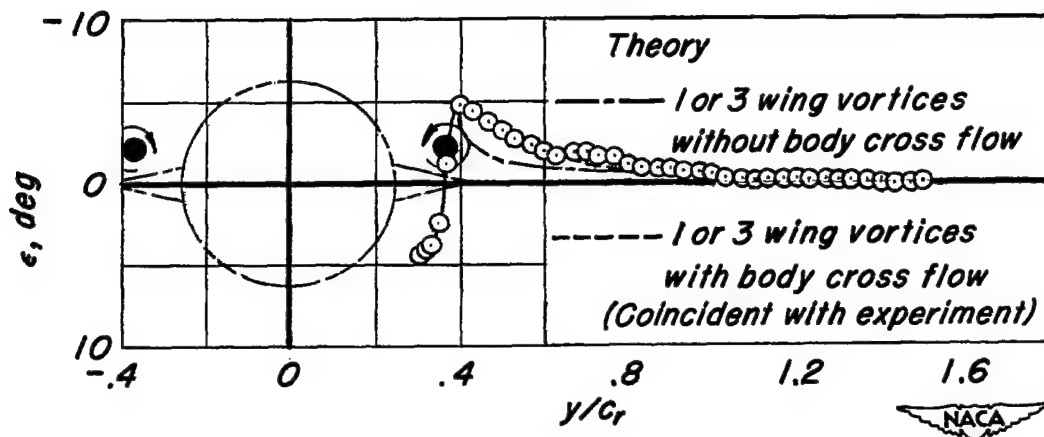


Figure 32.-Spanwise downwash distribution behind $A=0.67$ wing-body combinations at $x/c_r = 0.6$. $z/c_r = 0$; $\alpha = 5.0^\circ$; $M = 2.0$; $R = 1.6 \times 10^6$.

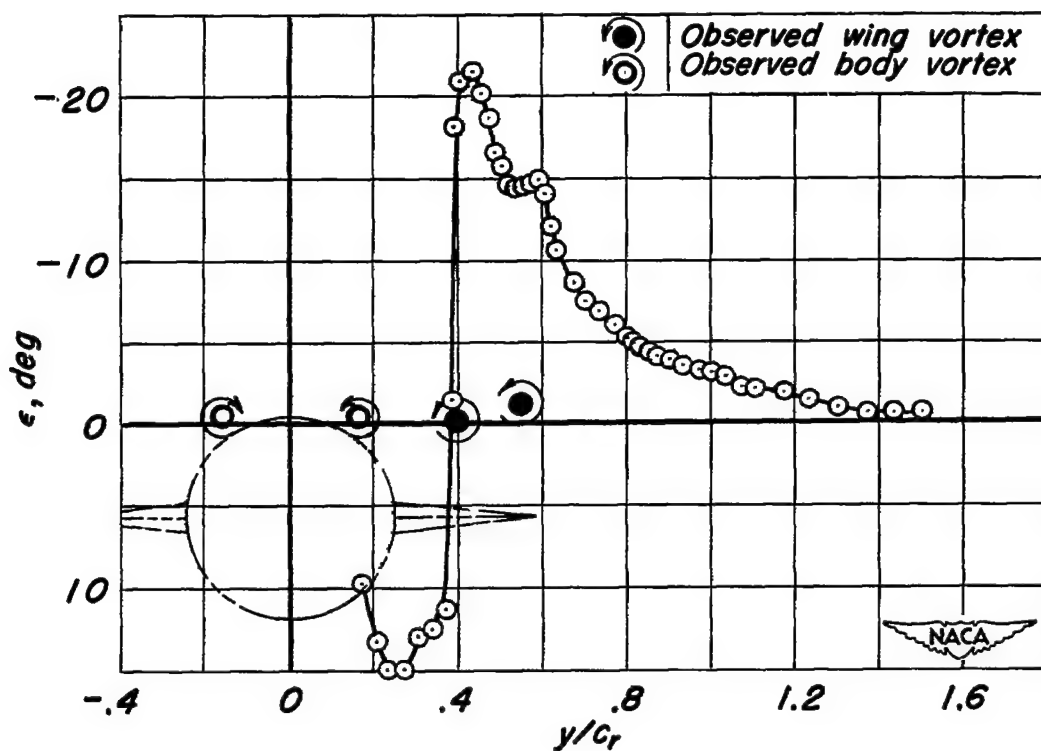


Figure 33.-Spanwise downwash distribution behind $A=1.33$ wing-body combination at $x/c_r = 0.6$. $z/c_r = 0.24$; $\alpha = 14.4^\circ$; $M = 2.0$; $R = 1.6 \times 10^6$.

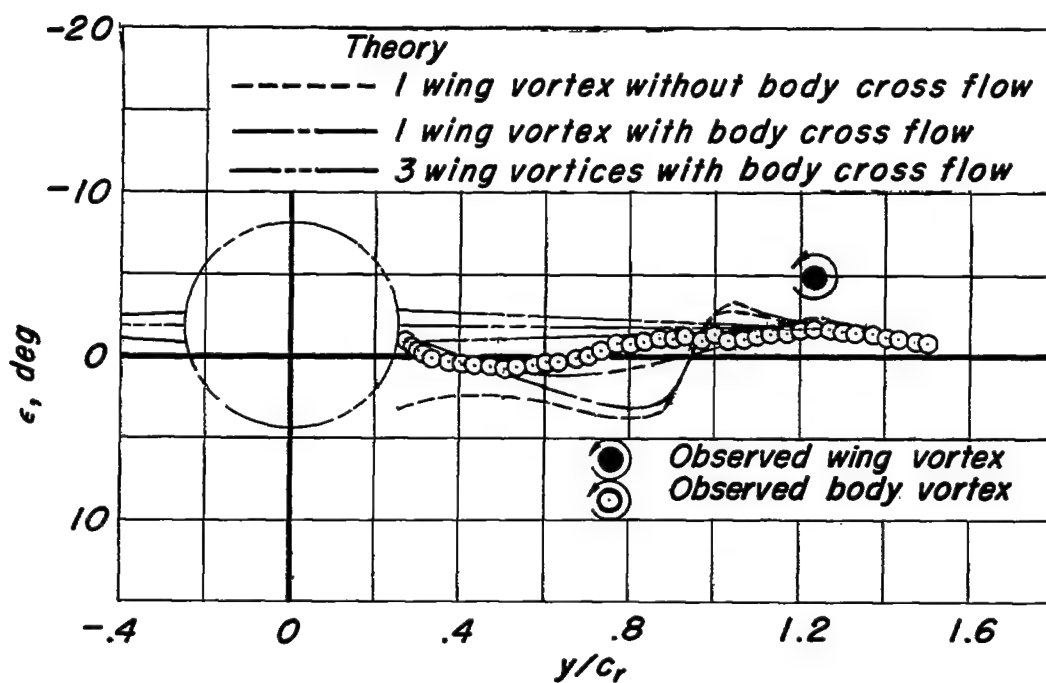
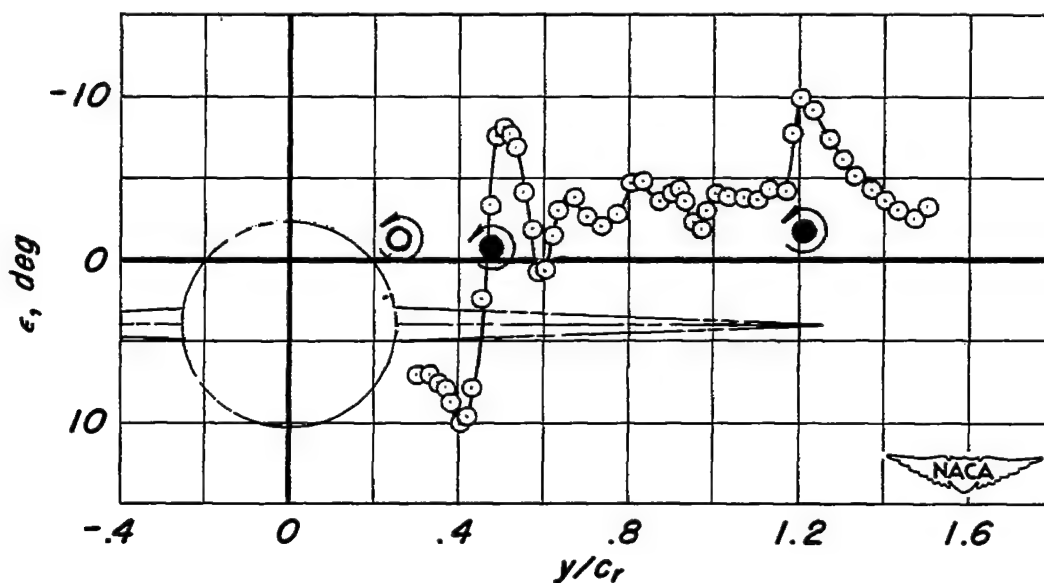
(a) $z/c_r = -0.1$; $\alpha = 5.9^\circ$ (b) $z/c_r = 0.2$; $\alpha = 15.2^\circ$

Figure 34.—Spanwise downwash distributions behind $A=4.0$ wing-body combinations at $x/c_r = 0.6$. $M=2.0$; $R=1.6 \times 10^6$.

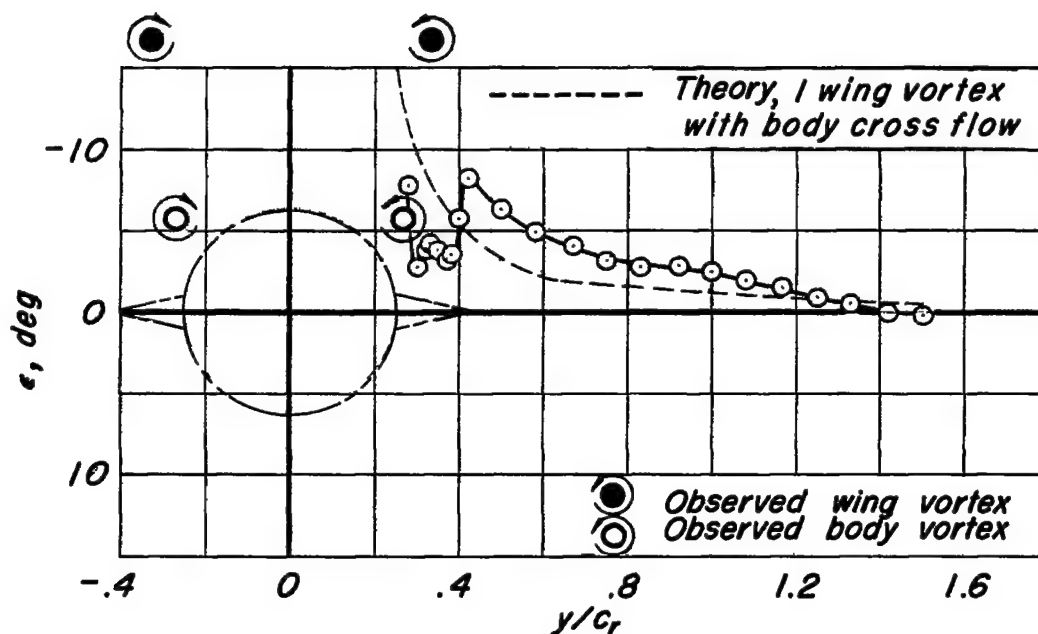
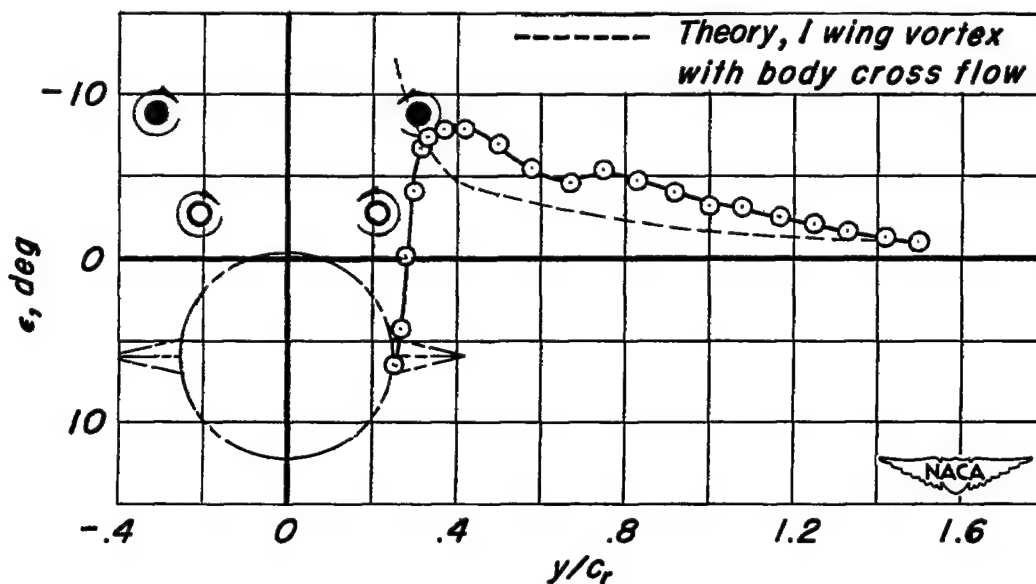
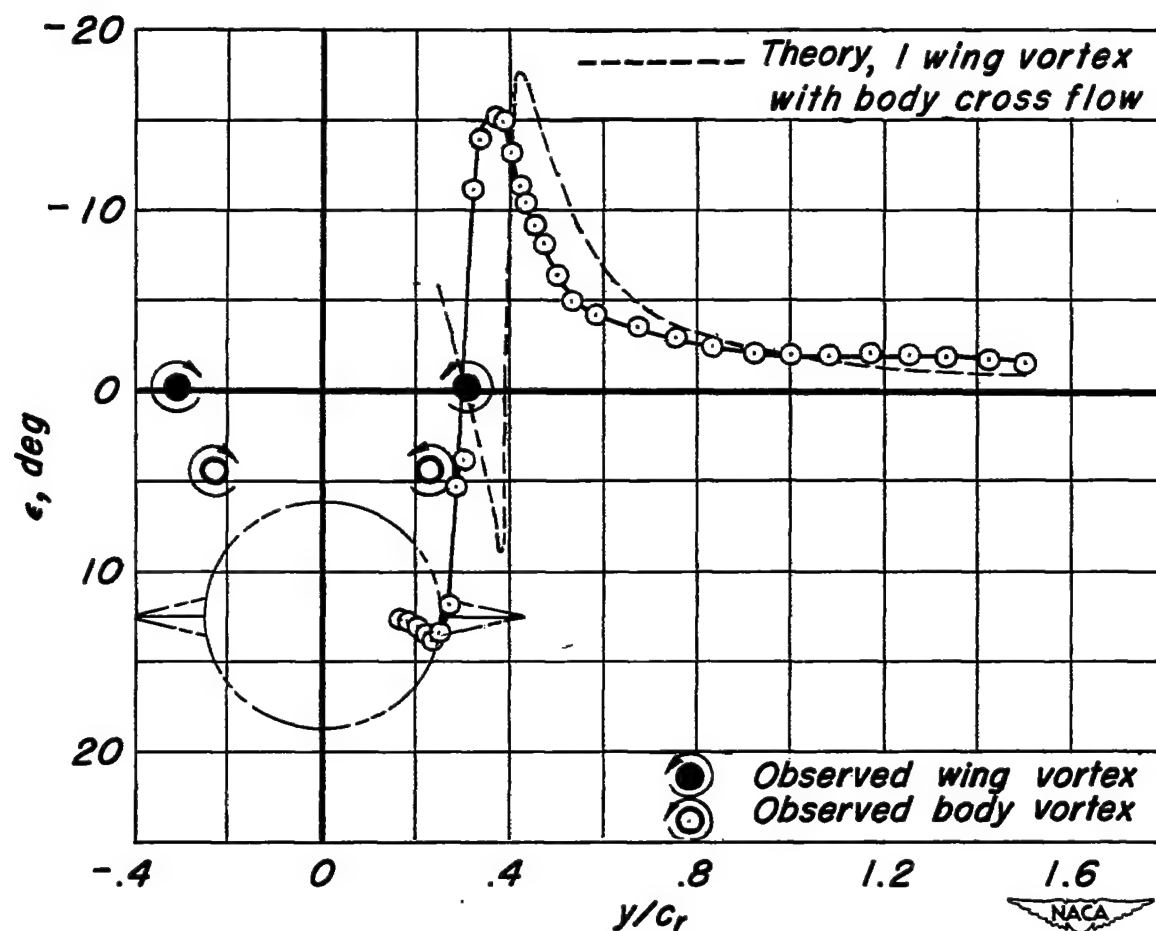
(a) $z/c_r = 0$; $\alpha = 17.9^\circ$ (b) $z/c_r = 0.24$; $\alpha = 16.4^\circ$

Figure 35.-Spanwise downwash distributions behind $A=0.67$ wing-body combinations at $x/c_r=1.6$. $M=2.0$; $R=1.6 \times 10^6$.



(c) $z/c_r = 0.50$; $\alpha = 14.8^\circ$

Figure 35.- Concluded.

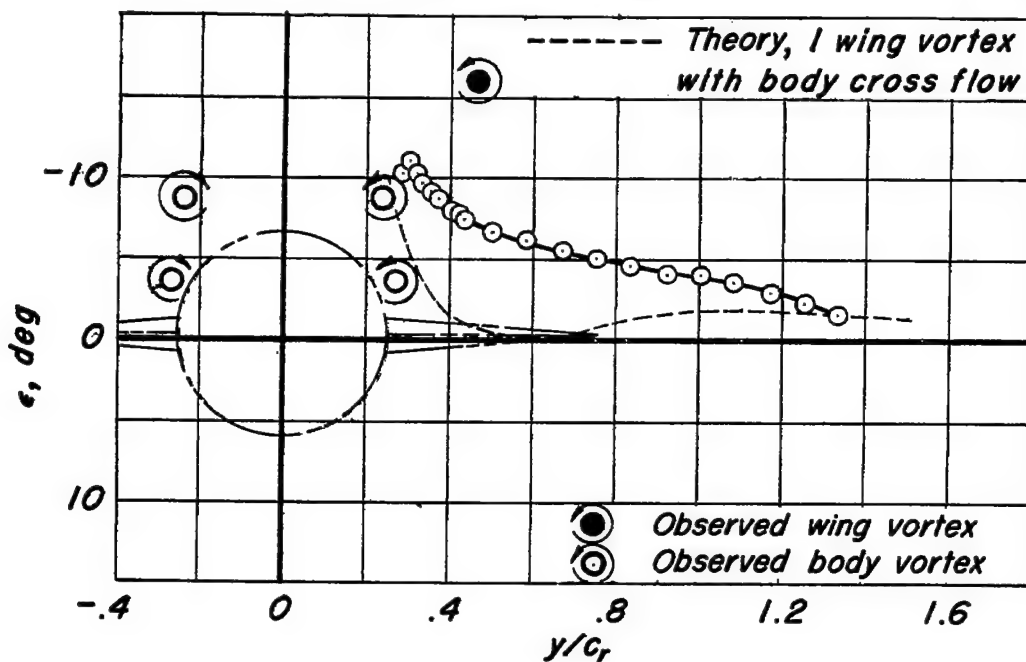
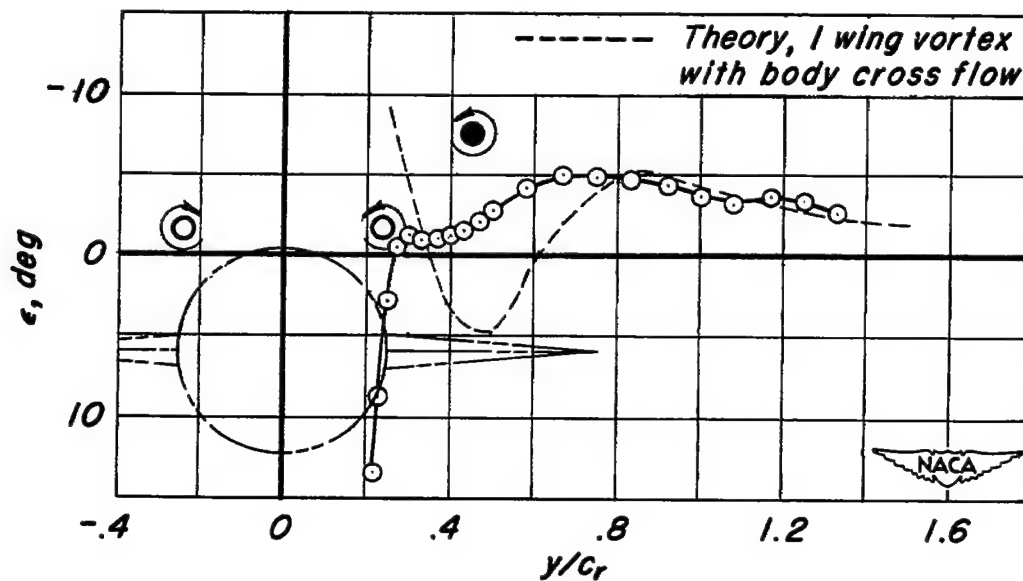
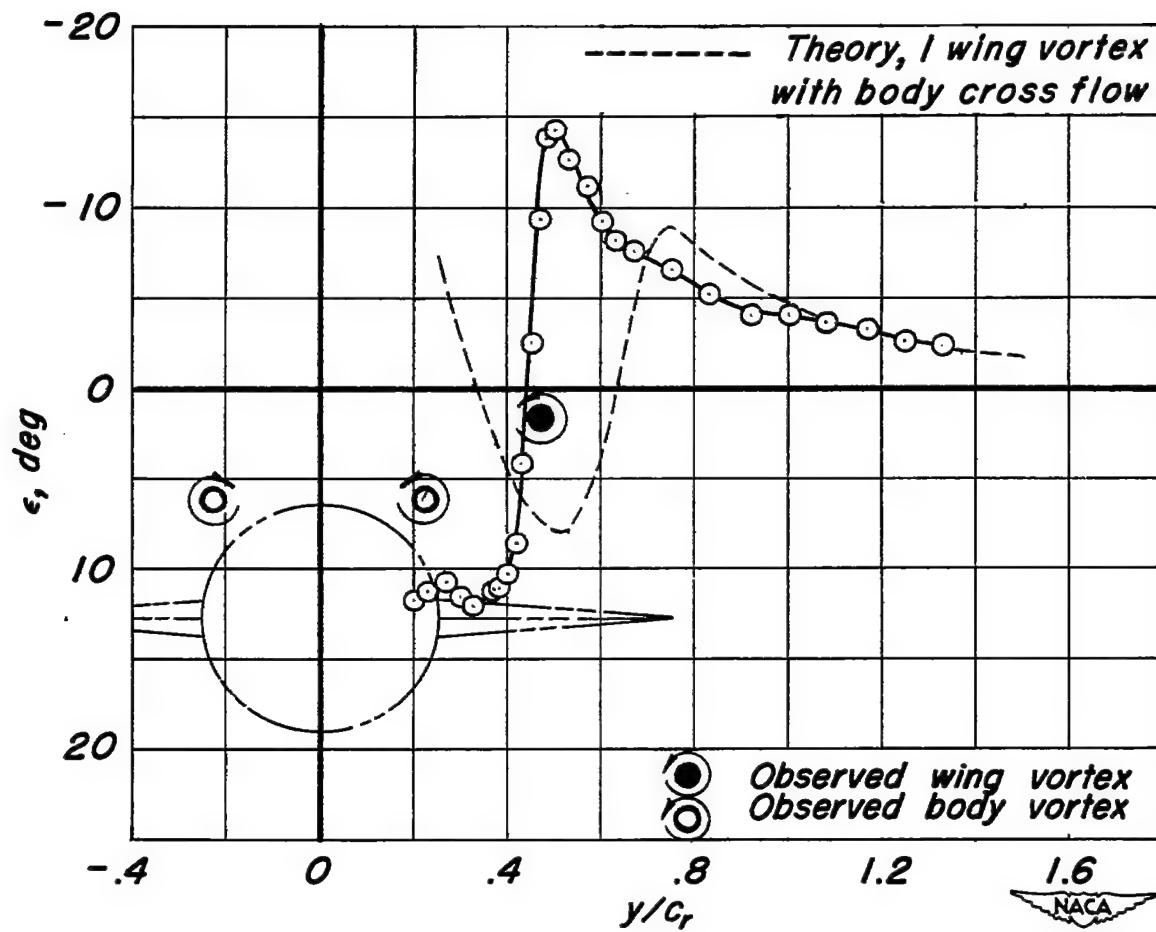
~~CONFIDENTIAL~~(a) $z/c_r = 0$; $\alpha = 18.1^\circ$.(b) $z/c_r = 0.24$; $\alpha = 16.6^\circ$

Figure 36.—Spanwise downwash distributions behind $A=2.0$ wing-body combinations at $x/c_r = 1.6$. $M=2.0$; $R=1.6 \times 10^6$.

~~CONFIDENTIAL~~



(c) $z/c_r = 0.51$; $\alpha = 15.0^\circ$

Figure 36. - Concluded.

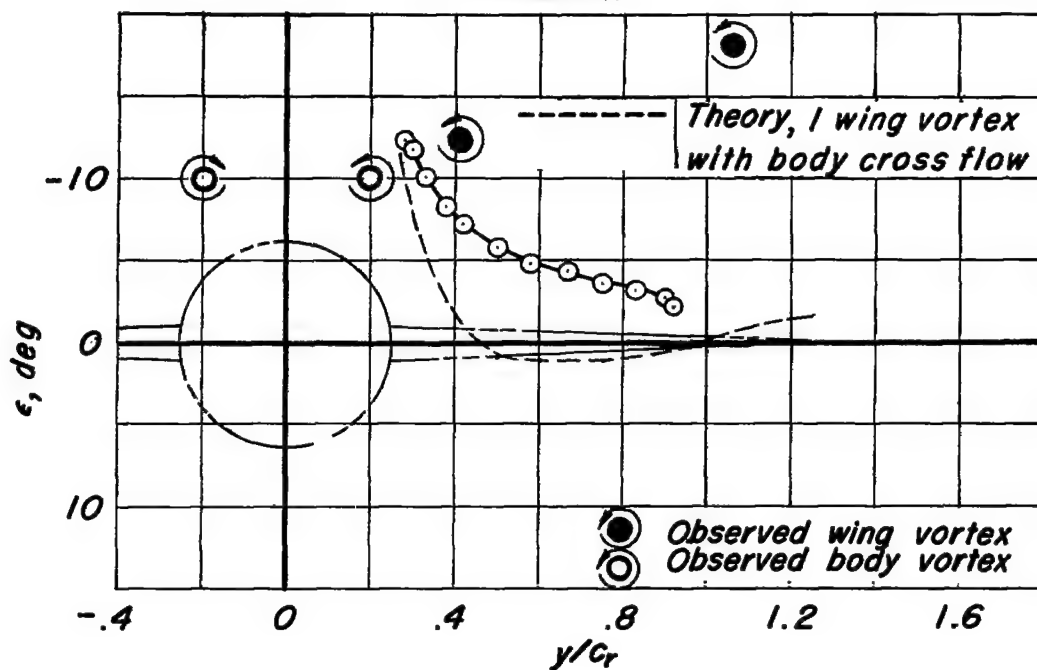
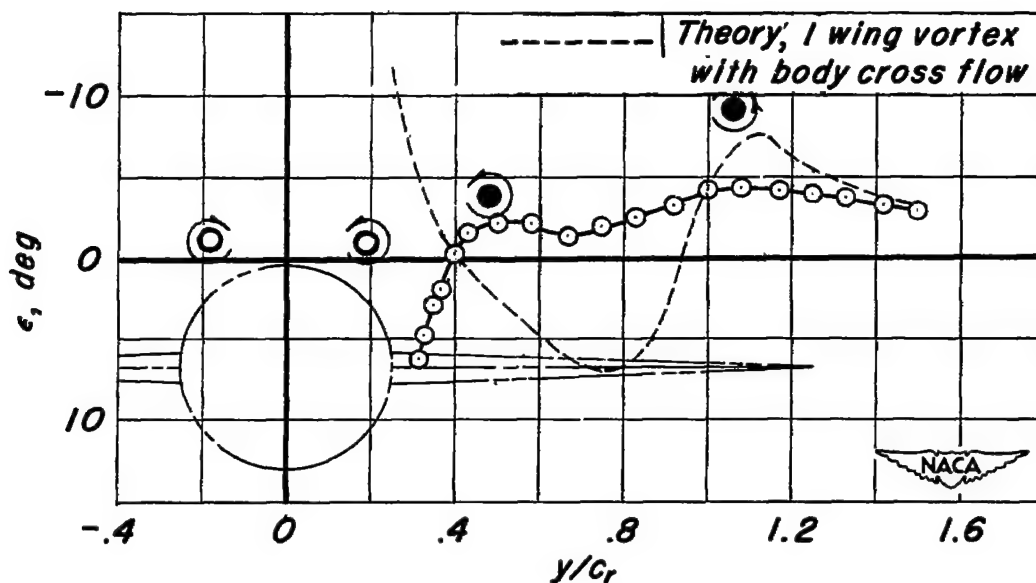
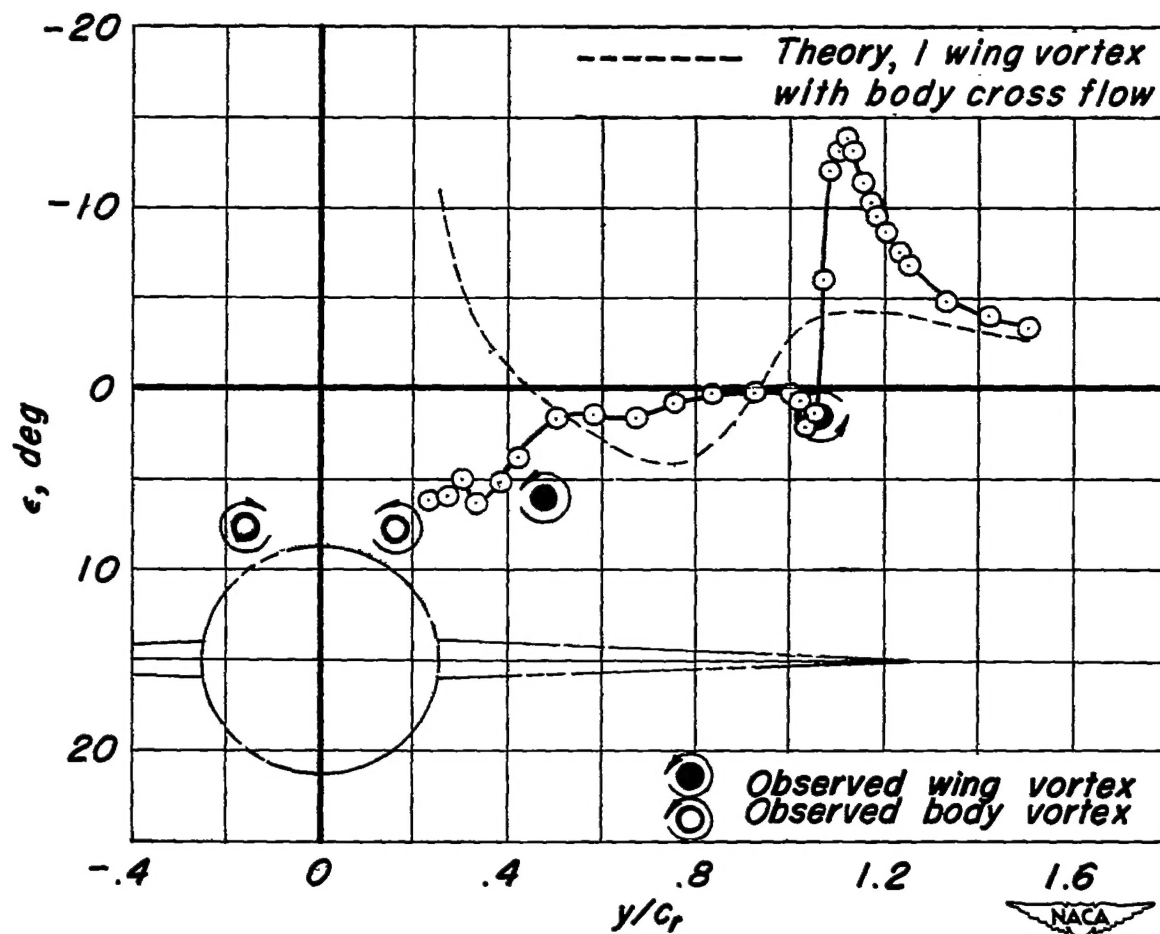
(a) $z/c_r = 0$; $\alpha = 18.5^\circ$ (b) $z/c_r = 0.27$; $\alpha = 16.6^\circ$

Figure 37.-Spanwise downwash distributions behind $A=4.0$ wing-body combinations at $x/c_r = 1.6$. $M=2.0$; $R=1.6 \times 10^6$.



(c) $z/c_r = 0.60$; $\alpha = 14.8^\circ$

Figure 37.- Concluded.

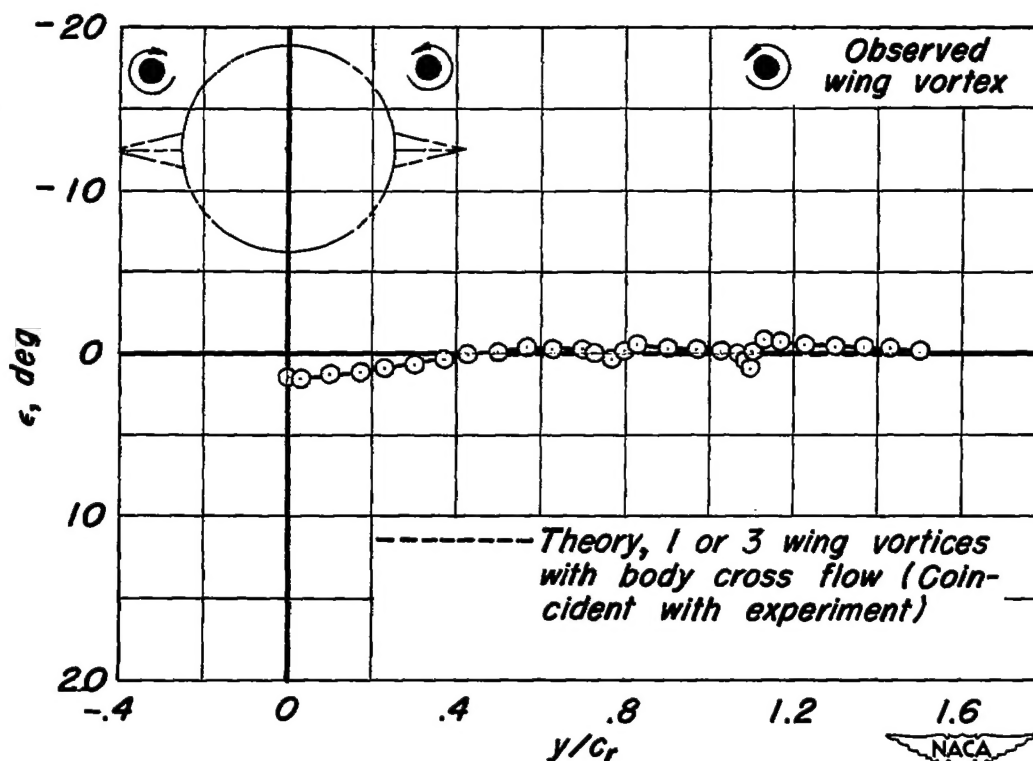
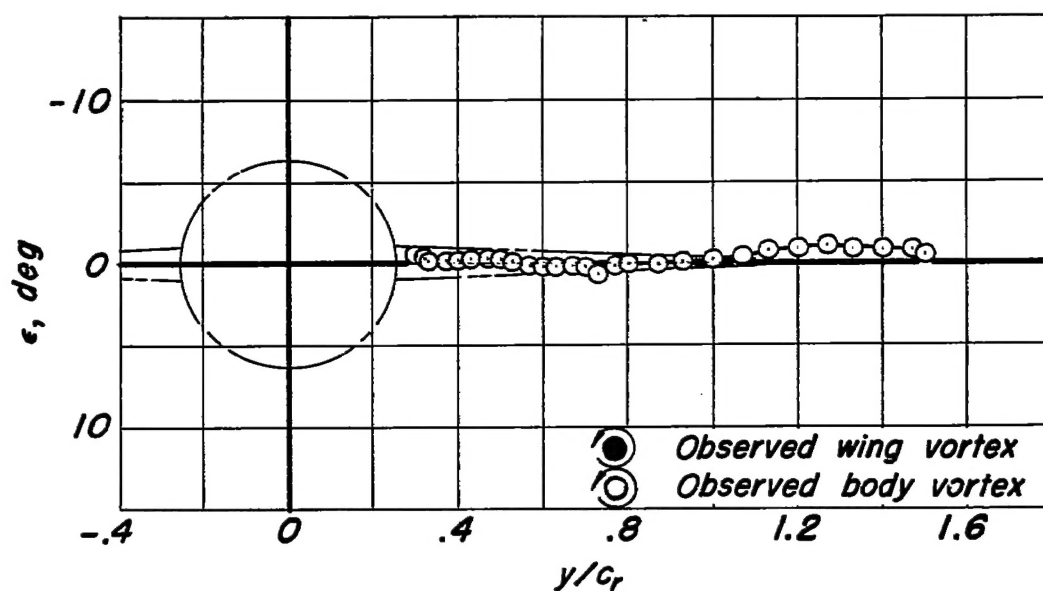
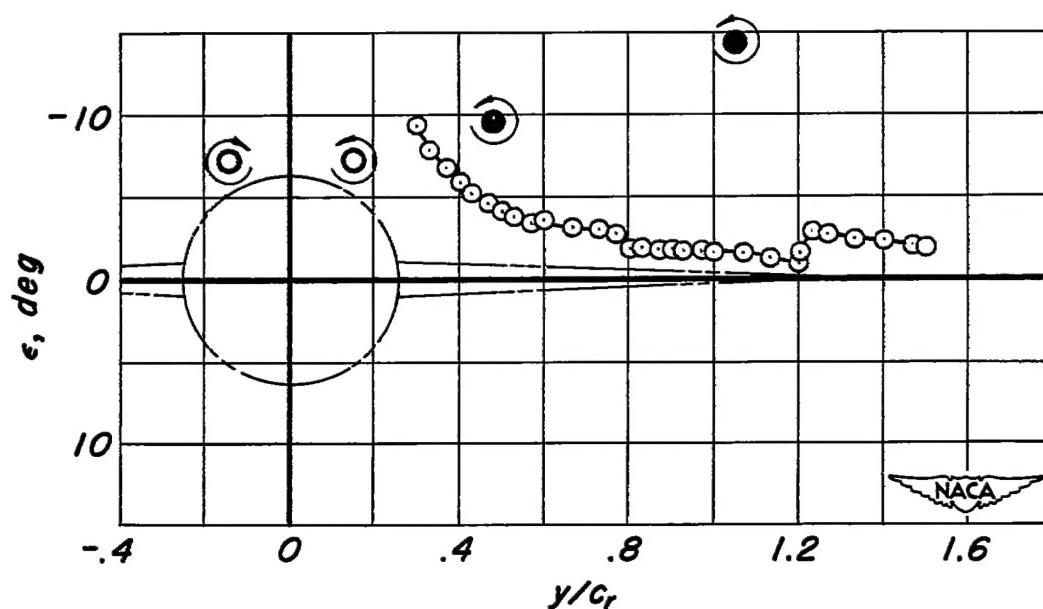


Figure 38.—Spanwise downwash distributions behind $A=0.67$ wing-body combinations at $x/c_r=1.8$. $z/c_r=-0.5$; $\alpha=5.0^\circ$; $M=2.0$; $R=1.6 \times 10^6$.

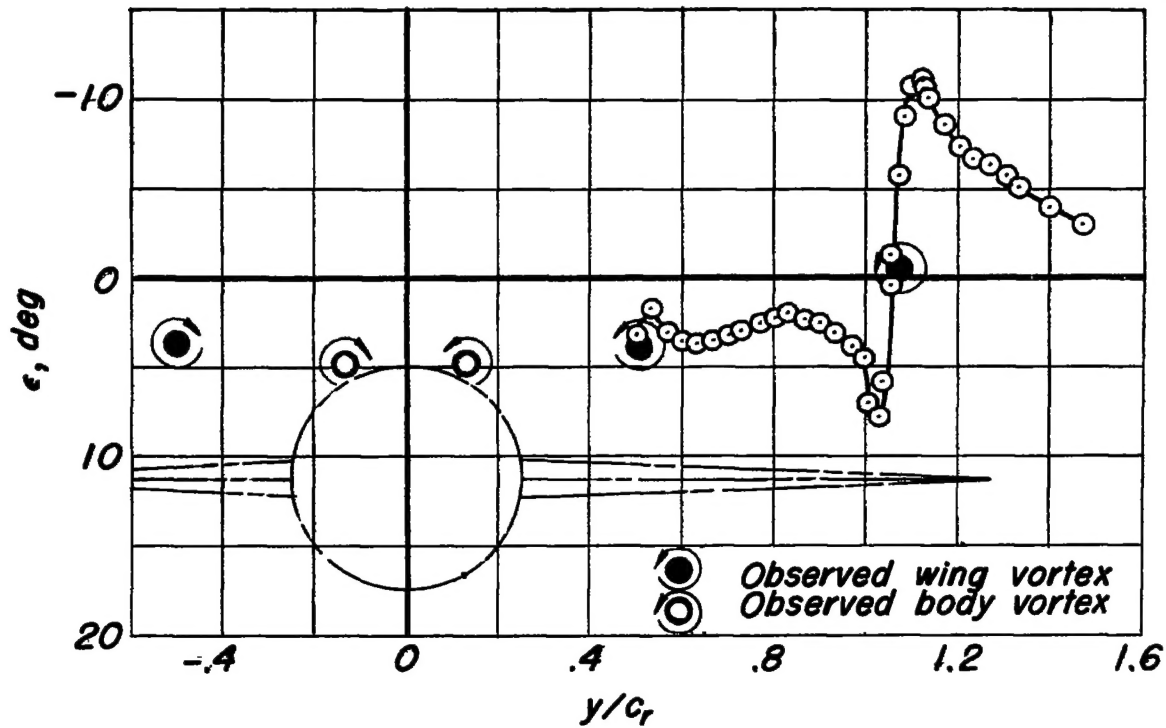


(a) $z/c_r = 0$; $\alpha = 3.0^\circ$

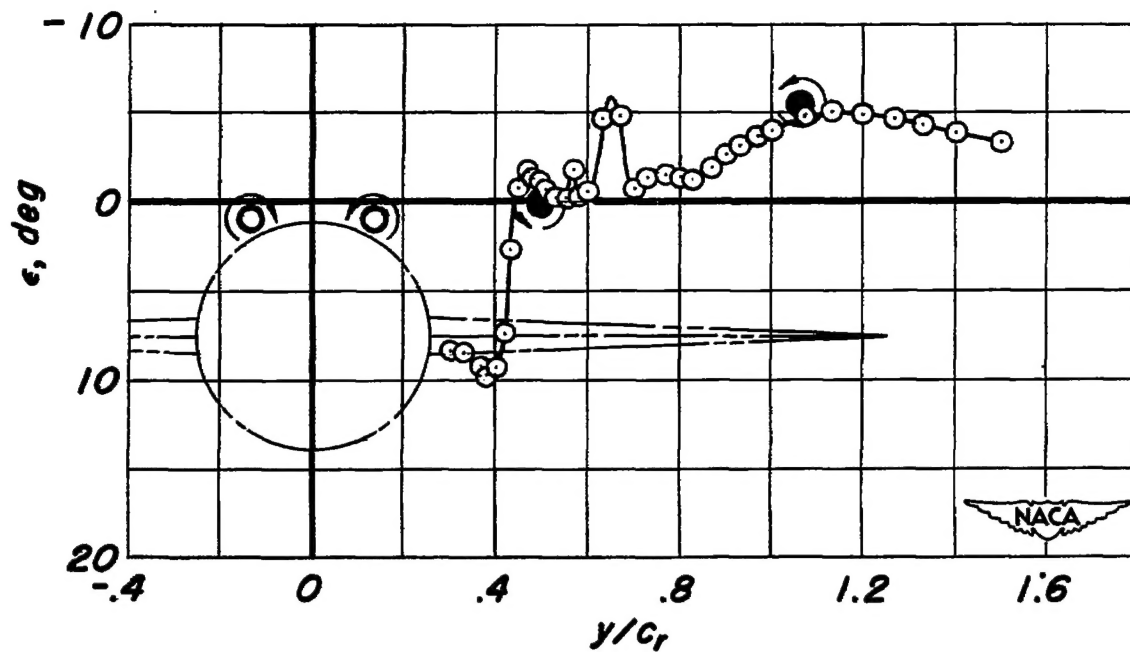


(b) $z/c_r = 0$; $\alpha = 13.9^\circ$

Figure 39.—Spanwise downwash distributions behind $A=4.0$ wing-body combinations at $x/c_r=1.8$. $M=2.0$; $R=1.6 \times 10^6$.



(c) $z/c_r = 0.45; \alpha = 11.1^\circ$



(d) $z/c_r = 0.3; \alpha = 11.8^\circ$

Figure 39.- Concluded.

CONFIDENTIAL